FRUCTOSE-1,6-BISPHOSPHATASE 2 INHIBITS SARCOMA PROGRESSION BY RESTRAINING MITOCHONDRIAL BIOGENESIS

Yangpeiwei Huang

A DISSERATION

in

Cell and Molecular Biology

Presented to the Faculties of the University of Pennsylvania

in

Partial Fulfillment of the Requirements for the

Degree of Doctor of Philosophy

2019

Supervisor of Dissertation

_____

M. Celeste Simon, Ph.D.

Arthur H. Rubenstein, MBBCh Professor, Cell and Developmental Biology

Scientific Director and Investigator, Abramson Family Cancer Research Institute

Graduate Group Chairperson

_____

Daniel S. Kessler, Ph.D.

Associate Professor of Cell and Developmental Biology

Dissertation Committee

_____

Margaret M. Chou, Ph.D. (chair), Associate Professor of Cell and Developmental Biology

Zoltan Pierre Arany, M.D., Ph.D., Professor of Medicine

Peter S. Klein, M.D., Ph.D., Professor of Medicine

Chi Van Dang, M.D., Ph.D., Scientific Director of Ludwig Cancer Research

FRUCTOSE-1,6-BISPHOSPHATASE 2 INHIBITS SARCOMA PROGRESSION BY RESTRAINING MITOCHONDRIAL BIOGENESIS

To my parents and husband, Chenchen

ACKNOWLEDGMENT

Completing my Ph.D. work and writing this thesis is a challenging task, which would not be possible without support from various people.

First, I would like to express my sincere gratitude to my advisors Dr. M. Celeste Simon and Dr. Brian Keith for their great mentorship and persistent support during my Ph.D. study and research, for their patience, motivation, enthusiasm, and immense knowledge. I deeply appreciate the tremendous support and encouragement I received from them along my graduate life, not only in scientific research, but also personal and career development. I feel lucky to have them as my mentors and I could not have imagined having a better advisor for my Ph.D. study.

I would like to acknowledge the members of my thesis committee: Dr. Margaret M. Chou, Dr. Zoltan P. Arany, Dr. Peter S. Klein and Dr. Chi Van Dang, who have provided continuous support and advice on my research project. I have benefited a lot from their insightful comments and helpful discussions, as well as the instructive courses they offered.

I am grateful to be working with my lab mates. I truly enjoy the collaborative and encouraging lab environment they create under the guidance of Celeste and Brian. I would like to express my gratitude to all of my lab mates for the technical supports and stimulating discussion. I also want to thank previous lab members, including Dr. Bo Li, Dr. Tzipora Sarah Karin Eisinger, Dr. Kyoung Eun Lee and Dr. Michael Nakazawa, for their invaluable advice and inspiring inputs during the initiation of my thesis study.

I also owe thanks to my lifelong friends out of the lab for their company and caring along my graduate school journey. I have met some of the most ambitious, talented, and humble individuals in graduate school. I would especially like to thank Dr. Nan Lin, who has been a source of support since the first day of graduate school.

I would like to thank my parents. Without their unconditional support and love, I could not achieve what I have now. They are the best example for me to grow up and to be a determined person. I hope I can continue to make you proud.

Finally, I would like to thank my husband, Chenchen. Our love is the most important motivation for me to face the challenges and overcome the difficulties.

ABSTRACT

FRUCTOSE-1,6-BISPHOSPHATASE 2 INHIBITS SARCOMA PROGRESSION BY RESTRAINING MITOCHONDRIAL BIOGENESIS

Yangpeiwei Huang

M. Celeste Simon

Sarcomas are uncommon but diverse mesenchymal malignancies arising from connective tissues, such as muscle, fat and cartilage. Despite rapid advances in molecular understanding of individual subtypes and pathway-specific therapies, the remarkable cellular and genetic heterogeneity of soft tissue sarcomas (STS) limits clinical benefit of targeted treatments. A variety of metabolism-associated oncogenic signaling pathways have been identified in sarcomas. Both these internal and external alterations converge to change cell metabolism, rendering sarcoma cells more susceptible to perturbations within metabolic networks. However, how abnormal metabolism influences sarcoma growth remains understudied.

I show that expression of the gluconeogenic isozyme fructose-1,6-bisphosphatase 2 (FBP2) is silenced in a broad spectrum of STS subtypes, revealing an apparent common metabolic feature shared by diverse STS. Enforced FBP2 re-expression inhibits STS cell and tumor growth through two distinct mechanisms. First, cytosolic FBP2 antagonizes elevated glycolysis associated with the "Warburg effect", thereby inhibiting sarcoma cell proliferation. Second, nuclear-localized FBP2 restrains mitochondrial biogenesis and respiration in a catalytic activity-independent manner by inhibiting the expression of nuclear respiratory factor (NRF1) and mitochondrial transcription factor A (TFAM). Specifically, nuclear FBP2 colocalizes with the c-Myc transcription factor at the *TFAM* locus and represses c-Myc-dependent *TFAM* expression. This unique dual function of FBP2 provides a rationale for its selective suppression in STS, identifying a potential metabolic vulnerability and possible future therapeutic target.

Table of Contents

LIST OF TABLES

LIST OF ILLUSTRATIONS

Chapter 3. RESULTS

LIST OF ILLUSTRATIONS (continued)

CHAPTER 1 INTRODUCTION

This chapter has been adapted from the following review article: Huangyang, Peiwei, and M. Celeste Simon. "Hidden features: exploring the non-canonical functions of metabolic enzymes." Disease models & mechanisms 11.8 (2018): dmm033365. https://dmm.biologists.org/content/11/8/dmm033365.abstract

Introduction to soft tissue sarcomas

Soft tissue sarcomas (STS) encompass a diverse group of mesenchymal tumors arising from connective tissues, such as muscle, fat and cartilage. Each year, approximately 13,000 new cases are diagnosed in the United States, and 5,000 patients succumb to this disease (Siegel et al., 2019). Collectively, STS are classified into more than 70 subtypes based on pathological and clinical features, ranging from indolent to highly invasive and metastatic (Cancer Genome Atlas Research Network, 2017; Fletcher, 2014). Liposarcoma, undifferentiated pleomorphic sarcoma (UPS), and fibrosarcoma represent 40% of newly diagnosed sarcomas in adults (Lehnhardt et al., 2009). Although recent studies have integrated genome-scale analyses of the molecular mechanisms underlying sarcomagenesis and progression (Cancer Genome Atlas Research Network, 2017; Taylor et al., 2011), these cancers remain understudied due to their extensive heterogeneity. Current treatment options are limited to standard surgical resection, radiotherapy and chemotherapy (Mehren et al., 2018); however, response rates to cytotoxic chemotherapy are only 10-25% (Linch et al., 2014). Highly divergent genomic alterations and low response rates to traditional treatments necessitate development of effective therapies that exploit common features of sarcoma progression.

Metabolic alterations in soft tissue sarcomas

Various oncogenic signaling pathways and microenvironmental stresses converge to modify cellular metabolism, adapting it to limited nutrient and oxygen availability (Vander Heiden and DeBerardinis, 2017). A broad array of oncogenes and tumor suppressors that regulate metabolic pathways are mutated in sarcomas, such as *PIK3CA* (catalytic subunit of phosphatidylinositol 3-

kinase), *TP53*, and *NF1* (Barretina et al., 2010; Cancer Genome Atlas Research Network, 2017). In addition to effects imposed by genetic mutations, hypoxic (O_2-deprived) tumor microenvironments characteristic of STS alter metabolism and are associated with worse prognosis (Brizel et al., 1996; Sadri and Zhang, 2013). While reprogrammed metabolic activities likely promote sarcoma growth and progression, they also create unique vulnerabilities and therefore new opportunities for therapeutic intervention. Previously, labeled isotope infusion of sarcoma patients revealed elevated tissue glucose uptake and turnover, accompanied by decreased glucose oxidation (Shaw et al., 1988), suggesting abnormal glucose metabolism in these tumors. Glycolysis is counterbalanced by anabolic gluconeogenesis to maintain glucose homeostasis, and gluconeogenic enzymes play important roles in regulating tumor cell growth and behavior (Wang and Dong, 2019).

Introduction to fructose-1,6-bisphosphatase and its role in cancer

Fructose-1,6-bisphosphatase (FBP) is a rate-limiting enzyme that catalyzes the irreversible hydrolysis of fructose-1,6-bisphosphate to fructose-6-phosphate and inorganic phosphate. Vertebrates possess two highly conserved FBP isozymes exhibiting 76.6% sequence identity: FBP1 is detected primarily in liver and kidney, whereas FBP2 expression is more ubiquitous although highest in skeletal muscle and other mesenchymal tissues. Recently, FBP1 loss has been found to contribute to the progression of multiple epithelial tumors, including clear cell renal cell carcinoma (ccRCC), breast cancer, hepatocellular carcinoma and pancreatic ductal adenocarcinoma (Dong et al., 2013; Hirata et al., 2016; Li et al., 2014; Zhu et al., 2015). Several mechanisms are implicated in downregulating FBP1, including transcription factor repression (Zhu et al., 2015), epigenetic silencing (Bigl et al., 2008; Chen et al., 2011; Yang et al., 2017) and proteasome degradation (Jin et al., 2017).

Restoration of FBP1 expression in breast cancer and ccRCC cells strongly antagonizes glycolysis through its catalytic activity (Dong et al., 2013; Li et al., 2014); however, FBP1 also regulates genes in ccRCC cells through an unanticipated nuclear function. Specifically, we

demonstrated that FBP1 directly suppresses the transcriptional activity of hypoxia-inducible factors (HIFs) through an enzymatic activity-independent mechanism (Li et al., 2014). HIFs regulate several hundred genes, including those encoding the glycolytic enzymes GLUT1, HK2, PFK1 and LDHA, to facilitate cellular adaptation to hypoxia (Nakazawa et al., 2016b); thus, FBP1 loss further enhances HIF responses. Interestingly, over 90% of ccRCC tumors harbor von Hippel-Lindau (VHL) mutations that stabilize HIFs even under normoxia (Nickerson et al., 2008). However, in pVHL-expressing ccRCC cells, FBP1 no longer inhibits glycolysis and NADPH production, suggesting that HIFs are required for FBP1-mediated effects on glucose metabolism. Further investigation found that FBP1 physically interacts with both HIF-1α and HIF-2α, and suppresses HIF target gene expression by co-localizing with HIF-1α at hypoxia-responsive elements (HREs) within these loci. Additionally, the suppression of HIF activity is abolished when a nucleus-excluded FBP1, but not the catalytically dead FBP1, is introduced into ccRCC cells (Li et al., 2014). These data suggest that FBP1's activity as a HIF transcriptional co-repressor is restricted to the nucleus in a catalytic-activity independent manner.

Whereas FBP1 has been studied in a variety of carcinomas, little is known about the role of FBP2 in mesenchymal cells or STS. The consensus nuclear localization sequence between FBP1 and FBP2 indicates that FBP2 might also preserve some previously unknown nuclear functions, which might also be involved in inhibiting sarcoma progression.

Non-canonical functions of metabolic enzymes

With the development of new experimental techniques, advances in cancer metabolism research have greatly enhanced our understanding of how cancer cells benefit from altered metabolism to support their growth. For example, subcellular fractionation revealed that a majority of key glycolytic enzymes are actually present in the nucleus (Kim and Dang, 2005). It is intriguing to speculate that these enzymes have unexpected nuclear functions, such as stimulating gene expression, which impacts specific cell decisions in response to fuel supply and demand. An emerging paradigm proposes that metabolic enzymes, rather than simple components of biochemical pathways, are multi-functional proteins. They can act as mediators between growth stimuli, signaling pathways

and downstream effectors, over and above the changes in metabolism contributing to many other biological functions, such as gene transcription, apoptosis, and cell-cycle progression.

A key finding from studies of metabolic enzymes is the existence of mechanistic links between their nuclear localization and the regulation of transcription. By modulating gene expression, metabolic enzymes themselves facilitate adaptation to rapidly changing environments. Furthermore, they can directly shape a cell's epigenetic landscape (Kaelin and McKnight, 2013). Strikingly, several metabolic enzymes exert completely distinct functions in different cellular compartments. Nuclear fructose bisphosphate aldolase, for example, directly interacts with RNA polymerase III to control transcription (Cieśla et al., 2014); whereas in the cytosol, it mediates signal transduction, vesicle trafficking and cell motility (Lincet and Icard, 2015). Indeed, a growing list of multifaceted enzymes supports the possibility that cells employ existing proteins in different and efficient ways, without the need to replicate or transcribe additional genes. We provide an overview of metabolic enzymes for which non-canonical functions have been identified (Table 1) and their implications in cancer.

Summary

The central goal of this study was to characterize the metabolic and transcriptional impacts of FBP2 on sarcoma progression. We demonstrate here that *FBP2* transcription is markedly silenced in the majority of STS subtypes, and that restoring FBP2 expression dramatically inhibits sarcoma cell proliferation *in vitro* and tumor growth *in vivo*, implicating FBP2 loss as an important general event during sarcomagenesis. Isotope tracing and unbiased mass spectrometry analyses of liposarcoma, fibrosarcoma and UPS cells demonstrated that glycolysis and TCA cycle activity are inhibited by FBP2 restoration. Additionally, RNA-seq analysis indicates that mitochondrial function and oxidative phosphorylation (OXPHOS) gene signatures are significantly repressed by FBP2. Both FBP1 and FBP2 isozymes share a consensus nuclear localization sequence (NLS) (Gizak et al., 2009a; 2009b), and a nucleus-excluded FBP2 mutant has no effect on mitochondrial biogenesis and OXPHOS, indicating that nuclear FBP2 regulates mitochondrial function independent of its enzymatic activity. Finally, we determined that FBP2 co-localizes with c-Myc at the promoter region

of *TFAM*, which encodes a master regulator of mitochondrial biogenesis, and inhibits c-Myc-mediated *TFAM* expression.

Table 1. Summary of metabolic enzymes with non-canonical functions.

Enzymes	Canonical functions	Non-canonical functions	Refs
Hexokinase 2 (HK2)	Phosphorylate glucose to glucose 6-phosphate (G6P)	Represses the expression of genes involved in glucose repression	(Ahuatzi et al., 2004; Cheung et al., 2012; Chiara et al., 2008; Gottlob et al., 2001; La Cera et al., 2002; Majewski et al., 2004; Neary and Pastorino, 2013; Pastorino et al., 2002)
		Mitochondrial HK2 protect cells from apoptosis by regulating the mitochondrial permeability transition pore and by limiting the production of reactive oxygen species	
Phosphoglucose isomerase (PGI)	Interconvert G6P to fructose 6-phosphate (F6P)	Acts as an autocrine factor extracellularly to elicit cell migration and proliferation	(Ahmad et al., 2011; Fu et al., 2011; Funasaka et al., 2007a; 2007b; Sun et al., 1999; Watanabe et al., 1996)
Phosphofructokinase (PFK)	Phosphorylate F6P to fructose 1, 6-bisphosphate (F1, 6BP)	Nuclear PFK1 binds to transcription factor TEAD and stabilizes its interaction with YAP/TAZ and promotes gene expression	(Enzo et al., 2015)
6-phosphofructose-2-kinase/fructose-2, 6-bisphosphatase 3 (PFKFB3)	Interconvert F6P to fructose 2, 6-bisphosphate (F2, 6BP)	Nuclear PFKFB3 promotes cell-cycle progression by upregulating cell-cycle protein expression and downregulating cell-cycle inhibitor p27	(Yalcin et al., 2014; 2009)
Fructose-1, 6-bisphosphatase 1 (FBP1)	Hydrolyze F1, 6BP to F6P	Nuclear FBP1 binds to HIFs and inhibits its transcriptional activation of glycolytic gene expression	(Li et al., 2014)
Aldolase A	Split F1, 6BP to dihydroxyacetone phosphate (DHAP) and glyceraldehyde 3-phosphate (G3P)	Nuclear aldolase A is involved in the cytokinesis through its interaction with F-actin and Wiskott-Aldrich Syndrome Protein (WASP) family proteins	(Buscaglia et al., 2006; Kao et al., 1999; Ritterson Lew and Tolan, 2012)
Glyceraldehyde 3-phosphate dehydrogenase (GAPDH)	Interconvert G3P to 1, 3-bisphophoglycerate (1, 3BPG)	Binds to colony-stimulating factor-1 (CSF-1) mRNA and stabilizes its transcripts	(Grosse et al., 1986; Hara et al., 2005; Ishitani et al., 1996; Ishitani and Chuang, 1996; Sen et al., 2009; 2008; Sundararaj et al., 2004; Zheng et al., 2003; Zhou et al., 2008)
		GAPDH is a key component in OCA-S complex, mediates its activation of H2B during S phase and promotes cell-cycle progression	
		Protects telomeres against rapid shortening	
		Increases DNA synthesis during S phase via direct binding to ssDNA and stimulating the DNA-polymerase-α-primase complex	
		GAPDH *S*-nitrosylation promotes its nuclear translocation and triggers apoptosis	
		Mitochondrial GAPDH facilitates apoptosis via inducing mitochondrial membrane permeabilization (MOMP) and	

		subsequent release of cytochrome c and AIF	
Phosphoglycerate kinase (PGK)	Interconvert 1, 3BPG to 3-phosphoglycerate (3PG)	Recognizes primer and robustly stimulates DNA synthesis catalyzed by DNA polymerase α and ε	(Kumble and Vishwanatha, 1991; Popanda et al., 1998)
Enolase 1 (ENO1)	Interconvert 2-phosphoglycerate to phosphoenolpyruvate (PEP)	*MYC* binding protein-1 (MBP-1) transcribes from the same gene as ENO1; MBP-1 binds to *MYC* and represses its expression by recruiting histone deacetylase (HDAC)	(Feo et al., 2000; Ghosh et al., 1999a; 1999b; Hsu et al., 2008; Wang et al., 2005)
		MBP-1 attenuates Notch1-mediated c-Myc activation by interacting with activated Notch1 receptor, N1IC	
Pyruvate kinase 2 (PKM2)	Transfer a phosphate group from PEP to ADP to yield pyruvate and ATP	Acts as a binding partner of Oct-4 and enhances its transcriptional activity	(Gao et al., 2012; Hosios et al., 2015; Jiang et al., 2014a; 2014b; Lee et al., 2008; Li et al., 2015; Luo et al., 2011; Wang et al., 2014; Yang et al., 2012a; 2011; 2012b)
		Interacts with HIF1α and increases p300 recruitment to HIF target gene	
		Upon EGFR stimulation, PKM2 binds to β-catenin and co-activates cyclin D1 and c-Myc	
		Kinase activity (controversial): PKM2 phosphorylates a variety of proteins, such as stat3, Histone H3, Bub3 and myosin light chain 2 (MLC2). PKM2 promotes G1/S transition by promoting cyclin D1 and c-Myc expression and chromosome segregation by phosphorylating spindle checkpoint protein Bub3	
		In yeast, Pyk1 (yeast PKM2) forms the SESAME complex. SESAME interacts with Set1 methyltransferase and controls H3K4me3	
Lactate dehydrogenase A (LDHA)	Interconvert lactate to pyruvate	Forms OCA-S complex with GAPDH and regulates cell-cycle progression	(Castonguay et al., 2014; Popanda et al., 1998; Zheng et al., 2003)
		Activates SIRT1 by supplementing NAD^+	
		Binds to ssDNA and facilitates DNA replication by recruiting with DNA polymerase α, δ, and ε	
Aconitase	Interconvert citrate to isocitrate in the TCA cycle	In yeast, aconitase (Aco1p) is essential for mtDNA maintenance	(Chen et al., 2005)
Succinyl-CoA synthase (SCS)	Interconvert sucinyl-CoA to succinate in the TCA cycle	SCS-A is associated with mtDNA maintenance	(Phillips et al., 2009)
Fumarase	Interconvert fumarate to malate in the TCA cycle	Participates in DNA damage repair in an enzymatic activity dependent manner	(Jiang et al., 2015; Yogev et al., 2010)
Malate dehydrogenase (MDH)	Interconvert malate to	Increases p53 stabilization and transcriptional activity by	(Lee et al., 2009; McEwen et al., 1963)

	oxaloacetate in the TCA cycle	facilitating its phosphorylation and acetylation	
Pyruvate dehydrogenase complex (PDC)	Convert pyruvate to acetyl-CoA	Produces acetyl-CoA in the nucleus and increases histone acetylation	(Cai et al., 2011; Kim et al., 2006; Sutendra et al., 2014)
		Promotes cell-cycle progression by increasing acetylation of histones important for G1/S transition and activating S-phase regulator expression (P-Rb, E2F, cyclin A, and Cdk2)	
ATP-citrate lyase (ACLY)	Convert citrate to oxaloacetate and acetyl-CoA	Produces acetyl-CoA and increases histone acetylation	(Lee et al., 2014; Sivanand et al., 2017; Wellen et al., 2009)
		Upon DNA damage, nuclear ACLY promotes homologous recombination	
Acetyl-CoA synthetase short-chain family member 2 (ACSS2)	Catalyze acetate to acetyl-CoA	Forms a complex with TFEB and increases lysosomal and autophagy gene expression by local histone acetylation	(Cheng et al., 2015; Li et al., 2017a; 2017b; Zhao et al., 2016)
		Provides acetyl-CoA for lysine acetyltransferase CREB-binding protein (CBP)-mediated HIF-2α acetylation	
Methionine adenosyltransferase IIα (MATIIα)	Produce S-adenosylmethionine (SAM) from methionine	Forms a complex with Maf and represses HO-1 expression by increasing histone methylation and recruiting chromatin corepressors	(Katoh et al., 2011)
Serine hydroxymethyltransferase (SHMT)	Interconvert L-serine to glycine and tetrahydrofolate to 5, 10-methylenetetrahydrofolate	Directs deubiquitinating complex BRISC to IFAR1 and protects it from lysosomal degradation and promotes IFNAR1 signaling	(Zheng et al., 2013)

CHAPTER 2 MATERIALS AND METHODS

Cell culture

LPS224, LPS246, T449, T778, T1000, SW872, HT1080, KP250 and 293T cells were tested to confirm they are mycoplasma negative, and cultured in DMEM (Life Technologies, 11965-084) containing 10% FBS (Gemini, 900-108). C2C12 myoblasts (ATCC, CRL-1772) were propagated in DMEM containing 20% FBS. To evaluate differentiation, myoblasts were grown to 80 to 90% confluence and switched to 2% horse serum (Life Technologies, 16050-122) in DMEM. For metabolic labelling assays, cells were maintained in glucose-free DMEM (Life Technologies, 11966-025) supplemented with 10% dialyzed FBS (Gemini, 100-108) and 10 mM [1, 2-^{13}C]glucose (Sigma-Aldrich, 453188), or supplemented with 10% dialyzed FBS and 2 mM [3-^{13}C]sodium pyruvate (Sigma-Aldrich, 490733). Human skeletal muscle myoblasts (HSMM, Lonza, CC-2580) were culture in SkBM-2 Basal Medium (Lonza, CC-3246), supplemented with SkGM-2 SingleQuots containing GA-1000, human Epidermal Growth Factor, Dexamethasone and L-glutamine (Lonza, CC-3244). Differentiation should be initiated when the plated myoblasts reach 80-90% confluence and differentiation medium (DMEM with 2% horse serum) was added to the plates and changed every 2-3 days. All cells were incubated at 37°C and 5% CO_2.

Mice

Xenograft tumor experiments were approved by the Animal Care and Use Committee at the University of Pennsylvania. Briefly, ten female NSG mice (the Jackson Laboratory, 6 weeks, 005557) were injected subcutaneously into both flanks with 2 million LPS246 cells stably expressing TetOne-FBP2. Before injection, cells were resuspended in 100 μl PBS mixed with an equal volume of Matrigel (Corning, 356234). Once palpable tumors were established, tumor volume was measure with a digital caliper. When the average tumor size reached 100 mm^3, ten mice were randomly separated into two groups: (1) Doxycycline diet (Bio-Serv, S3888) and (2) control diet (Bio-Serv, S4207). Upon completion of the experiment, the animals were sacrificed by CO_2 inhalation and xenograft tumors were dissected for downstream analyses.

Constructs and Viral Transduction

Lentivirus was produced by transfecting 2.5×10^6 HEK293 cells with the 10 μg indicated expression plasmid, 2.5 μg pRSV-Rev, 6.5 μg pMDL, and 3.5 μg pCMV-VSV-G plasmids (4^{th} generation lentiviral system) using FuGENE 6 Transfection Kit (Promega, E2691). The virus was harvested 48 h after transfection by filtering the virus-containing medium through Amicon Ultra-15 Centrifugal Filter (Millipore, UFC901024). Virus infection was performed by incubating cells with medium containing indicated virus and 8 μg/ml polybrene (Sigma, 107689) for 24 h. Cells were allowed to recover in complete medium for 24 h and then selected with puromycin for 48 h. Surviving pools were subjected to indicated experiments.

Sequence verified cDNA constructs were obtained from the Mammalian Gene Collection (GE Dharmacon) and were subcloned into the pCDH-CMV-MCS-EF1-Puromycin mammalian expression vector (System Biosciences CD510B-1) and pLVX-TetOne-Puro (Clontech, 631847). FBP2 cDNA construct: MHS6278-211687897 (Accession, BC117477). The $FBP2^{4KA}$ and $FBP2^{G260R}$ mutants were generated using Q5 Site-Directed Mutagenesis Kit (NEB, E0554). $FBP2^{4KA}$ Forward primer: 5'- caggagcgatttacagcctgaatgag-3', Reverse primer: 5'-ccgccgcaatcttgacatctttttccac-3'. $FBP2^{G260R}$ Forward primer: 5'-cctggtctatagaggaatcttcctgtaccc-3', Reverse primer: 5'-gtgcggtgcacgtcagcc-3'.

RNA Interference

LPS246 cells were plated in 6-well plate at a density of 2.5×10^5 cells per well. siRNA pools targeting human c-Myc (sc-29226) was obtained from Santa Cruz Biotechnology and non-targeting pool control (D-001810-10-05) was obtained from Dharmacon. For each well, 100 μl OPTI-MEM (Thermo Fisher Scientific, 31985062), 24 μl sic-Myc or non-targeting pool control (10 nM) and 12 μl HiPerfect transfection reagent (Qiagen, 301705) were mixed and incubated before loaded to the plate.

Cell Growth Assays

Multiple cultures of LPS246, T1000, SW872, and KP250 cells were plated in 60 mm plates at a density of 8×10^4 cells supplemented with DMEM containing 1% FBS. Every other day, one set of cultures was collected and counted. Multiple cultures of LPS246, T1000, SW872, and HT1080 cells were plated in 60 mm plates at a density of 5×10^4 cells with either glucose-free DMEM supplemented with 10% FBS and 5 mM D-(+)-Glucose (Sigma-Aldrich, G8270) or DMEM containing 10% FBS. Every day, one set of cultures was collected and counted every day.

Anchorage-Independent Growth Assay

Sarcoma cells (SW872, HT1080, KP250) stably expressing FBP2 or vector control were plated in 6-well plates at a density of 6,000 cells per well in complete medium containing 0.3% agarose (low-melt 2-hydroxyethylagarose, Sigma-Aldrich, A4018), onto underlays composed of medium containing 0.6% agarose. Additional media was added to the cultures once per week, and after two weeks of growth the colonies were quantified.

Western Blot Analysis

Cells were harvested in lysis buffer (150 mM NaCl, 10 mM Tris pH 7.6, 0.1% SDS and 5 mM EDTA) containing Halt Protease and Phosphatase Inhibitor Cocktail (Thermo Fisher Scientific, 78445). For western blots of xenograft tissue, approximately 20-30 mg of tissue was suspended in 500 μl lysis buffer and homogenized on ice using a Tissue-Tearor (Biospec, 985370). Samples were centrifuged at 12,000 rpm for 20 min at 4 °C. Protein lysates were resolved by Tris-Glycine SDS-PAGE and were transferred to nitrocellulose membranes (Bio-Rad, 162-0115, 0.45 μm pore size for all experiments). All membranes were incubated with the indicated primary antibodies overnight at 4 °C and were diluted in TBST (20 mM Tris pH 7.5, 150 mM NaCl, 0.1% Tween-20) supplemented with 5% bovine serum albumin (BSA, Sigma-Aldrich, A7906). Primary antibodies were detected with horseradish peroxidase-conjugated secondary antibodies followed by exposure to ECL reagents.

Co-Immunoprecipitation

LSP246 cells expressing FBP2 or FBP2^{4KA} were incubated in Co-IP lysis buffer (20 mM Tris HCl pH 8, 137 mM NaCl, 1% NP-40 and 2 mM EDTA) supplemented with Halt Protease and Phosphatase Inhibitor Cocktail for 20 min at 4 °C. Collect the lysates and centrifuge at 12,000 rpm for 10 min at 4 °C**.** Transfer the supernatant to a clean tube and save 1/10 lysate as input. Pre-clean the rest lysate by adding 50 μl Protein Agarose A/G bead slurry (Thermo Fisher Scientific, 20421) and 2 μl mouse IgG (Cell Signaling Technology, #5415) and rotate at 4 °C for 2 hours. Spin down the beads. The lysates were evenly separated and incubated with IgG or V5 antibody (Thermo Fisher Scientific, #R960-25) at 4 °C overnight. 35 μl Protein Agarose A/G bead slurry was incubated with lysates for additional 2 hours. Wash the beads with Co-IP lysis buffer three times and add 2 × loading buffer (0.5 M Tris-HCl pH 6.8, 4.4% SDS, 20% glycerol, 2% 2-mercaptoethanol, 0.1% bromophenol blue) to elute the bound proteins.

GST pull-down

The cDNA fragment of c-Myc was obtained from Addgene (102626) and was amplified and cloned into pGEX fusion with glutathione S-transferase (GST) as the bait using primers (F: CGC GGATCCATGGATTACAAGGATGACGACGATAAG, R: CCGGAATTCTTACGCACAAGAGTTCC GTAGCT). FBP2 cDNA construct: MHS6278-211687897 (Accession, BC117477) was cloned into pET-28a (+) plasmid as the prey for fusion with His-tag using the indicated primers (F: CGCGGATC CATGACGGACAGAAGCCCCTTC, R: CCGGAATTCTCAATGGTGATGGTGATGATGACCGG). Both bait and prey recombinant proteins were used to transform E. coli strain BL-21 for protein expression. Both bait and prey proteins were blocked using 4% BSA (final concentration 0.8%) at 4 °C for 30 min. Combine both proteins with 60 μl Glutathione Sepharose 4B (17075601) and rotate at 4 °C for 2 hours. Wash beads twice with PBS + 0.5% NP-40, once with PBS + 0.5% NP-40 + 300 mM KCl and twice with PBS + 0.5% NP-40. Resuspend the beads with 30 μl 2 × loading buffer and boil the samples at 95 °C for 10 min.

Quantitative RT-PCR

Total RNA was isolated from cells using the RNAeasy purification kit (Qiagen, 74104). cDNA was synthesized using a High Capacity RNA-to-cDNA kit (Applied Biosystems, 4368814). qRT-PCR was performed on a ViiA7 Real-Time PCR system from Applied Biosystems. Pre-designed Taqman primers were obtained from Life Technologies for the following genes: 18S (HS03928985_G1), MT-ND1 (HS02596873_S1), MT-MYB (HS02596867_S1), MT-CO1 (HS02596864_G1), and MT-ATP6 (HS02596862_G1), c-Myc (Hs00153408_m1), CCND2 (Hs00153380_m1), eIF2A (Hs00230684_m1), NPM1 (Hs02339479_g1), PSAT1 (Hs00795278_mH).

Chromatin Immunoprecipitation (ChIP) and ChIP-reChIP Assay

ChIP and ChIP-reChIP were performed as described previously (Si et al., 2015). Briefly, cells were cross-linked using 1% formaldehyde at room temperature for 10 min. The cross-linking reaction was quenched by glycine. Cells were lysed in SDS buffer containing protease inhibitor cocktail and lysates were sonicated at 4 °C (30s on and 30s off, 15 cycles). The sheared chromatin was precleared, and then subjected to immunoprecipitation with 5 μg IgG (Cell Signaling Technology, 5415) and V5 (Thermo Fisher Scientific, R960-25) antibodies. After washing with low- and high-salt buffers, immunoprecipitated DNA fragments were eluted and purified with the QIAquick PCR Purification Kit and then analyzed by qRT-PCR. For ChIP-reChIP, the first ChIP was performed using c-Myc antibody (Santa Cruz Biotechnology, sc-40x), until the washing steps. The immunoprecipitated protein-DNA complexes were incubated in ChIP-reChIP elution buffer (10 mM Tris-HCl, pH 8.0, 2 mM EDTA, 2% SDS, 15 mM DTT, supplemented with protease inhibitor cocktail) for 30 min at 37 °C. The isolated supernatant was diluted at least 20 times and subjected to the second ChIP using 5 μg IgG or V5 antibodies.

mtDNA Content

Total DNA was extracted from cell samples using Wizard Genomic DNA Purification Kit (Promega, A1120) according to the manufacturer's instructions. To quantify mtDNA copy number,

real-time PCR was performed using a on a ViiA7 Real-Time PCR system from Applied Biosystems against MT-ND1 (HS02596873_S1) as the standard for mtDNA. The β-globin (HBB) was used as the nuclear gene (nDNA) normalizer for calculation of the mtDNA/nDNA ratio, as previously described (Dickinson et al., 2013). A fragment of HBB gene was amplified using forward primer, 5'-caacttcatccacgttcacc-3', and reverse primer, 5'-gaagagccaaggacaggtac-3'. The relative mtDNA content was calculated using the formula: mtDNA content = $1/2^{\Delta Ct}$, where $\Delta C_t = C_t^{mtDNA} - C_t^{HBB}$.

Subcellular Fractionation

Cytosolic and nuclear fractionation of indicated cells were performed using NE-PER nuclear and cytoplasmic extraction reagents (Thermo Fisher Scientific, 78833) by following the manufacturer's protocol. Briefly, cells were trypsinized, washed using PBS and pelleted. Depending on the volume of cell pellet, the ratio of CER I, CER II and NER were maintained at 200:11:100 μl (for 20 μl cell pellet). Halt Protease and Phosphatase Inhibitor Cocktail (Thermo Fisher Scientific, 78445) was added to CER I and NER. Cells were first incubated with CER I for 10 min, followed by CER II for 1 min and centrifuged at 12,000 rpm for 5 min at 4 °C. The supernatant was saved as cytoplasmic extract and the insoluble fraction was suspended in NER. Vortex for 15s every 10 min, for a total of 40 min. Centrifuge at 12,000 rpm for 10 min at 4 °C and the supernatant is the nuclear extract.

FBP2 Enzymatic Activity Assay

Vector control 293T cells, or 293T cells expressing FBP2, $FBP2^{4KA}$ or $FBP2^{G260R}$ were harvested in lysis buffer used for western blot analysis. 20 μg lysates were added to 100 μl reaction buffer containing 50 mM Tris (pH 6.8), 10 mM $MgCl_2$, and 100 μM D-fructose 1,6- bisphosphate trisodium salt (Sigma-Aldrich, F6803). The reaction was started by incubating solutions at 37 °C for 15 min and stopped by a deproteinization protocol using Deproteinizing Sample Preparation Kit (BioVision, K808). FBP2 catalytic activity was quantified according to the yield of fructose 6-phosphate (enzyme product), measured by Fructose-6-Phosphate Fluorometric Assay Kit (BioVision, K689-100).

Cell Apoptosis Assay

LPS246 TetO-FBP2 (PBS or Dox treated) and LPS246 TetO-FBP2^{4KA} (PBS or Dox treated) cells were seeded in 6-well plates at a density of 1.5×10^5 per well. These cells were incubated in 5 mM glucose medium (glucose-free DMEM, 10% FBS, 5 mM glucose) or 5 mM galactose medium (glucose-free DMEM, 10% FBS, 5 mM galactose). After 24 h, cells and supernatant were collected and centrifuged. The cell pellet was suspended with 110 μl binding buffer. Cells were then stained with the FITC-Annexin V Apoptosis Detection Kit (BD Biosciences, 556547) with Annexin V Alexa Fluor 488 and propidium iodide (PI) and incubated for 15 min at room temperature in the dark. After incubation, 400 μl of binding buffer was added and cells were analyzed by flow cytometry using the BD Accuri C6 instrument. Double-negative cells were determined viable.

MitoTracker and MitoSox Staining

LPS246 TetO-FBP2 (PBS or Dox treated) and LPS246 TetO-FBP2^{4KA} (PBS or Dox treated) cells were seeded in 6-well plates at a density of 1.5×10^5 per well. Cells were incubated with 5 μM MitoSox reagent (Thermo Fisher Scientific, M36008) or 25-100 nM MitoTracker Green FM probe (Thermo Fisher Scientific, M7514) at 37 °C for 30 min. Save one well of cell without staining as the negative control. After staining was complete, the cells were gently washed three times with warm PBS. Detach cells from plates and ensure a single cell suspension. Analyze the samples by flow cytometry using BD Accuri C6.

ATP Measurements

ATP production was measured using the ATP Determination Kit (Thermo Fisher Scientific, A22066) according to the manufacturer's protocol. Briefly, cells were homogenized in lysis buffer (1% Triton X-100, 0.1% SDS, 150 mM NaCl, 50 mM Tris-HCl pH 7.5) supplemented with protease and phosphatase inhibitor cocktail (Thermo Fisher Scientific, 78445). Data were determined by luminescence (Promega, Glomax 20/20 luminometer). Data were collected from multiple replicate wells for each experiment and were normalized to protein concentration.

Citrate Synthase Activity

Citrate synthase activity was measured on total cell extracts by Citrate Synthase Activity Assay Kit (Abcam, ab119692). In brief, 100 μl of cell lysates was added to the pre-coated microplate strips, sealed, and incubated at room temperature for 3 hours. The wells were aspirated and washed twice with 300 μl wash buffer. Activity solution was added to the well and the plate was immediately read every 20 seconds for 30 min at a wavelength of 412 nm using a plate reader (BioTek, Synergy H1).

Immunohistochemistry

LPS246 tumor sections and tissue microarray slides (US Biomax, SO801b) were deparaffinized by baking slides at 60 °C for 30 min. The slides were rehydrated in series of ethanol solutions and endogenous peroxidase activities were quenched by 1% H_2O_2 in distilled water for 20 min. After three washes in TT buffer (500 mM NaCl, 10 mM Trizma, and 0.05% Tween-20), antigen retrieval was performed by boiling slides for 20 min in a citrate-based antigen unmasking solution (Vector labs, H3300). After cooling down to room temperature, slides were blocked in 2% normal goat serum and 4% BSA in TT buffer for 1 h. Next, tissue slides were incubated with various primary antibodies at 4 °C overnight. After three washes in TT buffer, biotinylated secondary antibody was added onto these slides for 1 h, following by 1 h treatment of the Vectastain Elite ABC reagents (Vector Labs, PK-6100). After three TT washes, the slides were processed with DAB peroxidase substrate kit (Vector Labs, SK-4100), and hematoxylin solutions for immunohistochemistry staining, dehydrated in a standard ethanol/xylene series, and mounted in 75% v/v Permount (Fischer Scientific, SP15-500) in xylenes.

Tissue Immunofluorescence

LPS246 tumors were fixed in 4% paraformaldehyde (PFA)/PBS overnight at 4 °C. Fixed tissues were dehydrated in 30% sucrose solution and embedded in OCT for frozen sectioning. Tissue samples were submitted to the Molecular Pathology & Imaging Core (MPIC) at the University of Pennsylvania for processing and sectioning. Frozen sections were rinsed in cold PBS to remove OCT, and then incubated with 0.25% Triton-X-100 in PBS for 10 min at room temperature. The

slides were incubated in a blocking buffer (4% BSA, 2% serum in PBS) for 1 h at room temperature. The slides were then incubated with diluted primary antibodies in blocking buffer overnight at 4 °C. After washing in PBS, the slides were further incubated with fluorescein-conjugated secondary antibodies diluted in blocking buffer for 1 hour at room temperature. The slides were finally mounted with ProLong Diamond Antifade Mountant with DAPI (Thermo Fisher Scientific, P36962). Slides were examined and images were captured on a Leica DM5000B microscope.

Cell Immunofluorescence

Cells were plated in 2-well Chamber Slides (Lab-Tek, 154461). After 24 h, the cells were washed three times with PBS and fixed for 20 min in 4% paraformaldehyde at room temperature. Cells were permeabilized in PBS containing 0.5% Triton X-100 and blocked in PBS containing 5% BSA (blocking buffer). Primary antibodies against FBP2 (Abcam, ab131253) and secondary antibodies (Thermo Fisher Scientific, Alexa Fluor 488) were diluted in blocking buffer. Slides were washed three times in PBS, rinsed in H_2O, and mounted on slides using VectaShield mounting medium containing 4'6'-diamidino-2-phenylindole (DAPI) (Vector Labs, H-1200).

Metabolic Quantification

The rate of glucose uptake and lactate secretion was determined using Multiparameter Bioanalytical System (YSI Life Sciences, YSI 2950). Briefly, cells were seeded in 6 cm plates starting with 4 replicates. The next day, the medium was changed to 10 mM glucose medium (glucose-free and glutamine-free DMEM, 10% dialyzed FBS, 10 mM glucose, 2 mM glutamine). Cells in one replicate ware trypsinized and counted. The cell number was labeled as Q1 (starting cell number). 24 h later, culture medium was collected and read by YSI analyzer. Cell number was counted as Q2 (final cell cell number). Measurements were normalized to cell number area under the curve, as previously described (Gentile et al., 2013). Metabolite consumption was defined as $v = V(x_{medium\ \ control} - x_{final})/A$, where v is metabolite consumption/production, V is culture volume, x is metabolite concentration, and A is cell number area under the curve. A was calculated as $N(T)d/ln2(1 - 2^{-T/d})$, where $N(T)$ is the final cell count, d is doubling time, and T is time of experiment. Doubling time was calculated as $d = (T)[log(2)/log(Q2/Q1)]$.

^{13}C-metabolic Flux Analysis

Cells were seeded to 10 cm plates at a density of 1 million cells per plate. For [1,2-^{13}C]glucose labeling, cells were incubated in 10 mM [1,2-^{13}C]glucose medium (glucose-free DMEM, 10% FBS, 10 mM [1,2-^{13}C]glucose) for 24 h. For [3-^{13}C]pyruvate labeling, cells were incubated in 2 mM [3-^{13}C]pyruvate medium (glucose-free DMEM, 10% FBS, 2 mM [3-^{13}C]pyruvate) for 6 h. To measure the ^{13}C enrichment in TCA cycle intermediates, [1,2-^{13}C]glucose-labelled or [3-^{13}C]pyruvate-labelled cells were extracted by 4% perchloric acid (PCA). Briefly, cells were washed twice with ice-cold PBS and then scraped in 4% PCA on dry ice, which was then freeze-thawed for three cycles. Cell extracts were neutralized using 5 M KOH and analyzed as previously described (Nissim et al., 2012). The neutralized PCA extract were subjected to an AG-1 column (100-200 mesh, 0.5 $\times$ 2.5 cm, Bio-rad) for enriching the organic acids, glutamate and aspartate, which were then converted to *t*-butyldimethylsilyl derivatives. The production of ^{13}C-labeled metabolites was measured using GC-MS. Isotopic enrichment in [^{13}C]glutamate isotopomers was monitored using ions at *m/z* 432, 433, 434, 435, 436 and 437 for M0, M1, M2, M3, M4 and M5 (containing 1 to 5 ^{13}C atoms above M0, the natural abundance), respectively. Isotopic enrichment in [^{13}C]aspartate isotopomers was monitored using ions at *m/z* 418, 419, 420, 421 and 422 for M0, M1, M2, M3 and M4 (containing 1 to 4 ^{13}C atoms above M0, the natural abundance), respectively. Isotopic enrichment in [^{13}C]lactate was determined using ions at *m/z* 261, 262, 263 and 264 for M0, M1, M2 and M3 (containing 1 to 3 ^{13}C atoms above natural abundance), respectively. Isotopic enrichment in [^{13}C]pyruvate isotopomers was monitored using ions at *m/z* 259, 260, 261 and 262 for M0, M1, M2 and M3 (containing 1 to 3 ^{13}C atoms above M0, the natural abundance), respectively. Isotopic enrichment in [^{13}C]malate isotopomers was monitored using ions at *m/z* 419, 420, 421, 422 and 423 for M0, M1, M2, M3 and M4 (containing 1 to 4 ^{13}C atoms above M0, the natural abundance), respectively, and ^{13}C enrichment in [^{13}C]citrate isotopomers was assayed using ions at *m/z* 459, 460, 461, 462, 463, 464 and 465 for M0, M1, M2, M3, M4, M5 and M6 (containing 1 to 6 ^{13}C atoms above M0, the natural abundance), respectively.

Quantification of the Pentose Phosphate Pathway (PPP)

Metabolic flux going through the PPP was quantified as previously described (Lee et al., 1998), using [1,2-^{13}C]glucose as the labelling tracer. Briefly, direct glycolysis of [1,2-^{13}C]glucose (without going through the PPP) produces M2-labelled lactate, while flux going through the oxidative portion of PPP removes the first carbon from glucose and releases it in the form of CO_2. The resultant M1-labelled intermediates are recycled back to glycolysis to produce M1-labelled lactate through the non-oxidative potion of PPP. The ratio of M1 to M2-labelled lactate indicates the ratio of flux going through the PPP versus flux directly going through glycolysis. Therefore, PPP flux was calculated based on the following formula: PPP flux = glucose consumption $\times$ M1 lactate enrichment / (M1 lactate enrichment + M2 lactate enrichment). Calculated PPP flux was then normalized to vector control cells by setting the vector control flux equal to 1.

Seahorse XF Cell Mito Stress Analysis

The mitochondrial respiratory capacity was determined using XF Cell Mito Stress Test Kit (Agilent Technologies, 103015-100). Cells were seeded in the XF96 Cell Culture Microplate at a density of 2×10^4 cells per well. 6 replicates were set up for each of the following groups: (1) LPS246 TetO-FBP2 + Veh; (2) LPS246 TetO-FBP2 + Dox; (3) LPS246 TetO-FBP2^{4KA} + Veh; (4) LPS246 TetO-FBP2^{4KA} + Dox. Microplate was incubated for 24 h at 37 °C. Seahorse XF96 FluxPak sensor cartridge was hydrated in the utility plate filled with 200 μl of Seahorse Calibrant overnight in a non-CO_2 incubator at 37 °C. Next day, cells were incubated with the base medium containing 2 mM L-glutamine, 1 mM sodium pyruvate, and 10 mM glucose for 1 hour prior to assay. The oxygen consumption rate (OCR) was measured by XFe96 extracellular flux analyzer with sequential injection of 1 μM oligomycin A, 1 μM FCCP, and 0.5 μM rotenone/antimycin A. After the experiment, cells lysates were harvested with 20 μl western blot lysis buffer and protein concentration was quantified using Pierce BCA Protein Assay Kit (Thermo Fisher Scientific, 23225). OCR value was normalized to the protein concentration in each well.

Quantification and Statistical Analysis

All statistical analyses were conducted using GraphPad Prism 7.0. All error bars are presented as mean ± s.d. unless otherwise specified. Data were reported as biological replicates. *P* values were calculated based on two-tailed, unpaired Student's *t*-tests. Significance was defined as *p < 0.05, **p < 0.01, ***p < 0.001, ****p < 0.0001.

Table 2. Key resources table.

REAGENT or RESOURCE	SOURCE	IDENTIFIER
Antibodies		
Rabbit monoclonal anti-FBP2	Abcam	#ab131253
Rabbit polyclonal anti-FBP2 for IHC	Sigma-Aldrich	#HPA012513
Mouse polyclonal anti-FBP1	Sigma-Aldrich	#SAB1405798
Rabbit polyclonal anti-PCK1	Abcam	#ab28455
Rabbit polyclonal anti-G6PC	Abcam	#ab83690
Rabbit monoclonal anti-GAPDH	Cell Signaling Technology	#2118
Mouse monoclonal anti-HDAC1	Cell Signaling Technology	#5356
Rabbit monoclonal anti-HSP90	Cell Signaling Technology	#4877
Rabbit polyclonal anti-Phospho-Histone H3	Cell Signaling Technology	#9701
Anti-rabbit IgG HRP-linked	Cell Signaling Technology	#7074
Anti-mouse IgG HRP-linked	Cell Signaling Technology	#7076
Mouse (G3A1) mAb IgG1 Isotype Control	Cell Signaling Technology	#5415
Normal Rabbit IgG	Cell Signaling Technology	#2729
NRF1 (D9K6P) Rabbit mAb	Cell Signaling Technology	#46743
Rabbit monoclonal anit-VDAC1	ABclonal	#A11242
Rabbit polyclonal anti-TOMM20	ABclonal	#A6774
TFAM Polyclonal Antibody	ABclonal	#A13552
Biotinylated Goat anti-Rabbit IgG	Vector Labs	#BA-1000
Mouse monoclonal anti-V5 Tag	Thermo Fisher Scientific	#R960-25
Goat anti-Rabbit IgG (H+L) Secondary Antibody, Alexa Fluor 488 conjugated	Thermo Fisher Scientific	#A-11008
c-Myc Monoclonal Antibody (9E10)	Thermo Fisher Scientific	#13-2500
Biological Samples		
Soft tissue malignant tumor tissue array	US Biomax	SO801b
Chemicals, Peptides, and Recombinant Proteins		
DMEM	Life Technologies	11965-084
Glucose-free DMEM	Life Technologies	11966-025
Glucose-free and glutamine-free DMEM	Life Technologies	A1443001
L-Glutamine	Life Technologies	25030-081
Sodium Pyruvate	Life Technologies	11360-070
Horse serum	Life Technologies	16050-122
Standard FBS	Gemini	900-108
Dialyzed FBS	Gemini	100-108
HSMM cell growth media (SkGM-2 BulletKit)	Lonza	CC-3245
[1,2-^{13}C]glucose	Sigma-Aldrich	453188
[3-^{13}C]sodium pyruvate	Sigma-Aldrich	490733
D-(+)-Glucose	Sigma-Aldrich	G8270
D-(+)-Galactose	Sigma-Aldrich	G0750
D-fructose 1,6-bisphosphate trisodium salt hydrate	Sigma-Aldrich	F6803
Perchloric acid, 70%	Sigma-Aldrich	311421
Polybrene	Sigma-Aldrich	107689

Doxycycline hydrochloride	Sigma-Aldrich	D3447
2-Hydroxyethyl agarose	Sigma-Aldrich	A4018
Bovine serum albumin	Sigma-Aldrich	A7906
MitoSox	Thermo Fisher Scientific	M36008
Hoechst	Thermo Fisher Scientific	62249
MitoTracker Green FM	Thermo Fisher Scientific	M7514
Propidium Iodide	Thermo Fisher Scientific	P3566
ProLong Diamond Antifade Mountant with DAPI	Thermo Fisher Scientific	P36962
Halt Protease and Phosphatase Inhibitor Cocktail	Thermo Fisher Scientific	78445
FuGENE 6 Transfection Reagent	Promega	E2691
Seahorse XFe96 FluxPaks	Agilent	102601-100
Seahorse XF Base Medium	Agilent	102353-100
Matrigel matrix	Corning	356234
Glutathione Sepharose 4B resin	GE Healthcare	17075601
Doxycycline diet - Sterile	Bio-Serv	S3888
Control diet - Sterile	Bio-Serv	S4207
Critical Commercial Assays		
Seahorse XF Cell Mito Stress Test Kit	Agilent	103015-100
Seahorse XF Glycolysis Stress Test Kit	Agilent	103020-100
Citrate Synthase Activity Assay Kit	Abcam	ab119692
FITC Annexin V Apoptosis Detection Kit	BD Biosciences	556547
Deproteinizing Sample Preparation Kit	BioVision	K808
Fructose-6-Phosphate Fluorometric Assay Kit	BioVision	K689-100
Nuclear and Cytoplasmic Extraction Reagents	Thermo Fisher Scientific	78833
ATP Determination Kit	Thermo Fisher Scientific	A22066
Q5 Site-Directed Mutagenesis Kit	New England BioLabs	E0554
Wizard Genomic DNA Purification Kit	Promega	A1120
RNeasy Mini Kit	Qiagen	74104
High-Capacity cDNA Reverse Transcription Kit	Applied Biosystems	4368814
Experimental Models: Cell Lines		
293T	ATCC	CRL-3216
HT1080	ATCC	CCL-121
C2C12	ATCC	CRL-1772
SW872	ATCC	HTB-92
LPS224	Core Facilities, MD Anderson Cancer Center, Houston, TX	A gift from Dr. Dina Lev
LPS246	Core Facilities, MD Anderson Cancer Center, Houston, TX	A gift from Dr. Dina Lev
T449	Established from a well-differentiated liposarcoma	CVCL_M807

T778	Established from a well-differentiated liposarcoma	CVCL_M808
T1000	Established from a well-differentiated liposarcoma	CVCL_M809
KP250	Derived from UPS mouse tumor	
HSMM	Lonza	CC-2580
Experimental Models: Organisms/Strains		
NOD-*scid* IL2Rgamma^{null} mice	The Jackson Laboratory	005557
Oligonucleotides		
18S	Life Technologies	HS03928985_G1
MT-ND1	Life Technologies	HS02596873_S1
MT-MYB	Life Technologies	HS02596867_S1
MT-CO1	Life Technologies	HS02596864_G1
MT-ATP6	Life Technologies	HS02596862_G1
TFAM	Life Technologies	Hs00273372_s1
NRF1	Life Technologies	Hs00602161_m1
c-Myc	Life Technologies	Hs00153408_m1
CCDN2	Life Technologies	Hs00153380_m1
eIF2A	Life Technologies	Hs00230684_m1
NPM1	Life Technologies	Hs02339479_g1
PSAT1	Life Technologies	Hs00795278_mH
c-Myc siRNA	Santa Cruz Biotechnology	sc-29226
ON-TARGETplus Non-targeting Pool	Dharmacon	D-001810-10-05
β-globin (genomic DNA) Forward: caacttcatccacgttcacc Reverse: gaagagccaaggacaggtac	(Dickinson et al., 2013)	
Recombinant DNA		
pCDH-CMV-MCS-EF1-Puromycin	System Biosciences	CD510B-1
pLVX-TetOne-Puro	Clontech	631847
pLV-EF1a-IRES-Blast	Addgene	85133
pGEX		A gift from Dr. Xiaolu Yang
pET-28a (+)		A gift from Dr. Xiaolu Yang
FBP2 cDNA	Dharmacon	MHS6278-211687897
TFAM cDNA	Dharmacon	MHS6278-211689190
NRF1 cDNA	Dharmacon	MHS6278-202757860
Software and Algorithms		
GraphPad Prism 7.0	GraphPad Software	http://www.graphpad.com
ImageJ	NIH	https://fiji.sc

FlowJo	FlowJo	https://www.flowjo.com/solutions/flowjo
Other		
Seahorse XFe96 Analyzer	Agilent	
YSI 2950	YSI	
Tissue Tearor	Biospec	985370

CHAPTER 3 RESULTS

FBP2 is frequently lost in soft tissue sarcomas

To assess their potential role in regulating sarcoma cell glucose metabolism, we measured the expression levels of three rate-limiting gluconeogenic enzymes, glucose-6-phosphatase catalytic subunit (G6PC), phosphoenolpyruvate carboxykinase 1 (PCK1), and fructose-1,6-bisphosphatase (FBP) using published microarray data from human STS (Barretina et al., 2010; Detwiller et al., 2005). As previously reported (Mizunuma and Tashima, 1990; Tejwani, 1983), *FBP1* is the predominant isozyme in liver, kidney and small intestine (Figure 1A), whereas *FBP2* expression predominates in muscle (Figure 1B). Further analysis revealed that *FBP2* mRNA levels are significantly reduced in liposarcoma, fibrosarcoma, leiomyosarcoma, and UPS samples relative to either normal skeletal muscle (Figure 2A) or adipose tissue (Figure 2B). Moreover, mouse UPS tumors isolated from a previously described autochthonous "KP" (*LSL-Kras*$^{G12D/+}$*; Trp53*$^{fl/fl}$) model (Kirsch et al., 2007; Mito et al., 2009) exhibited decreased FBP2 immunostaining relative to adjacent skeletal muscle tissue (Figure 2C). FBP2 protein abundance was also decreased in a variety of human sarcoma and mouse UPS cell lines, relative to mesenchymal stem cell (MSC) and human skeletal muscle myoblast (HSMM) or mouse C2C12 myoblasts (Figure 2D). Analysis of a representative human sarcoma tissue array showed undetectable FBP2 protein accumulation, compared to normal mesenchymal tissue, in almost 100% of sarcoma tumors examined (n = 70, Figure 3A-C). Even though *FBP2* expression is widely repressed in STS, intertumoral heterogeneity still results in different levels of repression among sarcoma samples, and a liposarcoma data set (Gobble et al., 2011) revealed that lower *FBP2* mRNA levels correlated with worse overall survival in liposarcoma patients (Figure 3D). We concluded that FBP2 loss is a common feature in STS subtypes and may contribute directly to tumorigenesis.

In contrast to *FBP2*, *G6PC* and *PCK1* mRNA levels were similar in liposarcoma, fibrosarcoma, leiomyosarcoma, and other sarcoma subtypes compared with normal skeletal muscle (Figure 4A-C), and liposarcoma cell lines exhibited PCK1 and G6PC protein abundance comparable to control

MSCs (Figure 4D). FBP1 was undetectable in tumors and sarcoma cell lines of diverse histological subtypes or controls, including MSC and human skeletal muscle myoblast (HSMM) (Figure 4E-F).

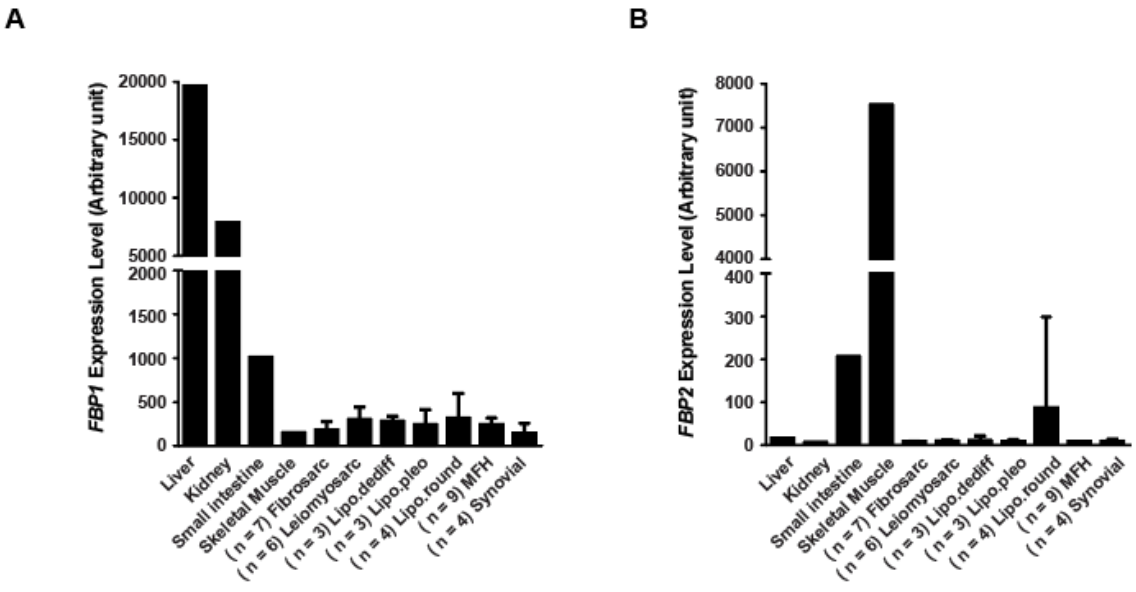

Figure 1. Differential tissue distribution of FBP1 and FBP2.

(A and B) *FBP1* (A) and *FBP2* (B) mRNA expression in multiple normal tissues and a variety of human sarcoma samples. Fibrosarc, fibrosarcoma; Lipo.dediff, dedifferentiated liposarcoma; Lipo.pleo, pleomorphic liposarcoma; Lipo.round, round cell liposarcoma; MFH, malignant fibrous histiocytoma.

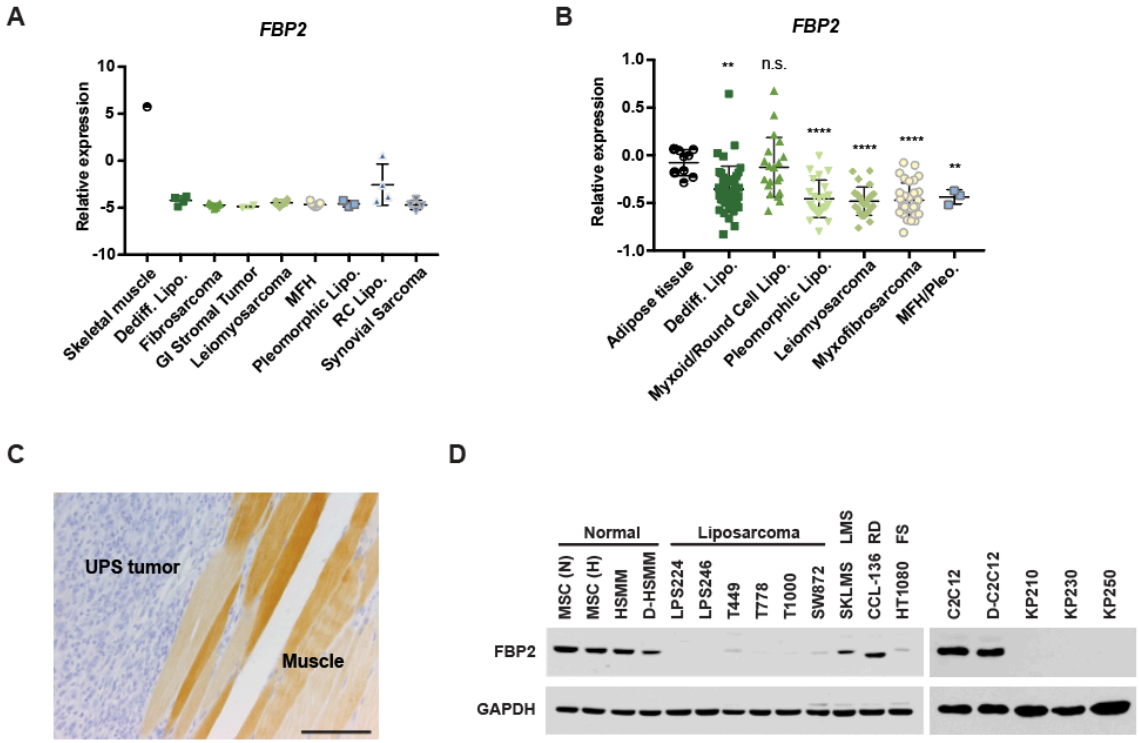

Figure 2. *FBP2* is severely downregulated in a variety of sarcomas.

(A and B) *FBP2* mRNA expression from Oncomine analysis of the (A) Detwiller *et al.* and (B) Barretina *et al.* sarcoma patient samples data set (Barretina et al., 2010; Detwiller et al., 2005). Values are normalized to median-centered intensity and shown on a $\log_2$ scale. Abbreviations: dediff. lipo., dedifferentiated liposarcoma; MFH, malignant fibrous histiocytoma; MFH/Pleo., UPS; pleomorphic lipo., pleomorphic liposarcoma; RC lipo., round cell liposarcoma. *p < 0.05, **p < 0.01, ***p < 0.001, ****p < 0.0001; n.s., not significant.

(C) Representative immunohistochemical (IHC) staining of FBP2 in mouse UPS tumor and surrounding muscle. Scale bars: 100 μm.

(D) Immunoblot analysis of FBP2 protein level in various human (left) and mouse (right) sarcoma cell lines. MSC, HSMM and C2C12 served as normal control. MSC, mesenchymal stem cell; HSMM, human skeletal muscle myoblast; (N), normoxia; (H) hypoxia; D-, differentiated; LMS, leiomyosarcoma; RD, rhabdomyosarcoma; FS, fibrosarcoma. GAPDH served as loading control.

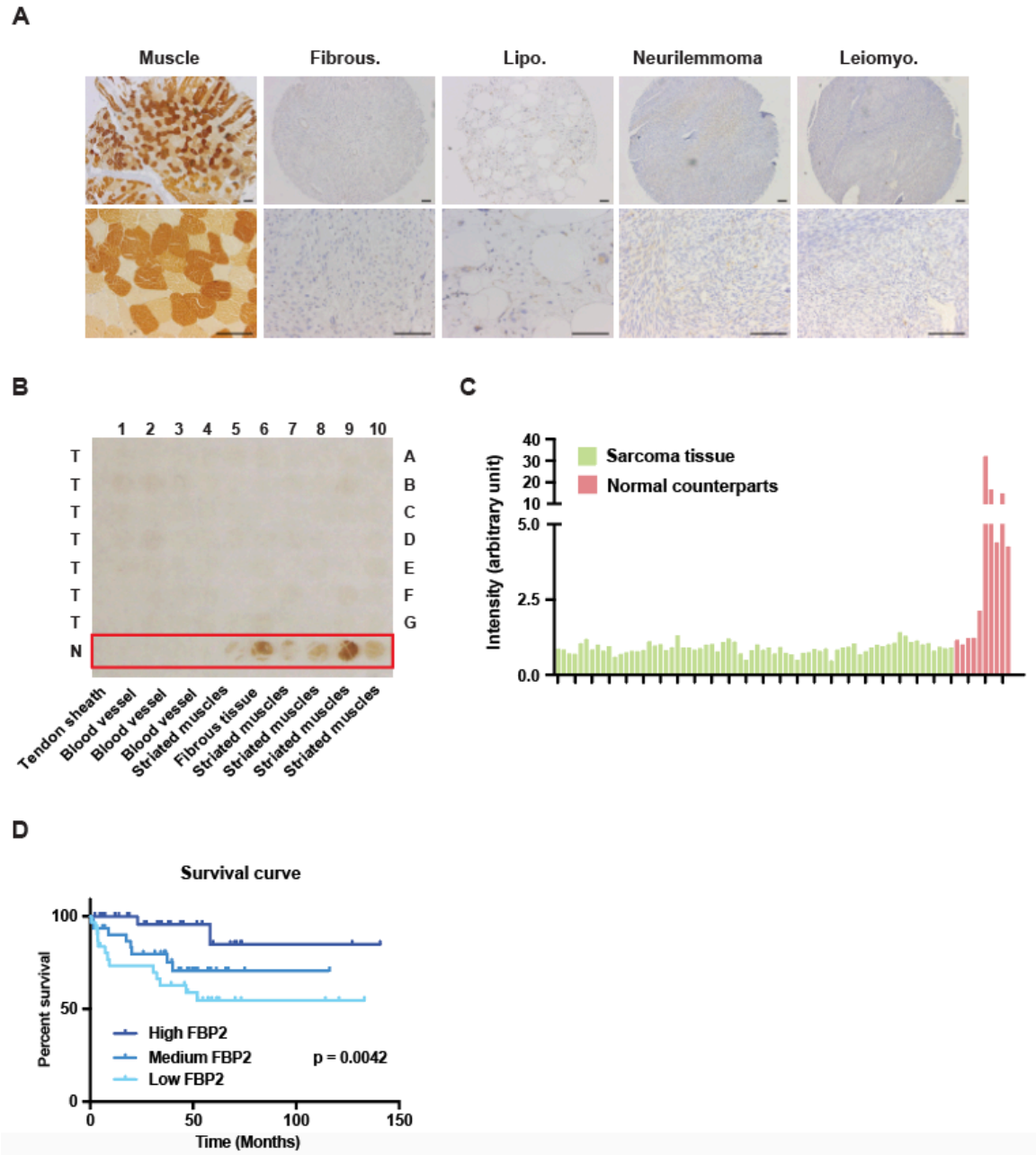

Figure 3. FBP2 protein abundance is uniformly decreased in sarcoma patient samples.

(A) Representative IHC FBP2 staining in human muscle and sarcoma samples from human sarcoma tissue array, including fibrous histiocytoma, liposarcoma, neurilemmoma, and leiomyosarcoma. Scale bars: 100 μm.

(B) Immunohistochemistry staining of a representative sarcoma microarray with FBP2 antibody. T, sarcoma tumor tissues; N, normal counterparts. Red box indicates normal counterparts. The sarcoma type of each sample is listed below.

(C) Quantification of IHC staining of 70 sarcomas and 10 normal tissues with FBP2 antibody from (B).

(D) Kaplan–Meier curve of overall survival of liposarcoma patients from the Gobble *et al*. data set (Gobble et al., 2011), segregated into the top 33% *FBP2* expression (High FBP2, n = 32), middle 33% *FBP2* expression (Medium FBP2, n = 32), and bottom *FBP2* expression (Low FBP2, n = 32). The p-value was calculated using a log-rank (Mantel–Cox) test.

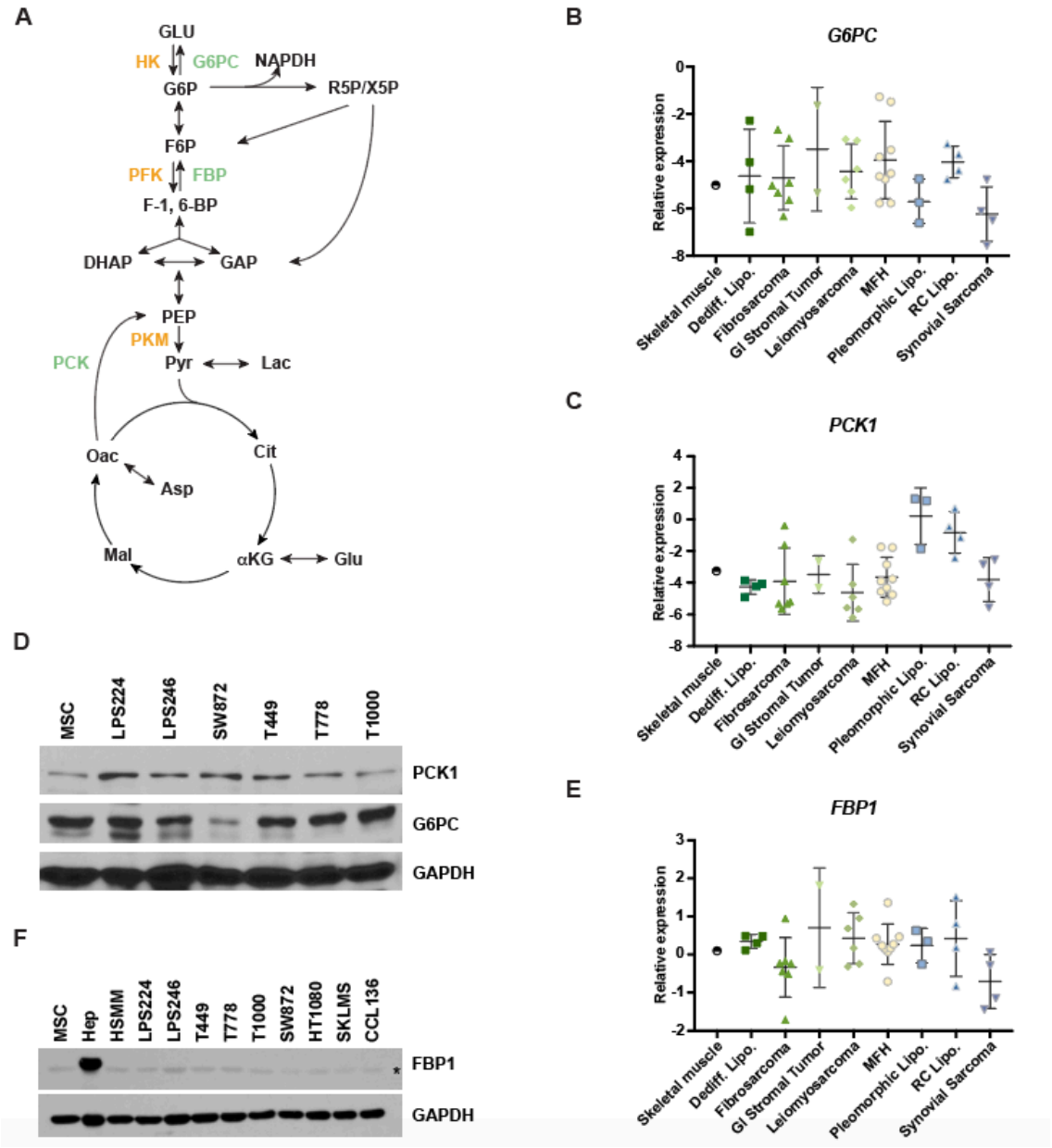

Figure 4. The expression of other gluconeogenic enzymes exhibit no consistent change in sarcoma.

(A) Illustration of central carbon metabolism, including glycolysis, gluconeogenesis, pentose phosphate pathway, and the TCA cycle. Enzymes controlling glycolysis (HK, hexokinase; PFK, phosphofructokinase; PKM, pyruvate kinase type M) are highlighted in orange, while enzymes controlling gluconeogenesis (G6PC, glucose-6-phosphatase catalytic subunit; FBP, fructose-1,6-

bisphosphatase; PCK, phosphoenolpyruvate carboxykinase) are highlighted in green. G6P, glucose-6-phosphate; F6P, fructose 6-phosphate; F-1,6-BP, fructose 1,6-bisphosphate; DHAP, dihydroxyacetone phosphate; GAP, glyceraldehyde 3-phosphate; R5P, ribose 5-phosphate; X5P, xylulose 5-phosphate; PEP, phosphoenolpyruvate; Pyr, pyruvate; Lac, lactate; Cit, citrate; αKG, α-ketoglutarate; Glu, glutamate; Mal, malate; Oac, oxaloacetate; Asp, aspartate.

(B and C) *G6PC* (B) and *PCK1* (C) mRNA expression based on Oncomine analysis of the Detwiller *et al.* sarcoma patient samples data set (Detwiller et al., 2005). Values are normalized to median-centered intensity and shown on a $\log_2$ scale. Dediff. lipo., dedifferentiated liposarcoma; MFH, Malignant Fibrous Histiocytoma; pleomorphic lipo., pleomorphic liposarcoma; RC lipo., round cell liposarcoma.

(D) Immunoblot analysis of PCK1 and G6PC protein levels in various human sarcoma cell lines. MSC, mesenchymal stem cells. MSCs served as normal control, while GAPDH served as a loading control.

(E) *FBP1* mRNA expression based on Oncomine analysis of the Detwiller *et al.* sarcoma patient samples data set (Detwiller et al., 2005).

(F) Immunoblot analysis of FBP1 protein levels in various human sarcoma cell lines. MSC, mesenchymal stem cell; hep, human primary hepatocyte. MSC served as normal control and Hep served as positive control for FBP1 expression. GAPDH served as a loading control. * indicates non-specific band.

FBP2 Re-Expression Suppresses Sarcoma Growth

To investigate its functional effects in different STS subtypes, we expressed FBP2 ectopically in human liposarcoma (LPS246, T1000, SW872), fibrosarcoma (HT1080), and mouse UPS (KP250) cell lines to levels observed in control HSMM or C2C12 cells, respectively (Figure 5A-B). FBP2 significantly inhibited cell proliferation under either low serum (1% serum, 25 mM glucose) or low glucose (10% serum, 5 mM glucose) conditions (Figures 6A-B), reminiscent of nutrient starved tumor microenvironments, as well as replete culture conditions (Figures 6C). In addition, FBP2 re-expression in SW872, HT1080 and KP250 cells dramatically impaired anchorage-independent growth in 3D soft agar colony assays (Figure 7).

We also exploited a doxycycline (dox)-inducible system to restore FBP2 expression in LPS246 cells (LPS246 TetO-FBP2) and identified dox concentrations that produced FBP2 protein in LPS246 TetO-FBP2 cells comparable to control HSMM cells (Figure 8A). To further evaluate the role of FBP2 in tumor growth and maintenance *in vivo*, NSG mice were injected subcutaneously with LPS246 TetO-FBP2 cells and tumors allowed to grow to 100 mm^3. Subsequent dox-induced FBP2 expression decreased tumor growth (volume and mass) without affecting mouse body weight (Figure 8B-E). FBP2 expression was maintained during dox treatment as shown by western blot (Figure 8F) and immunohistochemistry (IHC) (Figure 8G). The FBP2-expressing tumor cohorts exhibited decreased tumor cell proliferation as indicated by decreased phospho-histone H3 staining (Figure 8H). These results demonstrate that FBP2 restoration inhibits the *in vitro* proliferation and *in vivo* tumor growth of multiple STS cell types, including UPS, fibrosarcoma and liposarcoma.

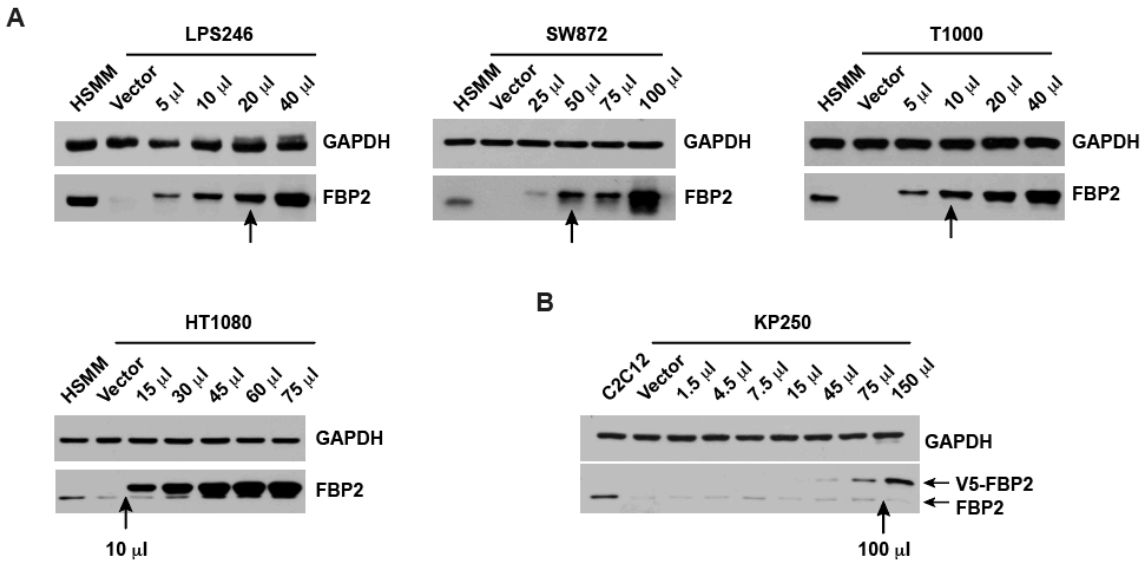

Figure 5. Re-expression of FBP2 in multiple sarcoma cell lines.

(A and B) Immunoblot showing FBP2 expression levels over lentiviral titration in LPS246, T1000, SW872 and HT1080 cells compared to HSMM (A), and in KP250 cells compared to C2C12 (B). GAPDH served as a loading control. Arrows indicate virus volumes used for all experiments.

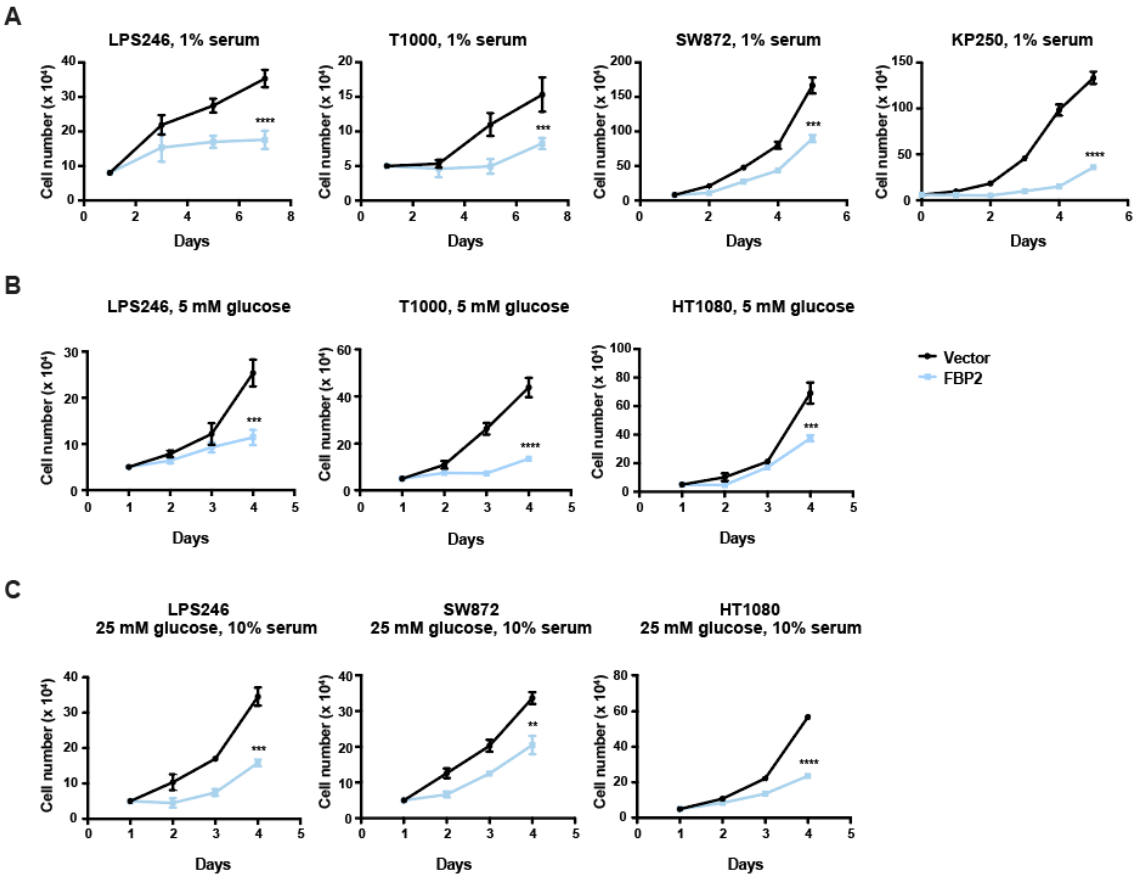

Figure 6. FBP2 re-expression inhibits sarcoma cell proliferation.

(A) Growth of LPS246, T1000, SW872, and KP250 cells in low serum medium (1% FBS), with or without ectopic FBP2 expression.

(B) Growth of LPS246, T1000, and HT1080 cells in low glucose medium (glucose free DMEM supplemented with 10% FBS and 5 mM glucose) with vector control of FBP2 expression.

(C) Growth of LPS246, SW872, and HT1080 cells in replete medium (10% FBS and 25 mM glucose) with vector control of FBP2 expression.

n = 3, *p < 0.05, **p < 0.01, ***p < 0.001, ****p < 0.0001.

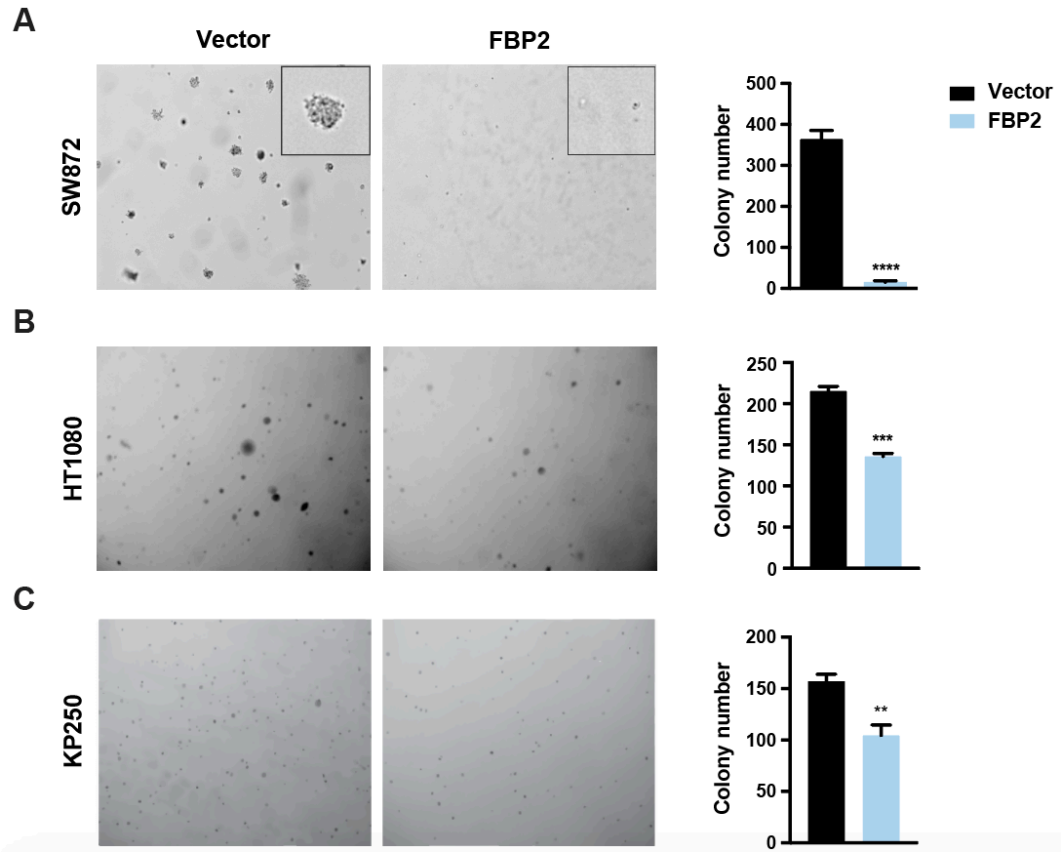

Figure 7. FBP2 re-expression inhibits anchorage independent growth.

(A-C) Soft agar colony formation assay of SW872 (A), HT1080 (B), and KP250 (C) cells with or without FBP2 expression. Representative pictures of colony size (left) and quantification of colony number (right).

Error bars represent SD of three replicate wells for each condition. *p < 0.05, **p < 0.01, ***p < 0.001, ****p < 0.0001.

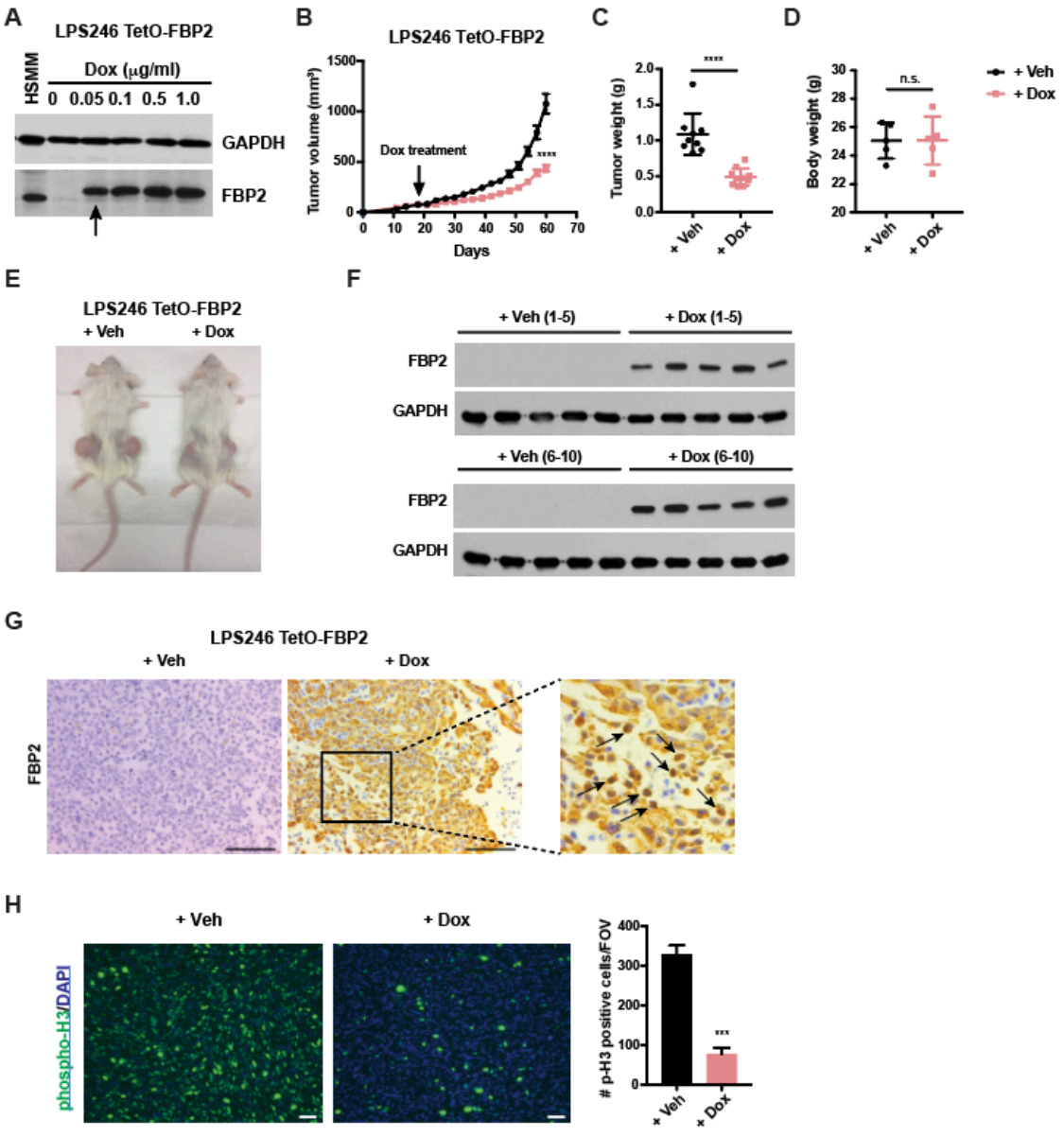

Figure 8. Dox-induced FBP2 expression suppresses sarcoma progression.

(A) Immunoblot showing FBP2 expression level with increased doxycycline concentration in LPS246 cells compared to HSMM. GAPDH served as loading control. The arrow indicates dox concentration used for all experiments.

(B) Tumor volume of LPS246 TetO-FBP2 liposarcoma xenografts with or without dox-induced FBP2 expression (each group includes ten tumors from five mice). ****p < 0.0001.

(C and D) LPS246 xenograft tumor weight (C) and body weight (D) with or without dox treatment at time of euthanasia, measured in grams. ****$p < 0.0001$, n.s., not significant.

(E) Representative xenograft tumors in mice fed with vehicle or dox chow.

(F) FBP2 induction in xenograft tumors were validated by western blot. GAPDH served as loading control.

(G) Representative immunohistochemistry image of FBP2 staining on LPS246 TetO-FBP2 tumor sections. Scale bars: 100 μm. Arrows indicate nuclear staining of FBP2.

(H) Representative image (left) of immunofluorescent staining of phosphor-Histone 3 and quantifications (right) in xenograft tumors with or without dox treatment. Five fields per slide were quantified. Scale bars: 100 μm. Error bars represent SD of three experimental replicates. *$p < 0.05$, **$p < 0.01$, ***$p < 0.001$, ****$p < 0.0001$. n.s., not significant.

FBP2 Re-Expression Inhibits Glycolysis

Glucose metabolism is balanced by catabolic glycolysis/oxidative phosphorylation (OXPHOS) and anabolic gluconeogenesis/glycogen production. Since FBP2 is a rate-limiting enzyme in gluconeogenesis, FBP2 re-expression is likely to antagonize glycolysis and therefore reduce glucose uptake. We ectopically expressed FBP2 in five STS cell lines and examined glucose metabolism. FBP2 significantly decreased glucose uptake and lactate secretion without affecting glutamine uptake in LPS224, LPS246, T1000, HT1080, and KP250 cells cultured in 10 mM glucose (Figure 9A-C). To further assess glycolytic pathway, we investigated the metabolic fate of [1,2-^{13}C]glucose, which produces glycolytic and TCA cycle intermediates containing two ^{13}C atoms, as well as intermediates containing one ^{13}C atom from the pentose phosphate pathway (PPP) (Figure 10A). Analysis of culture media confirmed reduced [1,2-^{13}C]glucose uptake and M1- and M2-labeled ^{13}C-lactate secretion in FBP2-expressing LPS246 cells (Figure 10B-C), indicating decreased conversion of glucose to lactate. [1,2-^{13}C]glucose releases its first carbon in the form of CO_2 to generate M1 species when catabolized through the oxidative portion of PPP (Lee et al., 1998); therefore, PPP flux can be determined by the ratio of M1- to M2-labeled lactate. Interestingly, we found that FBP2 re-expression reduced PPP flux (Figure 10D), which is important for the synthesis of ribonucleotides and NADPH. The same cell extracts were further analyzed by GC-MS to quantify M2 enrichment of glucose-derived TCA intermediates (citrate, α-ketoglutarate, fumarate, and malate), as well as TCA cycle products (aspartate and glutamate). We observed decreased M2 enrichment of four TCA intermediates (Figure 10E), as well as glutamate and aspartate (Figure 10F) in FBP2-expressing cells.

In addition, we employed an unbiased approach to determine relative abundance of intermediates from glycolysis, serine metabolism and the TCA cycle in KP250 and HT1080 cells. In both cell lines, ectopic FBP2 expression significantly reduced steady-state abundance of metabolites in glycolysis (glucose-6-phosphate, pyruvate, lactate) (Figure 11A), serine metabolism (serine and glycine) (Figure 11B) and the TCA cycle (citrate, α-ketoglutarate, fumarate, malate, oxaloacetate) (Figure 11C). In contrast to these decreased metabolic intermediates in FBP2-

expressing cells, we observed enrichment of metabolites in other pathways (Figure 11D), indicating a global metabolic adaptation in FBP2-expressing cells. Together, these results indicate that FBP2 inhibits glycolysis, which further affects serine and TCA cycle metabolism.

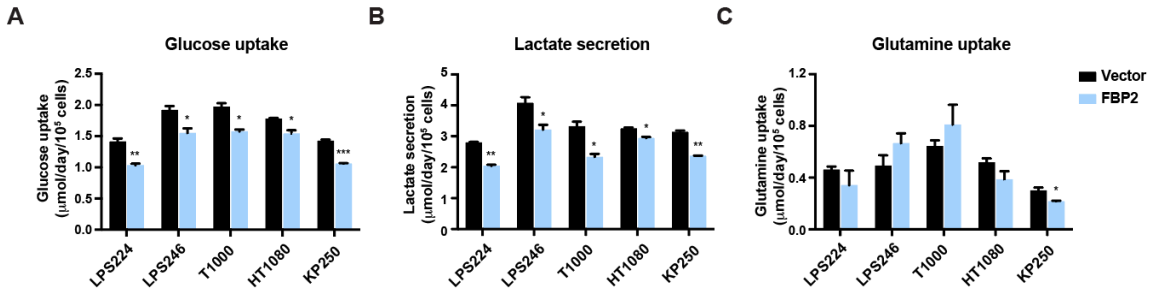

Figure 9. FBP2 restoration opposes glycolysis in multiple sarcoma cell lines.

(A-C) Glucose uptake (A), lactate secretion (B), and glutamine uptake (C) were assessed in LPS224, LPS246, T1000, HT1080, and KP250 cells with or without FBP2 re-expression by YSI bioanalyzer.

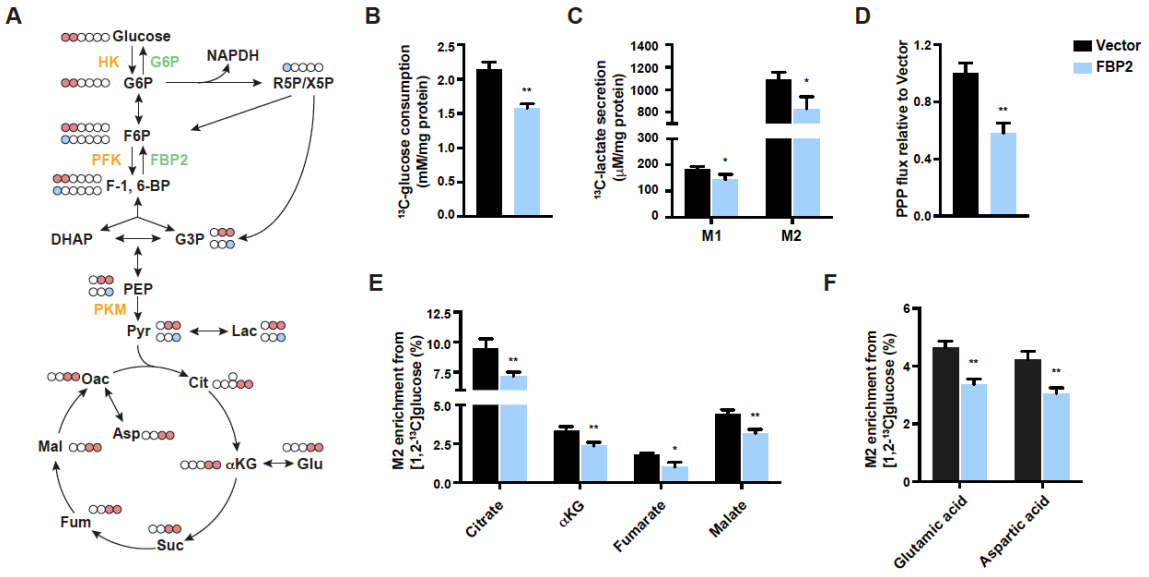

Figure 10. FBP2 re-expression inhibits glycolysis, the pentose phosphate pathway and glucose-derived TCA cycle.

(A) Carbon fate map showing the isotopomer distribution of indicated metabolites derived from [1,2-^{13}C]glucose. ^{13}C atoms are depicted as filled circles. ^{13}C atoms directly going through the glycolytic pathway are colored in red, while ^{13}C atoms going through the PPP and recycled back to glycolysis are colored in blue.

(B and C) [1,2-^{13}C]glucose consumption (B), M1 and M2 isotopomer distribution of lactate (C) measured from culture medium of LPS246 cells expressing vector control or FBP2.

(D) Calculated PPP flux (relative to vector control) in LPS246 cells with or without FBP2 expression based on the M1 to M2 ^{13}C-lactate ratio in cell extracts.

(E and F) M2 isotopomer distribution of indicated TCA metabolites (E) and amino acids (F) in LPS246 cells with or without FBP2 re-expression, labelled with [1,2-^{13}C]glucose. M2 enrichment represents the mole per cent excess of M2 species above natural abundance. αKG, α-ketoglutarate. Values represent mean ± SD of three experimental replicates. *p < 0.05, **p < 0.01, ***p < 0.001.

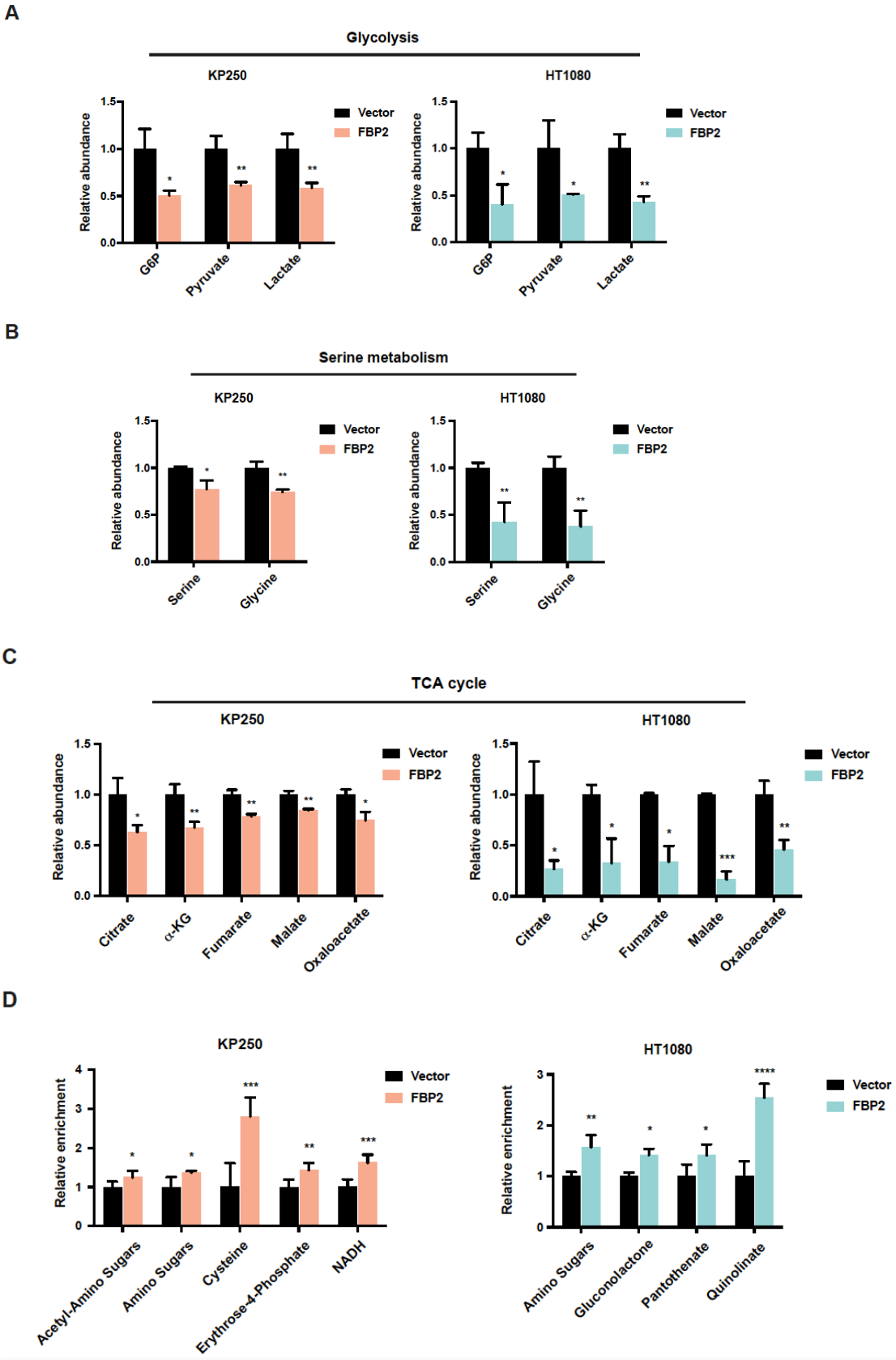
A
Glycolysis
KP250
HT1080
Relative abundance
Vector
FBP2
G6P
Pyruvate
Lactate
B
Serine metabolism
KP250
HT1080
Serine
Glycine
C
TCA cycle
KP250
HT1080
Citrate
α-KG
Fumarate
Malate
Oxaloacetate
D
KP250
HT1080
Relative enrichment
Acetyl-Amino Sugars
Amino Sugars
Cysteine
Erythrose-4-Phosphate
NADH
Amino Sugars
Gluconolactone
Pantothenate
Quinolinate

Figure 11. Ectopic FBP2 expression opposes glycolysis and the TCA cycle.

(A-C) Pan-metabolomic analysis of steady-state metabolites in KP250 cells (left) and HT1080 cells (right) expressing vector control or FBP2. Relative abundance of metabolites in glycolysis (A), serine metabolism (B) and TCA cycle (C) are shown.

(D) Representative examples of metabolites whose relative abundance is higher in KP250 cells (left) or HT1080 cells (right) upon FBP2 restoration, compared to cells expressing control vector.

Error bars represent SD of three experimental replicates. *p < 0.05, **p < 0.01, ***p < 0.001, ****p < 0.0001. n.s., not significant.

Nuclear FBP2 Inhibits Mitochondrial Gene Expression

To investigate whether the growth inhibitory effect of FBP2 is dependent on its enzymatic activity, we generated a catalytically inactive FBP2 mutant by replacing a glycine residue at position 260 with arginine ($FBP2^{G260R}$) as previously described (Åsberg et al., 2010) (Figure 12A). Upon wild-type FBP2 and $FBP2^{G260R}$ expression at comparable levels in LPS246 cells (Figure 12B), $FBP2^{G260R}$ inhibited cell growth, although to a lesser extent than wild-type FBP2 (Figure 12C), implying that FBP2 has catalytic activity-independent cellular functions.

Accumulating evidence demonstrates that multiple glycolytic enzymes exhibit nuclear localization and interact with transcription factors to regulate gene expression, in addition to their cytoplasmic roles (Huangyang and Simon, 2018). Interestingly, we observed strong nuclear staining of FBP2 within xenograft tumor sections (Figure 13A), suggesting that FBP2 possesses nuclear function. Specifically, immunofluorescence indicated overlap between endogenous FBP2 staining and DAPI staining in C2C12 cells (Figure 13B), and subcellular fractionation of HSMM and C2C12 cells further indicated that FBP2 co-purifies with both nuclear and cytosolic fractions (Figure 13C). A nuclear localization sequence (NLS) ($_{203}$KKKGK$_{207}$) was previously identified in FBP2(Gizak et al., 2009a; 2009b). By replacing four lysine residues in the NLS with alanine, we generated a nucleus-excluded form of FBP2 without disrupting its catalytic activity (Figure 13D), and $FBP2^{4KA}$ expression in LPS246 cells decreased cell proliferation albeit, not as dramatically as wild-type FBP2, suggesting that nuclear FBP2 contributes functionally to its growth inhibitory properties (Figure 13E-F). Interestingly, [1,2-^{13}C]glucose labeling in control or $FBP2^{4KA}$-expressing cells determined that $FBP2^{4KA}$ inhibits glucose uptake and lactate secretion (Figure 13G-H), but less potent than wild-type FBP2 (Figure 10B-C). These results indicate that nuclear FBP2 is also involved in suppressing glycolysis.

To gain further mechanistic insights into the function of nuclear FBP2, we compared the transcriptomes of vehicle (n = 5) or dox-treated (n = 4) LPS246 TetO-FBP2 cells by RNA-seq. Gene set enrichment analysis of FBP2-restored cells revealed reduced gene expression signatures for E2F targets, MYC targets, the G2M checkpoint, and OXPHOS (Figure 14A), as well as increased

expression signatures related to protein secretion, UV responses, and heme metabolism (Figure 14B). Ingenuity Pathway Analysis (IPA) also identified OXPHOS and mitochondrial dysfunction as the primary differentially modulated pathways in FBP2-expressing cells, compared to controls (Figure 14C). These functional categories contain genes encoding essential subunits of mitochondrial complex I, III, IV and V of the electron transport chain and genes critical for mitochondrial function (*UCP2* and *RHOT2*) (Figure 14D). We confirmed differential expression of several genes involved in OXPHOS (*MT-ND1*, *MT-MYB*, *MT-CO1* and *MT-ATP6*) by qRT-PCR analysis and found that FBP2, but not $FBP2^{4KA}$, significantly decreased their expression (Figure 15A). Intriguingly, catalytically inactive $FBP2^{G260R}$ downregulated mitochondrial gene expression to a similar level as wild-type FBP2 (Figure 15B). Taken together, these data suggest that nuclear FBP2 is required for inhibiting OXPHOS in an enzymatic activity-independent manner.

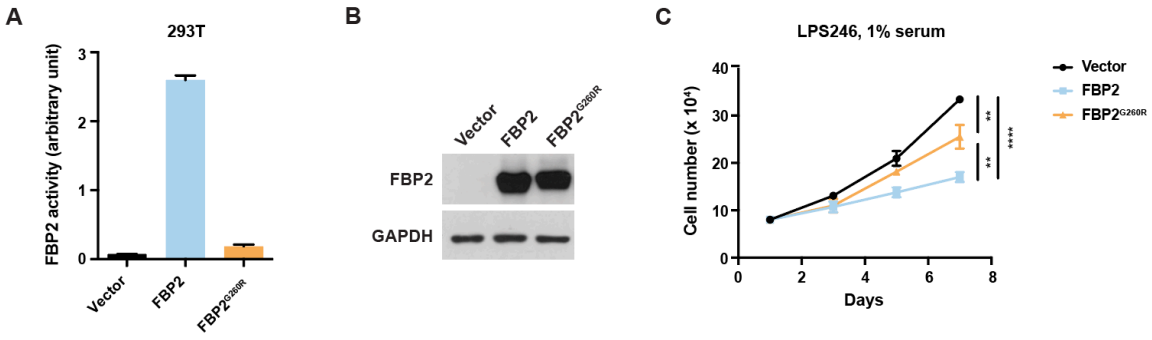

Figure 12. Catalytically inactive FBP2^{G260R} suppresses sarcoma cell growth.

(A) Enzymatic activity in 293T cells expressing vector, wild-type FBP2 and FBP2^{G260R}.

(B) Protein levels of ectopically expressed FBP2 and FBP2^{G260R} in LPS246 cells. GAPDH was used as a loading control.

(C) Growth of vector control, FBP2- or FBP2^{G260R}-expressing LPS246 cells grown in 1% serum medium.

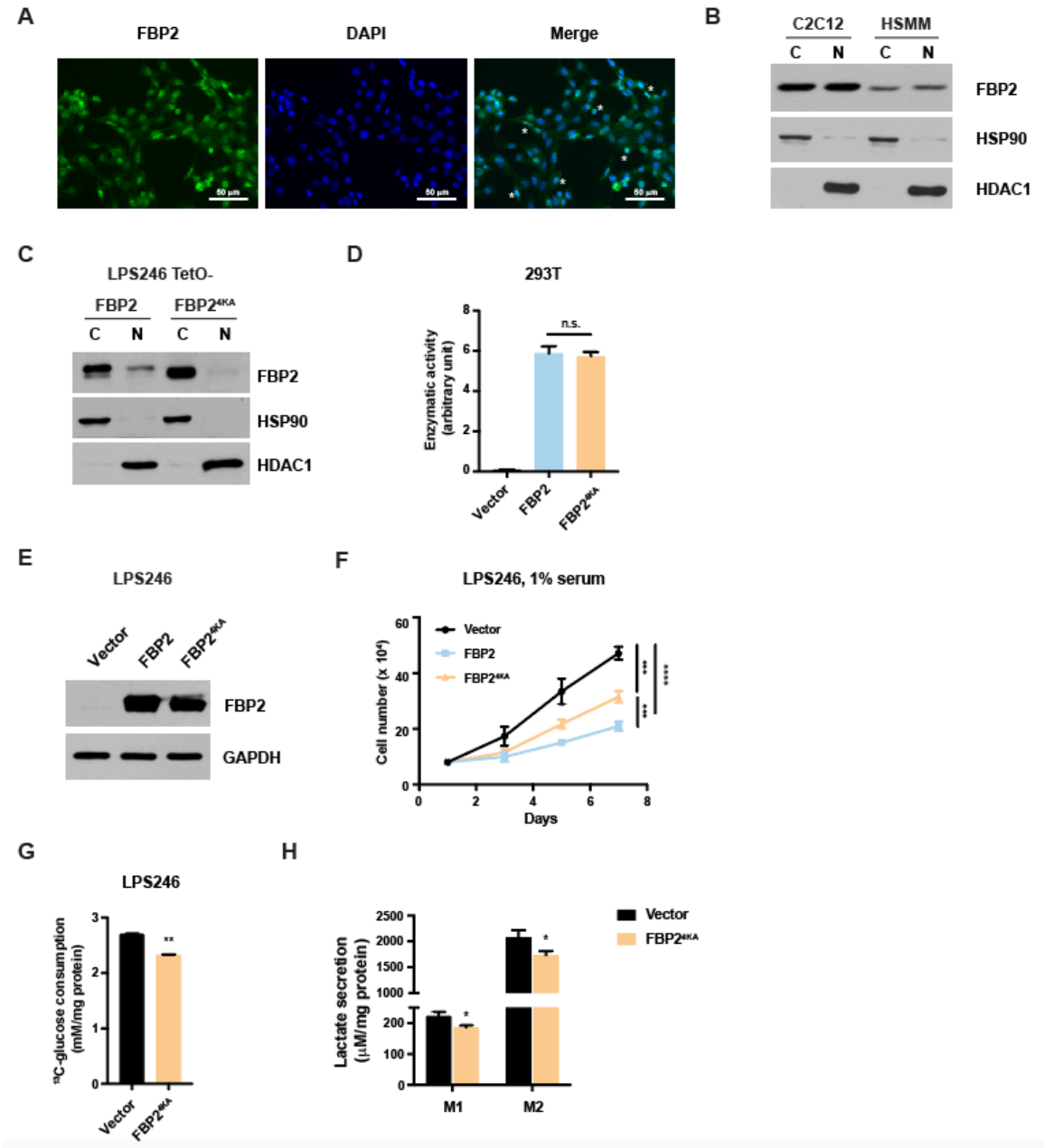

Figure 13. Nuclear FBP2 is able to inhibit sarcoma cell proliferation and glycolysis.

(A) Immunofluorescent staining of mouse myoblast C2C12 cells with FBP2 antibody. Asterisks indicate representative sites with nuclear FBP2. DAPI is a fluorescent nuclear dye.

(B) FBP2 protein levels detected in cytosolic and nuclear fractions of C2C12 and HSMM. HSP90, a cytosolic protein, and HDAC1, a nuclear protein, reflect the purity of respective subcellular fractionations.

(C) Western blot analysis of V5-tagged FBP2 or FBP2^{4KA} (4 lysines in nuclear localization sequence were substituted with alanine) in the cytosolic and nuclear fractions of transfected LPS246 cells.

(D) Enzymatic activity in 293T cells expressing control vector, wild-type FBP2 and FBP2^{4KA}.

(E) Protein levels of ectopically expressed FBP2 and FBP2^{4KA} mutant in LPS246 cells. GAPDH serves as a loading control.

(F) Growth of vector control, FBP2- or FBP2^{4KA}-expressing LPS246 cells in 1% serum medium.

(G and H) [1,2-^{13}C]glucose consumption (G), M1 and M2 isotopomer distribution of lactate (H) measured from culture medium of LPS246 cells expressing vector control or FBP2.

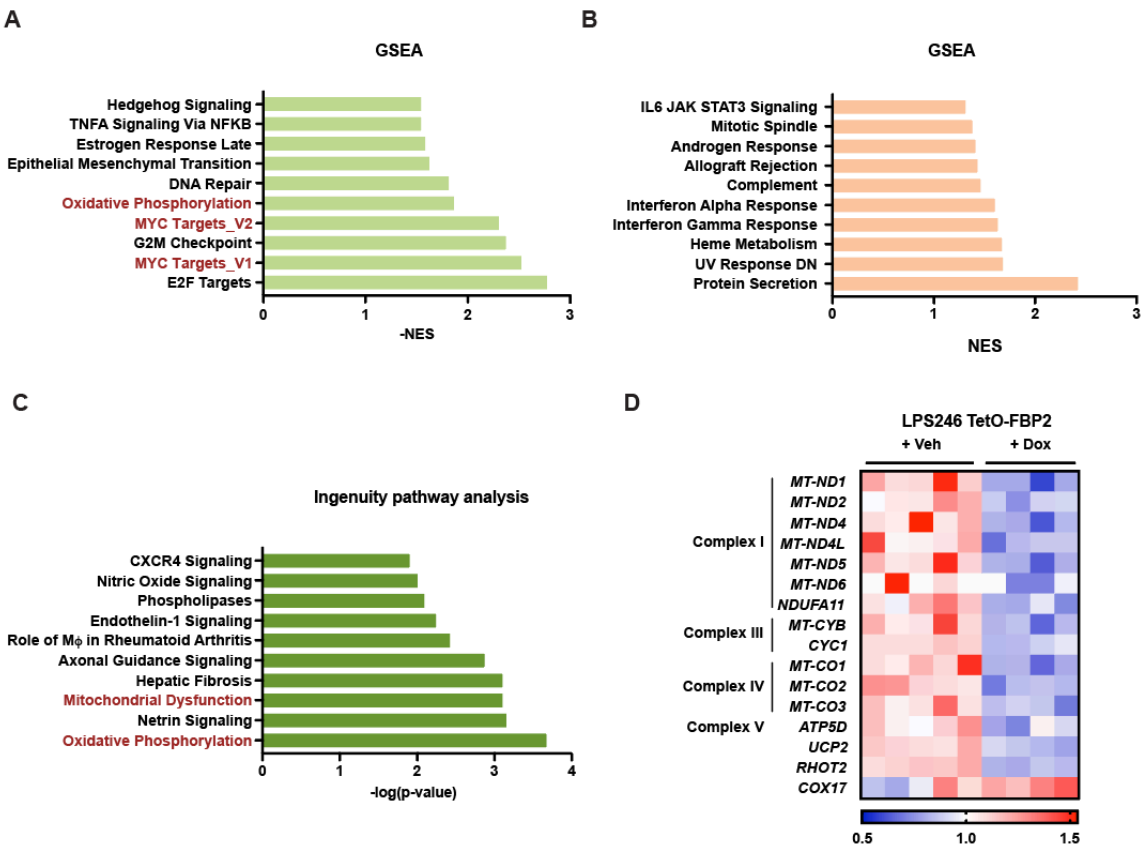

Figure 14. RNA-seq analyses of transcriptome between vehicle or dox treated LPS246 TetO-FBP2 cells.

(A and B) GSEA comparing vehicle-treated (n = 5) and dox-treated (n = 4) LPS246 TetO-FBP2 cells. The 50-gene "Hallmark signatures" set from MsigDB was queried. Top 10 gene sets downregulated (A) or upregulated (B) in dox-treated groups are shown with the normalized enrichment score (NES). Relevant gene sets are highlighted with red.

(C) Differentially expressed genes were analyzed using ingenuity pathway analysis (IPA) software. Top 10 relevant and significant biological pathways were identified according to p-value from Fisher's exact test.

(D) Heatmap showing the relative expression of OXPHOS genes and mitochondrial dysfunction pathway from IPA. Expression signals are depicted using pseudocoloring, in which expression for each gene is shown as high (red) or low (blue).

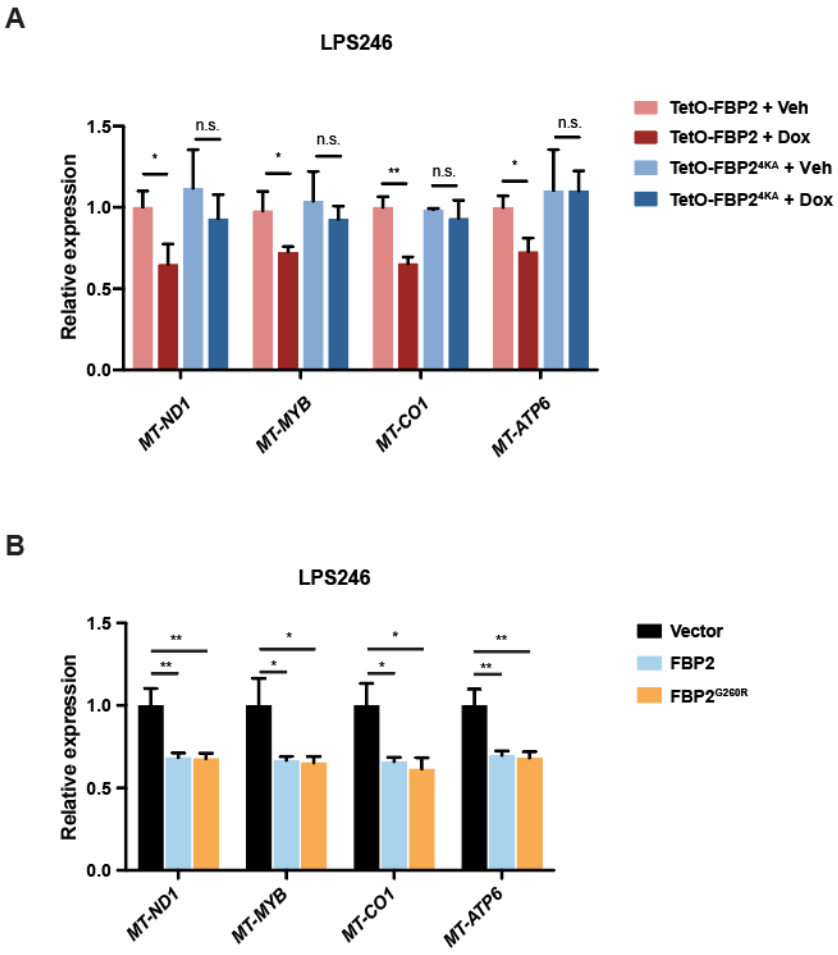

Figure 15. Nuclear FBP2 inhibits mitochondrial gene expression in a catalytic activity-independent manner.

(A) qRT-PCR analysis of *MT-ND1*, *MT-CYB*, *MT-CO1*, and *MT-ATP6* in LPS246 cells constitutively expressing TetO-FBP2 or Tet-FBP2^{4KA}, treated with vehicle or dox.

(B) qRT-PCR analysis of *MT-ND1*, *MT-CYB*, *MT-CO1*, and *MT-ATP6* in LPS246 cells constitutively expressing vector, FBP2 or FBP2^{G260R}.

Error bars represent SD of three experimental replicates. *p < 0.05, **p < 0.01, ***p < 0.001, ****p < 0.0001. n.s., not significant.

Nuclear FBP2 Impairs Mitochondrial Biogenesis

To determine whether reduced transcription of OXPHOS genes in FBP2-expressing cells correlated with decreased mitochondrial biogenesis, we first measured mitochondrial DNA content by using real-time quantitative PCR. Mitochondrial to nuclear DNA ratios were dramatically decreased in FBP2-expressing LPS246 cells (Figure 16A), and flow cytometric analysis of cells stained with MitoTracker further revealed that FBP2 induction reduced mitochondrial mass (Figure 16B). Similarly, we observed a dramatic decrease in citrate synthase activity after restoring expression of FBP2 in LPS246 cells (Figure 16C). Decreased mitochondrial biogenesis in FBP2-expressing LPS246 cells was further confirmed by transmission electron microscopy, indicated by reduced number of mitochondria and swollen mitochondria with disorganized cristae (Figure 16D). Consistently, LPS246 xenograft sections exhibited reduced staining of Vdac (voltage-dependent anion channel) and Tomm20 (a constitutively expressed mitochondrial protein) in dox-treated tumors, supporting decreased mitochondrial mass caused by FBP2 expression (Figure 16E). As doxycyline has been reported to interfere with mammalian protein synthesis and disrupt mitochondrial proteostasis and function (Moullan et al., 2015), we confirmed that mtDNA content, MitoTracker staining, and citrate synthase activity were comparable in both vehicle and dox-treated LPS246 TetO-FBP2^{4KA} cells (Figure 16A-C). Collectively, these data demonstrate that nuclear FBP2 inhibits mitochondrial biogenesis in LPS246 cells.

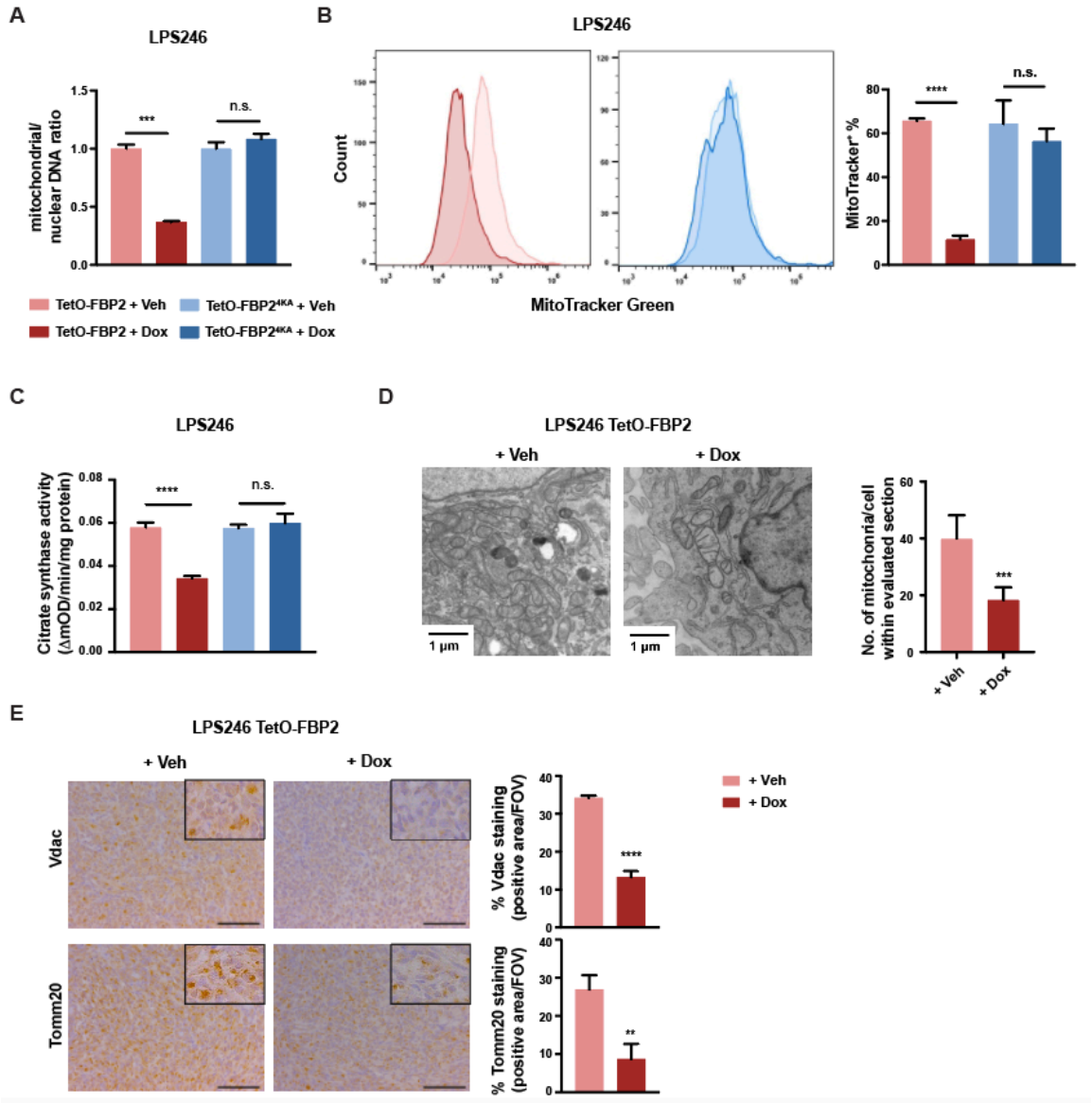

Figure 16. Nuclear FBP2 impairs mitochondrial biogenesis.

(A) qPCR analysis of mitochondrial (*MT-ND1*) versus nuclear (*β-globin*) DNA content in indicated cells (three experimental replicates).

(B) LPS246 TetO-FBP2 cells and TetO-FBP2^{4KA} cells stained with MitoTracker Green FM probe. Flow cytometry plots (left) show the fluorescence intensity corresponding to mitochondrial mass. Histograms (right) show the quantification (three experimental replicates).

(C) Citrate synthase activity measured in indicated cells (three experimental replicates).

(D) Ultrastructural analysis of mitochondria in LPS246 Teto-FBP2 cells using transmission electron microscopy. Scale bars: 1 μm. Quantification of the number of mitochondria per cell in the imaged section (vehicle treated, n = 10 cells; dox treated, n = 10 cells).

(E) Immunohistochemical staining for expression of voltage-dependent anion channel (Vdac) and Tomm20 on sections from LPS246 TetO-FBP2 xenografts treated with vehicle or dox. Five fields per slide were quantified. Scale bars: 100 μm.

Data are represented as mean ± SD. *p < 0.05, **p < 0.01, ***p < 0.001, ****p < 0.0001. n.s., not significant.

FBP2 Suppresses Mitochondrial Respiration and the TCA Cycle

The effects of FBP2 expression on mitochondrial OXPHOS activity were investigated by culturing LPS246 cells in glucose-free medium containing 5 mM galactose, which cannot be fermented, requiring cells to rely on mitochondrial metabolism to generate sufficient ATP for survival (Rossignol et al., 2004). We observed increased apoptosis in dox-treated LPS246 TetO-FBP2 cells cultured in galactose medium (Figure 17A-B) compared to vehicle-treated cells, indicating that mitochondrial OXPHOS is critically impaired upon FBP2 induction. Furthermore, oxygen consumption rates (OCR) and ATP production were lower in FBP2-expressing LPS246 cells compared to controls (Figure 17C-D, I). In contrast, $FBP2^{4KA}$ expression had no effect on OCR in LPS246 cells (Figure 17E-F). Loss of ATP-generating capacity stimulated glycolytic compensation in both LPS246 TetO-FBP2 and TetO-$FBP2^{4KA}$ cells, as indicated by extracellular acidification rate (ECAR) (Figure 17G-H). Interestingly, ECAR was lower in both FBP2- and $FBP2^{4KA}$-expressing LPS246 cells than control cells (Figure 17G-H), indicating inhibition of glycolysis by each protein. These results are consistent with our previous conclusion that FBP2 suppresses glucose uptake and lactate secretion (Figure 9-11). In active mitochondria, a small percentage of electrons are prematurely leaked to O_2 from complex I and/or complex III, resulting in the formation of reactive oxygen species (ROS) (Chatterjee et al., 2011). As expected, reduced OCRs observed in FBP2-expressing LPS246 cells correlated with a substantial decrease in ROS levels; whereas $FBP2^{4KA}$ had no effect on ROS accumulation (Figure 17J).

To assess the effects of FBP2 expression on TCA cycle metabolite levels, we performed isotope tracing experiments by labeling vehicle- or dox-treated LPS246 TetO-FBP2 cells with [3-^{13}C]pyruvate. Labeled pyruvate is converted to acetyl-CoA by mitochondrial pyruvate dehydrogenase, which then combines with oxaloacetate to produce M1-labeled citrate. When acetyl-CoA is abundant, pyruvate decarboxylase can also generate M1-labeled oxaloacetate, which then incorporates M1-labeled acetyl-CoA to produce M2-labeled citrate (Figure 18A). We observed decreased M1 and M2 enrichment of three TCA intermediates (citrate, fumarate and malate), as well as glutamic acid and aspartic acid (Figure 18B-E) in FBP2-expressing cells. In

contrast, ectopic FBP2^{4KA} expression had no effect on M1 and M2 enrichment of TCA intermediates and products compared with control cells (Figure 18F-I), further indicating that it is nuclear FBP2 that restrains mitochondrial function and metabolism.

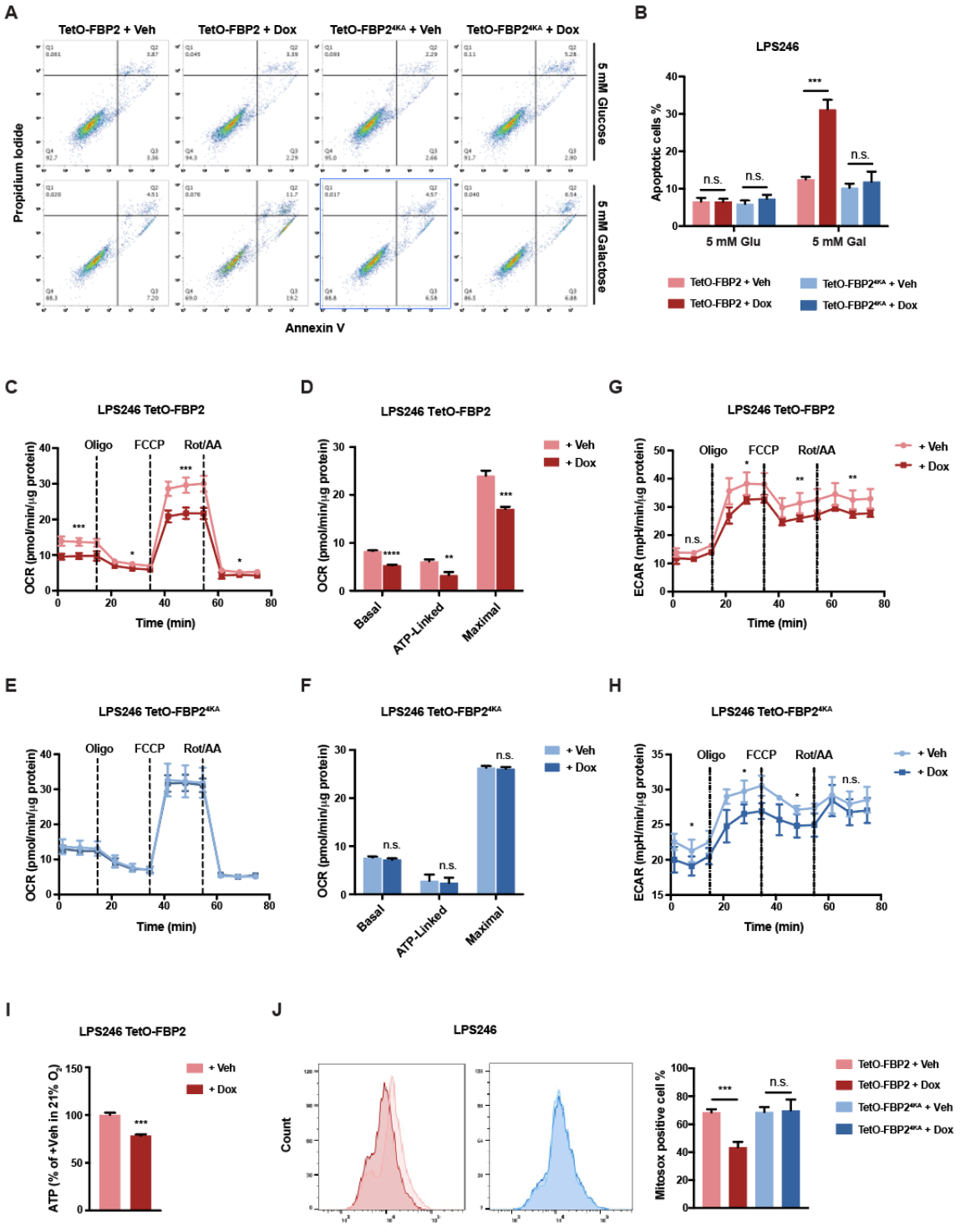

Figure 17. FBP2 suppresses mitochondrial respiration.

(A) LPS246 cells cultured in 5 mM glucose and 5 mM galactose medium. Apoptotic cells measured through Annexin V/PI staining followed by flow cytometry.

(B) Indicated cells were cultured in 5 mM glucose and 5 mM galactose medium. Flow cytometry plots of annexin V/PI staining of indicated cells.

(C-F) Relative oxygen consumption rate normalized to protein abundance in LPS246 TetO-FBP2 cells (C) or LPS246 TetO-FBP2^{4KA} cells (E) treated with vehicle or dox. Histogram showing basal, ATP-linked and maximal respiration in LPS246 TetO-FBP2 cells (D) or LPS246 TetO-FBP2^{4KA} cells (F) treated with vehicle or dox. Data are presented as mean ± SD of three reading cycles of n = 9 wells pooled from three independent experiments.

(G and H) Relative extracellular acidification rate (ECAR) normalized to protein abundance in LPS246 TetO-FBP2 cells (G) or LPS246 TetO-FBP2^{4KA} cells (H) treated with vehicle or dox. Data are presented as mean ± SD of three reading cycles of n = 9 wells pooled from three independent experiments.

(I) ATP production was measured in indicated cells.

(J) Fluorescence intensity of MitoSox analyzed by flow cytometry. Flow cytometry plots (left) show the fluorescence intensity. Histograms (right) display their quantification (three experimental replicates). *$p < 0.05$, **$p < 0.01$, ***$p < 0.001$, ****$p < 0.0001$. n.s., not significant.

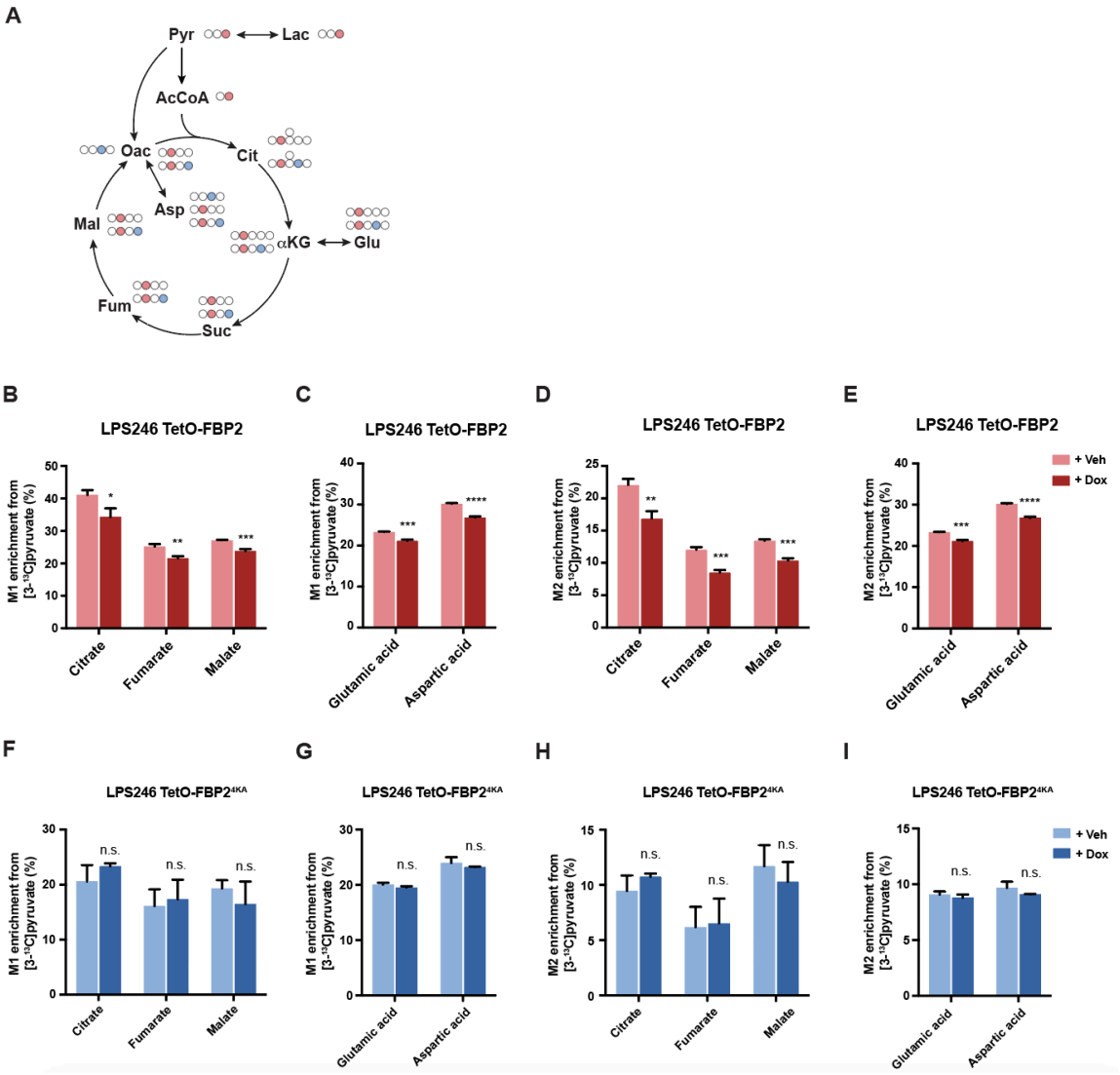

Figure 18. Nuclear FBP2 inhibits the TCA cycle in LPS246 cells.

(A) Carbon fate map showing the isotopomer distribution of indicated metabolites derived from [3-^{13}C]pyruvate. ^{13}C atoms are depicted as filled circles. ^{13}C atoms directly going through the acetyl-CoA are colored in red, while ^{13}C atoms going through oxaloacetate and combined with acety-CoA to generate citrate are colored in blue.

(B-E) M1 isotopomer distribution of indicated TCA metabolites (A) and amino acids (B), and M2 isotopomer distribution of indicated TCA metabolites (C) and amino acids (D) in LPS246 TetO-FBP2 cells with vehicle or dox treatment, labelled with [3-^{13}C]pyruvate.

(F-I) M1 isotopomer distribution of indicated TCA metabolites (F) and amino acids (G), and M2 isotopomer distribution of indicated TCA metabolites (H) and amino acids (I) in LPS246 TetO-FBP2^{4KA} cells with vehicle or dox treatment, labelled with [3-^{13}C]pyruvate.

Error bars represent SD of three experimental replicates except in B and C. *p < 0.05, **p < 0.01, ***p < 0.001, ****p < 0.0001. n.s., not significant.

FBP2 Transcriptionally Represses Mitochondrial Biogenesis

Mitochondrial biogenesis and function are controlled by a set of nuclearly-encoded transcription factors, including PPAR-γ coactivators (PGC-1α), nuclear respiratory factor 1 (NRF1), and mitochondrial transcription factor A (TFAM) (Scarpulla, 2012). As nuclear FBP2 regulates mitochondrial function, we hypothesized that FBP2 dampens mitochondrial biogenesis through inhibiting one or more of these nuclear regulators. Quantitative RT-PCR analyses revealed significant downregulation of *NRF1* and *TFAM* expression upon FBP2 restoration (Figure 19A). Ectopic expression of TFAM or NRF1 reversed the suppression of target genes associated with OXPHOS (*MT-ND1*, *MT-CYB*, *MT-CO1* and *MT-ATP*) (Figure 19B-C, Figure 20A-B), and partially restored mitochondrial mass (Figure 19D, Figure 20C). Moreover, ectopic TFAM or NRF1 expression partially reversed cell apoptosis (Figure 19E, Figure 20D) and proliferation (Figure 19F, Figure 20E) in dox-treated LPS246 TetO-FBP2 cells.

To elucidate the molecular mechanisms whereby FBP2 alters the expression of nuclear transcription factors associated with mitochondrial biogenesis, we examined the top differentially expressed pathways based on RNA-seq data and identified Myc target genes as one of the top downregulated gene sets (Figure 14A). Previous studies have demonstrated that c-Myc regulates mitochondrial biogenesis and gene expression (Lee et al., 2017; Scarpulla, 2008); for example, c-Myc induces NRF1 target genes by binding to a canonical NRF1 binding site, leading to the sensitization of cells to apoptosis (Morrish et al., 2003). In addition, c-Myc potentiates mitochondrial biogenesis through induction of TFAM and other nuclear-encoded mitochondrial genes (Li et al., 2005). To ascertain that FBP2 diminishes c-Myc transcriptional activity, we measured c-Myc luciferase-reporter intensity and found FBP2 decreased c-Myc functionality (Figure 21A). Transcript levels of c-Myc target genes (*CCND2, eIF2A, NPM1, PSAT1*) were also decreased in FBP2-expressing cells (Figure 21B). To determine whether FBP2 represses mitochondrial biogenesis in a predominantly c-Myc dependent manner, we assessed the expression of mitochondrial genes (*MT-ND1*, *MT-CO1* and *MT-ATP6*) in the presence and absence of c-Myc using RNA interference. Interestingly, dox-induced FBP2 expression or *sic-Myc* resulted in comparable repression of

mitochondrial gene transcription (Figure 21C-D), and combined FBP2 expression and *sic-Myc* showed no additive effects on gene expression. MitoTracker staining indicated a slight but perceptible decrease in mitochondrial mass in cells with combined dox and *sic-Myc* treatment, relative to cells with either treatment alone (Figure 21E). We conclude that FBP2's inhibition of mitochondrial biogenesis is largely, but not entirely dependent on the c-Myc pathway.

c-Myc has been reported to bind *TFAM* in the region of amplicons 1 and 2, approximately 900 bp upstream of the transcription start site (Figure 22A), thereby stimulating *TFAM* expression (Li et al., 2005). Remarkably, chromatin immunoprecipitation (ChIP) analyses indicated that FBP2 protein was enriched at amplicon 1, which contains a 5'-CACGTG-3' c-Myc binding site, but not at amplicon 2, which contains a Myc/Max 5'-GCG-3' half site (Figure 22B). As expected, nucleus-excluded FBP2^{4KA} was not detected at either amplicon (Figure 22B). Importantly, ChIP-reChIP analyses revealed co-localization of c-Myc and FBP2 proteins at *TFAM* promoter amplicon 1 (Figure 22C). We also demonstrated the association of epitope-tagged FBP2 or FBP2^{4KA} and endogenous c-Myc by co-immunoprecipitations in LPS246 cell lysates (Figure 22D), suggesting their physical interaction can occur in both the nucleus and cytosol (albeit at lower levels). Finally, GST pull-down assays of bacterially expressed proteins further revealed that FBP2 directly binds to c-Myc (Figure 22E). Collectively, these results indicate that FBP2 inhibits c-Myc transcriptional activation of *TFAM*, by direct physical association at its promoter.

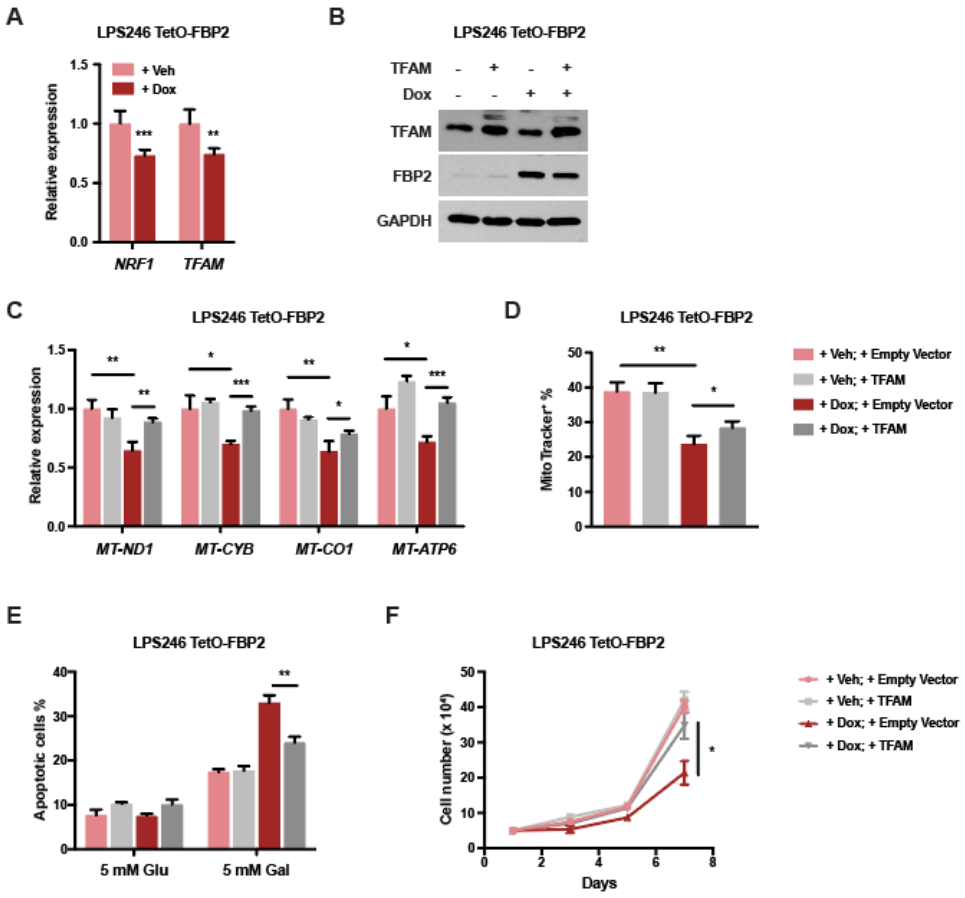

Figure 19. Ectopic expression of TFAM partially rescued mitochondrial biogenesis.

(A) qRT–PCR analysis of NRF1 and TFAM in vehicle treated or dox-treated LPS246 TetO-FBP2 cells.

(B) Immunoblot analysis for ectopic expression of vector control or TFAM in LPS246 TetO-FBP2 cells.

(C) qRT-PCR analysis of *MT-ND1*, *MT-CYB*, *MT-CO1*, and *MT-ATP6* in indicated cells.

(D) LPS246 TetO-FBP2 cells with or without TFAM expression stained with MitoTracker Green FM probe. Fluorescence intensity corresponding to mitochondrial mass is shown in histograms.

(E) Indicated cells cultured in 5 mM glucose and 5 mM galactose medium, where apoptotic cells were measured through Annexin V/PI staining followed by flow cytometry.

(F) Growth of indicated cells in low serum medium (1% FBS).

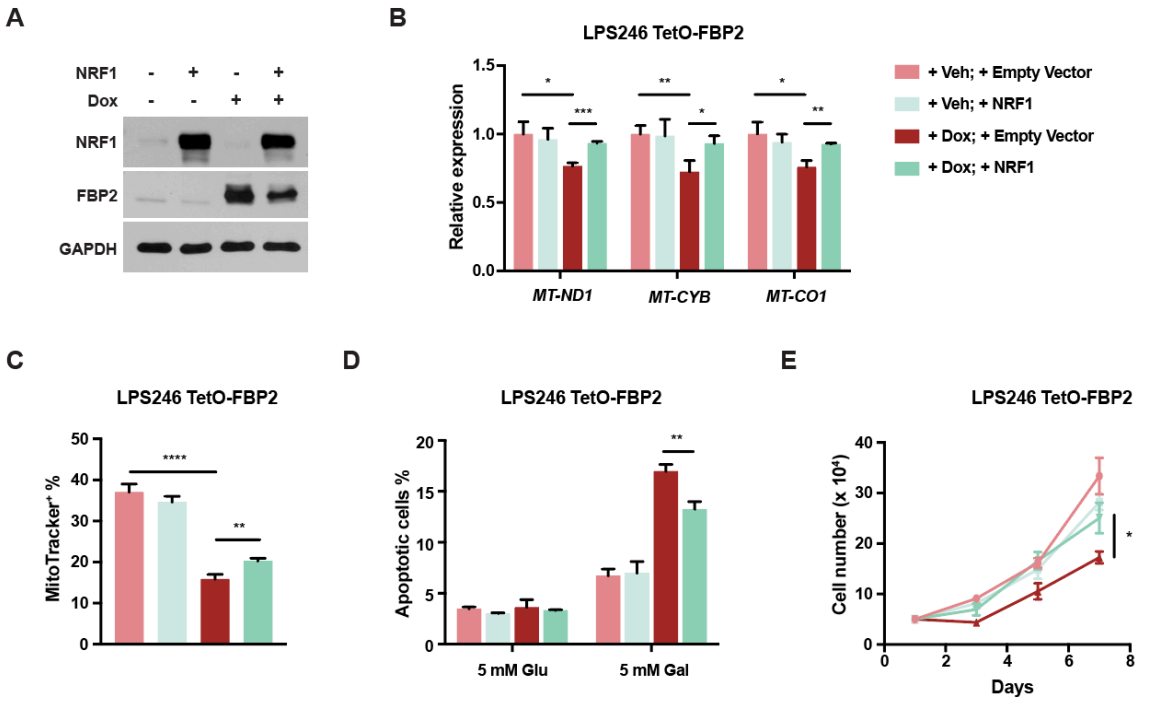

Figure 20. NRF1 partially rescues FBP2-mediated inhibition of mitochondrial biogenesis.

(A) Immunoblot analysis for ectopic expression of vector control or NRF1 in LPS246 TetO-FBP2 cells.

(B) qRT-PCR analysis of *MT-ND1*, *MT-CYB*, and *MT-CO1* in indicated cells.

(C) LPS246 TetO-FBP2 cells with or without NRF1 expression were stained with MitoTracker Green FM probe. Fluorescence intensity corresponding to mitochondrial mass is shown in histogram.

(D) Indicated cells were cultured in 5 mM glucose and 5 mM galactose medium. Apoptotic cells were measured through Annexin V/PI staining followed by flow cytometry.

(E) Growth of indicated cells in low serum medium (1% FBS).

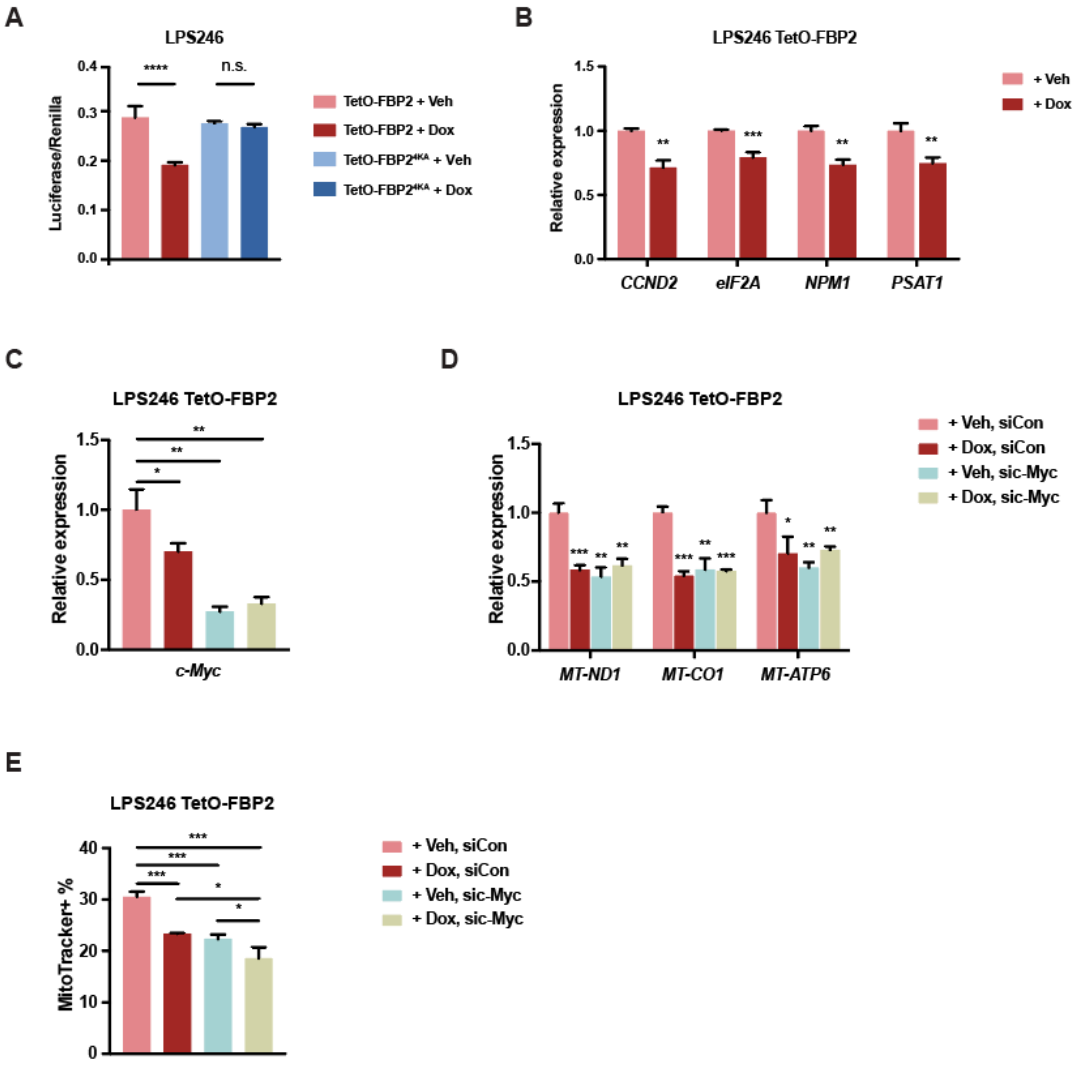

Figure 21. FBP2 inhibits mitochondrial biogenesis in a c-Myc dependent manner.

(A) c-Myc reporter activity measured in LPS246 TetO-FBP2/FBP2^{4KA} cells transfected with Myc/Max luciferase reporter, in the presence of vehicle or dox. Transfection efficiencies were normalized to co-transfected pRenilla-luciferase.

(B) qRT-PCR analysis of c-Myc target genes (*CCND2*, *eIF2A*, *NPM1*, *PSAT1*) in indicated cells.

(C and D) qRT-PCR analysis of *c-Myc* (C) and *MT-ND1*, *MT-CO1* and *MT-ATP6* (D) in LPS246 TetO-FBP2 cells under four conditions (+ Veh, siControl; + Dox, siControl; + Veh, sic-Myc; + Dox, sic-Myc).

(E) LPS246 TetO-FBP2 cells treated with four conditions stained with MitoTracker Green FM probe. Histogram shows the quantification of fluorescence intensity corresponding to mitochondrial mass. Data are represented as mean ± SD (three experimental replicates) *p < 0.05, **p < 0.01, ***p < 0.001, ****p < 0.0001. n.s., not significant.

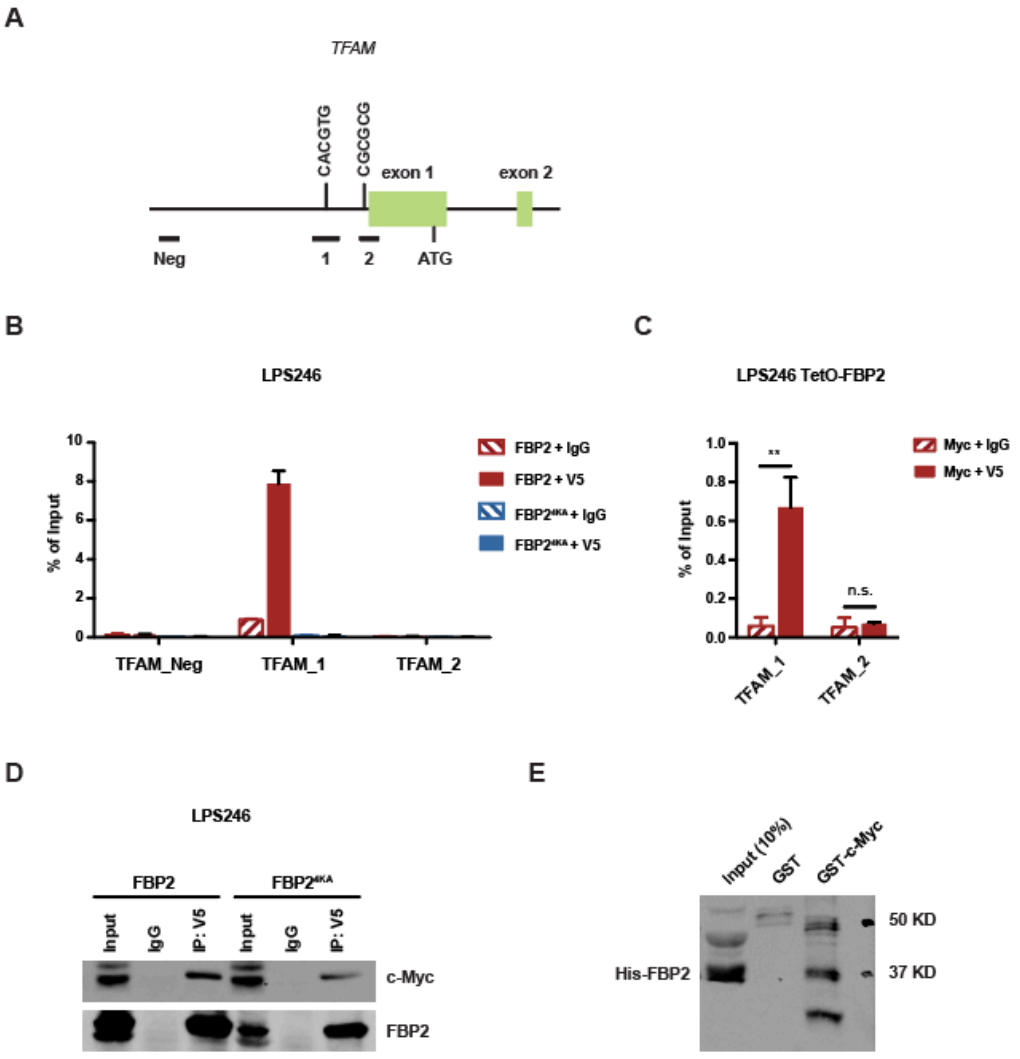

Figure 22. FBP2 suppresses *TFAM* expression by co-localizing with c-Myc at the promoter region of *TFAM*.

(A) Diagram of 2 kb upstream of exon 1 to exon 2 of human *TFAM*. Exons are represented by green boxes. The E box in amplicon 1 is illustrated. Horizontal bars labeled Neg, 1, 2 indicate the regions amplified for ChIP analysis.

(B) ChIP assays evaluating FBP2 association with chromatin at a c-Myc binding site in *TFAM* promoter (amplicon 1 and 2), or to a site negative for c-Myc binding (amplicon Neg). IgG, isotype-matched immunoglobulin G; V5, V5-tagged FBP2.

(C) ChIP-reChIP analysis examining the co-localization of c-Myc and FBP2 at amplicon 1 and 2 at *TFAM* promoters.

(D) V5 tagged FBP2 or FBP2^{4KA}-expressing LPS246 cell lysates were immunoprecipitated with IgG, or V5 antibody and blotted for endogenous c-Myc. IP, immunoprecipitate.

(E) GST pull-down analysis between recombinant His-FBP2 and recombinant GST or GST-tagged c-Myc and blotted using FBP2 antibody.

Data are represented as standard error of the mean (three technical replicates from a representative experiment). *$p < 0.05$, **$p < 0.01$, ***$p < 0.001$, ****$p < 0.0001$. n.s., not significant.

Discussion

Soft-tissue sarcomas (STS) are a complex set of mesenchymal malignancies, compromising more than 70 subtypes (Fletcher, 2014). Despite rapid advances in the molecular analysis of individual subtypes, the heterogeneous nature of sarcomas limits the efficacy of targeted therapies (Cancer Genome Atlas Research Network, 2017; Linch et al., 2014), emphasizing the need to identify therapeutic vulnerabilities common to multiple STS subtypes. Although a diverse spectrum of oncogenic mutations has been recently described for in STS (Barretina et al., 2010; Cancer Genome Atlas Research Network, 2017; Eisinger-Mathason et al., 2015; Frith et al., 2013; Nakazawa et al., 2016a), it is increasingly clear that all tumors must adapt cell metabolism to support growth. Whereas metabolic reprogramming in STS has long been observed (Shaw et al., 1988), how this influences sarcoma growth is unclear. In the current study, we demonstrate that the gluconeogenic enzyme FBP2 is uniformly depleted in multiple sarcoma subtypes. Restoring FBP2 expression in sarcoma cells dramatically inhibited tumor cell growth both *in vitro* and *in vivo* (Figure 6-8), suggesting that FBP2 has tumor suppressive activities in sarcomas. We further discovered that FBP2 exhibits two distinct tumor-suppressive functions that depend on its subcellular localization. These results identify a specific metabolic adaptation as a common feature of STS and could help inform therapeutic strategies.

Tumor cells are typified by enhanced glycolysis, as a means of generating ATP and providing building blocks for macromolecule biosynthesis, sometimes known as the “Warburg effect” (Vander Heiden and DeBerardinis, 2017; Warburg, 1956). Reprogrammed glucose metabolism is induced by multiple mechanisms, such as the deregulation of oncoproteins and tumor suppressors (Hay, 2016). Previous studies uncovered frequently mutated genes in STS, including *TP53*, *NF1* and *PIK3CA* (Barretina et al., 2010; Frith et al., 2013), further confirmed by recent large-scale analyses of 206 adult soft tissue sarcomas representing 6 major subtypes using multi-platform molecular profiling (Cancer Genome Atlas Research Network, 2017). The p53 protein is involved in regulation of glucose metabolism by promoting OXPHOS and dampening glycolysis (Humpton and Vousden, 2016). Furthermore, *PIK3CA* mutations, among the most frequent somatic mutations found in STS

along with gain of function mutations in *c-KIT* and *PDGFRα*, are implicated in activation of the AKT/mTOR pathway (Fruman et al., 2017; Yuan and Cantley, 2008), stimulating a shift towards aerobic glycolysis (Lien et al., 2016). We show here that FBP2 loss also underlies increased glycolytic activity observed in sarcomas, as FBP2 re-expression inhibits glucose uptake and lactate secretion in distinct sarcoma cell lines. We also observed decreased glycolytic intermediates for biosynthesis in FBP2-expressing cells, such as glucose-6-phosphate, serine and glycine, consistent with previous speculation that FBP2 participates in the regulation of glycolysis (Newsholme and Crabtree, 1970). Furthermore, FBP2 restoration reduces PPP activity needed for ribonucleotide production and reducing equivalents in the form of NADPH.

Increasing evidence shows that multiple essential glycolytic/gluconeogenic enzymes localize to the nucleus and influence gene transcriptional regulation (Boukouris et al., 2016; Huangyang and Simon, 2018). We suggest a model in which metabolic enzymes transduce signals from growth factors, nutrient and oxygen availability, and external stress to modulate gene expression. We reported previously that nuclear FBP1 functions as a transcriptional corepressor to inhibit HIF-1α and its downstream targets, including genes associated with glucose metabolism (*GLUT1*, *LDHA*, and *PDK1*), therefore decreasing glycolytic phenotypes and enhancing glutamine uptake in tumor cells (Li et al., 2014). FBP2 has been previously shown to reside in nuclei of myogenic progenitor cells, cardiomyocytes and smooth muscle cells (Gizak and Dzugaj, 2003; Gizak et al., 2005; 2006), although its nuclear function was unclear. We determined that FBP2 nuclear activity suppresses sarcoma cell growth by inhibiting mitochondrial biogenesis and OXPHOS in a catalytic activity-independent manner, at least in part by repressing the expression of critical transcription factors NRF1 and TFAM. Of note, nuclear FBP2 also plays a role in suppressing glycolysis, as nucleus-excluded $FBP2^{4KA}$ exhibited less potent inhibition of glucose uptake and lactate secretion than wild-type FBP2, as indicated by [1,2-^{13}C]glucose labeling experiments (e.g. 26% decrease in glucose consumption by FBP2 versus 14% by $FBP2^{4KA}$, Figure 10B and Figure 13G). We can account for this based on decreased expression of c-Myc target genes in FBP2-expressing cells from RNA-seq (Figure 4G). c-Myc regulates virtually all genes involved in glycolysis (Dang et al., 2006),

including the essential glycolytic enzymes LDHA, PDK1 and ENO1, consistent with our observation that nuclear FBP2 also contributes to changes in glucose catabolism.

It's noteworthy that even though FBP1 and FBP2 have different tissue distributions, they share many functional similarities due to 77% sequence homology. For example, enforced expression of FBP1 in sarcoma cells or FBP2 in renal cancer cells suppresses tumor cell proliferation (Figure 23A-D). In addition, we showed that c-Myc transcriptional activity can also be suppressed by FBP1 in sarcoma cells (Figure 23E). Interestingly, in contrast to c-Myc, the effect of FBP1 and FBP2 on HIF signaling is tissue type-dependent. We consistently observed increased HRE luciferase activity upon FBP1/FBP2 expression in different sarcoma cell lines (Figure 23F-J). However, both proteins inhibit HIF transcriptional output in renal cancer cells. These results are in line with our previous findings that HIF2α is actually a tumor suppressor in soft tissue sarcoma, unlike kidney cancer (Nakazawa et al., 2016a) and increased HIF activity might also be involved in FBP2-mediated growth inhibition.

Recent isotope tracing analysis of human ccRCC confirmed enhanced glycolysis and suppressed glucose oxidation by the TCA cycle in these tumors (Courtney et al., 2018), likely due to HIF stabilization caused by frequent von Hippel-Lindau (*VHL*) mutations (Nickerson et al., 2008). However, sarcoma cells exhibited more active mitochondrial metabolism than ccRCC, as the incorporation rate of ^{13}C from [1,2-^{13}C]glucose into TCA cycle intermediates is faster (Figure 10E-F; see (Li et al., 2014)), suggesting that mitochondrial activity is critical for sarcoma progression. While earlier studies emphasized the importance of glycolysis, mitochondrial biosynthesis, bioenergetics, and signaling are also essential for tumorigenesis (Weinberg and Chandel, 2015). Intermediates from the TCA cycle, such as citrate, aspartate and glutamate, are precursors for macromolecule synthesis (lipid and nucleotides) to support biomass accumulation (Birsoy et al., 2015; Faubert et al., 2017; Hosios et al., 2016; Sellers et al., 2015). In addition, the mitochondrial ETC produces ROS via oxidative metabolism. Elevated ROS levels activate signaling pathways to promote cell proliferation and tumor progression (Schieber and Chandel, 2014). By inhibiting

mitochondrial function, FBP2 reduces the abundance of TCA cycle intermediates, ATP, and ROS, therefore inhibiting cell growth.

A key observation is that FBP2 co-localizes with the c-Myc oncogene at the *TFAM* promoter, suggesting that FBP2 acts as a nuclear c-Myc transcriptional corepressor. c-Myc affects a large spectrum of genes involved in mitochondrial function (Kim and Dang, 2005) and directly activates *TFAM* expression. Given the multitude of biological processes c-Myc regulates, the precise mechanisms whereby FBP2 specifically targets c-Myc-induced mitochondrial biogenesis remain to be elucidated. Presumably, additional factors are required to regulate c-Myc driven targets associated with mitochondrial functions. Another nuclearly-encoded transcription factor, NRF1 is key to mitochondrial biogenesis and also an upstream regulator of *TFAM* (Kelly and Scarpulla, 2004). Decreased *NRF1* expression in FBP2-expressing cells further explains reduced TFAM activity in this context.

Interestingly, FBP2 has been reported to translocate from the nucleus to the cytosol during myoblast differentiation (Gizak et al., 2006), which corresponds to a shift from a highly glycolytic state to increased OXPHOS needed in fully developed muscle cells (Remels et al., 2010). We suggest that FBP2 is restricted to the nucleus in muscle progenitors to transcriptionally suppress mitochondrial biogenesis and OXPHOS, as undifferentiated cells frequently favor glycolytic metabolism. At the onset of differentiation, FBP2 exits the nucleus and functions as a gluconeogenic/glycogen producing enzyme to antagonize glycolysis in the cytosol. How FBP2 translocation is regulated and whether subcellular shuttling of FBP2 contributes to muscle differentiation are unclear, and remain part of our future studies. It will also be important to evaluate the role of FBP2 in adipogenic differentiation, another lineage derived from mesenchymal stem cells.

In summary, our findings demonstrate a role for FBP2 in suppressing sarcoma progression and further establish dual tumor-suppressive functions of FBP, including promoting gluconeogenesis and inhibiting mitochondrial biogenesis by inhibiting c-Myc transcriptional activity (Figure 24).

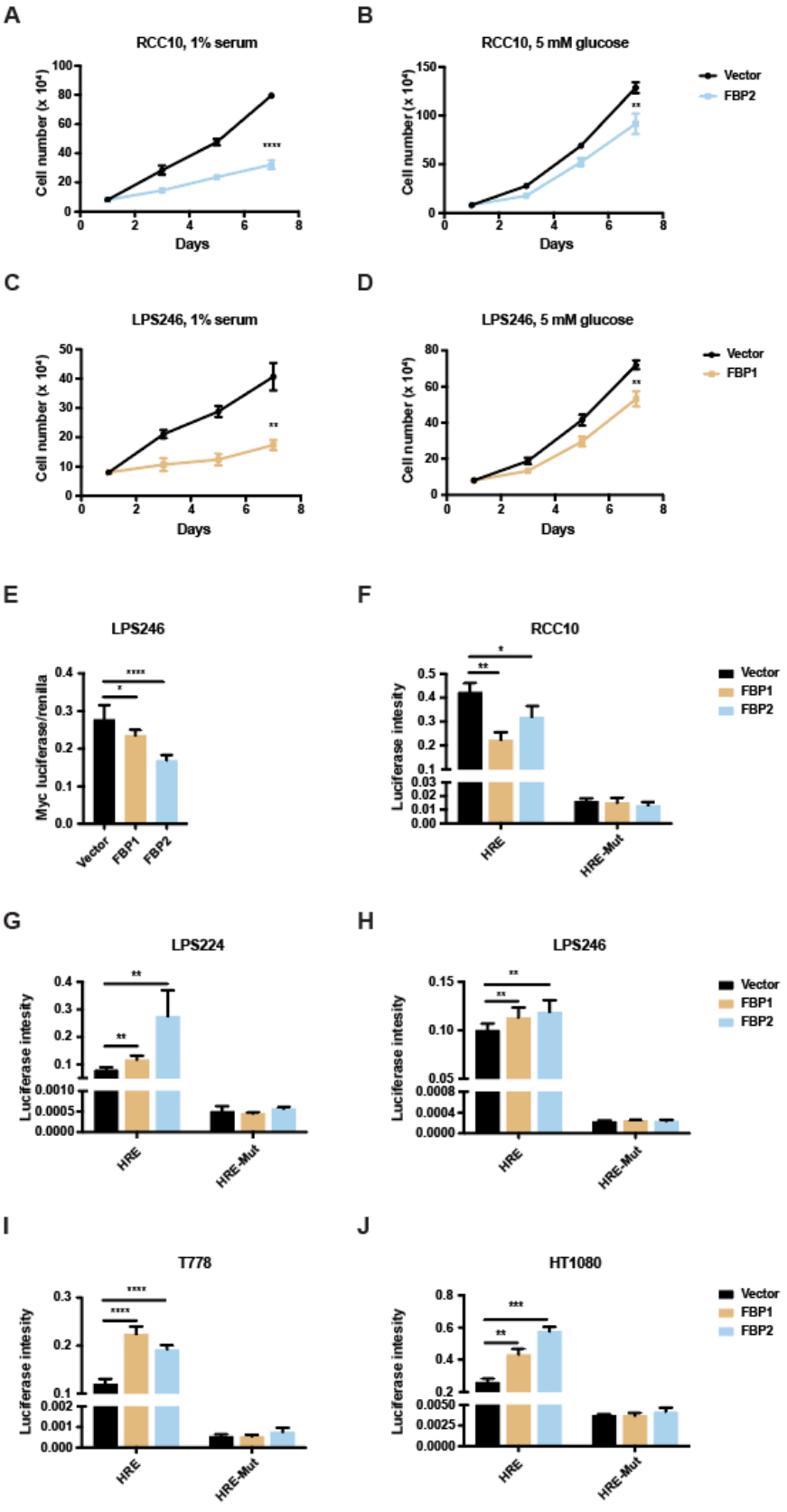
A
RCC10, 1% serum
Cell number (x 10⁴)
Days
****
B
RCC10, 5 mM glucose
Cell number (x 10⁴)
Days
**
Vector
FBP2
C
LPS246, 1% serum
Cell number (x 10⁴)
Days
**
D
LPS246, 5 mM glucose
Cell number (x 10⁴)
Days
**
Vector
FBP1
E
LPS246
Myc luciferase/renilla
****
*
Vector
FBP1
FBP2
F
RCC10
Luciferase intesity
*
**
HRE
HRE-Mut
Vector
FBP1
FBP2
G
LPS224
Luciferase intesity
**
**
HRE
HRE-Mut
H
LPS246
Luciferase intesity
**
**
HRE
HRE-Mut
Vector
FBP1
FBP2
I
T778
Luciferase intesity
****
****
HRE
HRE-Mut
J
HT1080
Luciferase intesity
***
**
HRE
HRE-Mut
Vector
FBP1
FBP2

Figure 23. Functional similarity of FBP1 and FBP2 in different tumor type.

(A and B) Growth of RCC10 cells in low serum medium (1% FBS) (A) or low glucose medium (5 mM glucose) (B), with or without ectopic FBP2 expression.

(C and D) Growth of LPS246 cells in low serum medium (1% FBS) (C) or low glucose medium (5 mM glucose) (D), with or without ectopic FBP1 expression.

(E) c-Myc reporter activity measured in vector-, FBP1- or FBP2-expressing LPS246 cells transfected with Myc/Max luciferase reporter. Transfection efficiencies were normalized to co-transfected pRenilla-luciferase.

(F-J) HRE reporter activity measured in vector-, FBP1- or FBP2-expressing RCC10 cells (F), LPS224 cells (G), LPS246 cells (H), T778 cells (I), and HT1080 cells (J) transfected with Myc/Max luciferase reporter. Transfection efficiencies were normalized to co-transfected pRenilla-luciferase. n = 3, *$p < 0.05$, **$p < 0.01$, ***$p < 0.001$, ****$p < 0.0001$.

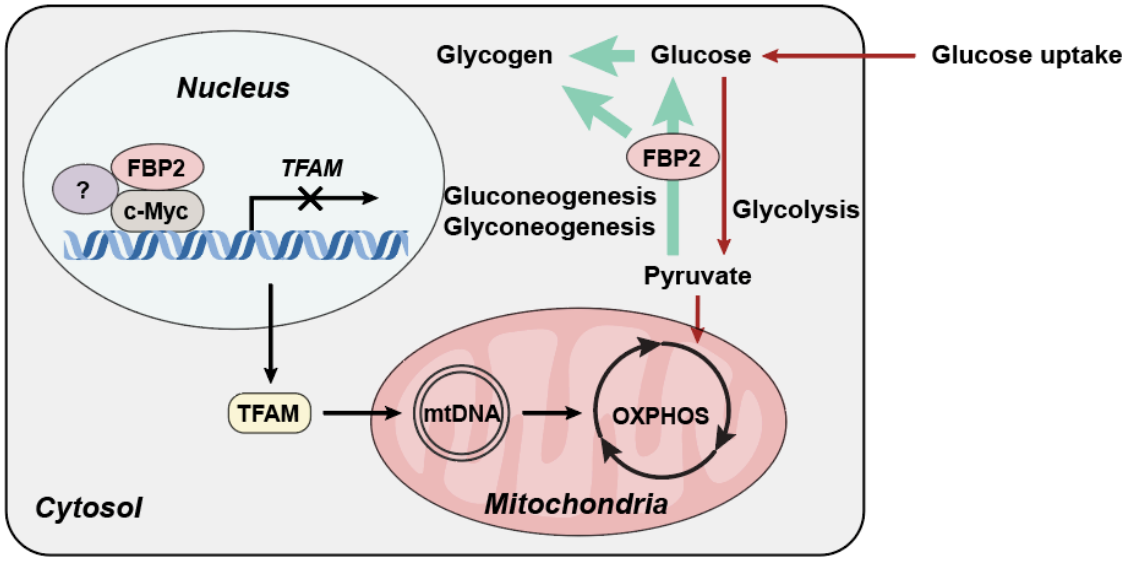

Figure 24. Model depicting the metabolic status, transcription activity and mitochondrial change of sarcoma cells upon FBP2 re-expression. The cytosolic FBP2 inhibits glycolysis and following TCA cycle. The nuclear FBP2 restrains mitochondrial function by co-localizing with c-Myc at the promoter region of *TFAM*, a nuclearly encoded transcription factor that is crucial for mitochondrial biogenesis.

CHAPTER 4 CONCLUSIONS

Over the past decade, study of cellular metabolism has been rigorously revisited, especially in the field of cancer research, revealing new insights that significantly expand our understanding of cancer. However, general metabolic alterations in soft tissue sarcomas are largely understudied and there appear to be at least some common phenotypes among diverse sarcoma subtypes. The extent of soft tissue sarcoma heterogeneity has led to questions about the usefulness of targeting individual signaling molecules as a practical therapeutic strategy. As described in Chapter 1, abnormal glucose metabolism, which has long been observed in sarcoma patients, could be exploited as a potential therapeutic target. In order to expand our understanding of increased glucose catabolism in sarcoma patients, my thesis aims to investigate the impact of FBP2 loss on sarcoma progression by depicting its canonical enzymatic activity in gluconeogenesis and non-canonical functions in the nucleus. I determined that FBP2 exhibits two distinct tumor-suppressive functions depending on its subcellular localization.

In Chapter 3, I demonstrated that FBP2 re-expression in sarcoma cells significantly suppresses tumor cell growth both *in vitro* and *in vivo*, indicating that FBP2 acts as a tumor suppressor in sarcomas. I further revealed that FBP2 restoration significantly inhibits glycolysis, the TCA cycle and the pentose phosphate pathway. However, decreased glycolytic activity is not only based on FBP2's catalytic activity, as ectopic expression of nuclear excluded $FBP2^{4KA}$ exhibited less potent inhibition of glycolysis. These results indicate that nuclear FBP2 is also implicated in regulating glucose metabolism.

Interestingly, accumulating evidence indicates that various metabolic enzymes have surprisingly novel activities outside of their established metabolic roles, including regulating gene expression, cell cycle progression, and apoptosis (Huangyang and Simon, 2018). Many of these new functions are activated in response to growth factor signaling, nutrient and oxygen availability, and external stress. As such, multifaceted enzymes directly link metabolism to transcription, engaging diverse physiological and pathological processes to maintain cell homeostasis. We compared the

transcriptome between control and FBP2-expressing LPS246 cells, and determined that mitochondrial dysfunction is the primary differentially expressed functional category. We further confirmed that nuclear FBP2 mediates the suppression of mitochondrial function by inhibiting the expression of TFAM and NRF1, two crucial nuclear regulators of mitochondrial biogenesis. Moreover, we determined that nuclear FBP2 colocalizes with the c-Myc transcription factor at the *TFAM* promoter region and represses c-Myc-dependent *TFAM* activation. Collectively, these data add to our current understanding of FBP2's role in sarcoma progression and provide implications for STS metabolic reprogramming that should guide future clinical treatment.

Future directions

Restoring FBP2 expression in soft tissue sarcoma.

Previous studies have shown that *FBP1* epigenetic repression is common in several cancers, such as hepatocellular carcinoma (HCC), and colon and non-small cell lung, and breast cancer (Bigl et al., 2008; Chen et al., 2011; Liu et al., 2018). Specifically, in breast cancer cells, histone methyltransferase G9a and DNA methyltransferase DNMT1 are recruited to the *FBP1* promoter by Snail, a critical factor in epithelial-to-mesenchymal transitions (EMTs), resulting in increased H3K9me2 and DNA methylation (Dong et al., 2013). Similarly, in lung cancer cells, zinc finger E-box-binding homeobox 1 (ZEB1) increases DNA methylation by binding to *FBP1*'s promoter (Zhang et al., 2016). In addition, pharmacological inhibition of histone demethylase LSD1 by tranylcypromine remarkably upregulated *FBP1* expression (Pan et al., 2013). Histone deacetylation is also involved in downregulating *FBP1*, as low FBP1 levels are correlated with high levels of histone deacetylase 1 (HDAC1) and HDAC2 proteins, and decreased histone H3K27 acetylation at *FBP1*'s enhancer in HCC patient tissues (Yang et al., 2017). Importantly, HDAC inhibitors, such as sodium butyrate, SAHA and LBH589, restored FBP1 expression in a dose-dependent manner (Yang et al., 2017). Interestingly, ubiquitin-mediated degradation provides another layer of regulation of FBP1 protein abundance in HCC, in that MAGE-A3 and MAGE-C2, which are known to be overexpressed in HCC, form ubiquitin ligase complexes with the tripartite motif-containing protein 28 (TRIM28) and facilitate TRIM28-dependent degradation of FBP1 (Jin et al., 2017).

As discussed above, diverse inhibitors of deacetylases or methyltransferases have been examined in cancers exhibiting *FBP1* silencing. In Chapter 3, I showed that *FBP2* expression is uniformly downregulated in a broad spectrum of sarcoma subtypes (Figure 2-3). Analysis of TCGA sarcoma database indicates that FBP2 loss is not due to copy number variation, but rather through epigenetic silencing, such as DNA and histone hypermethylation (data not shown). However, in sarcoma cells, epigenetic profiling and associated transcription factors at the *FBP2* promoter remain to be uncovered. Therefore, it will be interesting to investigate the underlying mechanisms of *FBP2* downregulation, and test several epigenetic inhibitors or activators to restore *FBP2* expression in sarcoma cells in the future.

Investigating the role of FBP2 in sarcoma initiation.

In this thesis, the main question I asked is: how is FBP2 loss affects sarcoma progression? However, *FBP2* mRNA levels are significantly decreased in tumors at early stages relative to normal tissues, strongly indicating that FBP2 depletion is an essential step during sarcomagenesis. To determine whether FBP2 loss contributes to sarcoma initiation, we will delete *FBP2* in a genetically engineered sarcoma mouse model, and assess whether FBP2 loss accelerates tumor formation. Our lab utilizes a "KP" murine model, where adenovirus-expressing Cre recombinase (Adeno-Cre) injection into gastrocnemius muscle simultaneously drives expression of oncogeneic $Kras^{G12D}$ and deletion of *Trp53* (Eisinger-Mathason et al., 2013; Kirsch et al., 2007; Mito et al., 2009). These genetic changes occur frequently in sarcoma, and murine tumors that develop recapitulate human UPS morphologically, histologically, and genetically. We will use a CRISPR/Cas9 system to delete *FBP2* in this KP model. CRISPR-Cas9 knockin mice were previously generated by inserting a *Cas9* transgene expression cassette into the Cre-dependent *Rosa26* locus for genome editing and cancer modeling (Platt et al., 2014). We crossed the CRISPR-Cas9 knockin mice with KP mice to generate Cas9KP mice, and therefore AAV-Cre injection should simultaneously activate Cas9 and oncogenic *Kras*, and deplete *p53*. The use of Cas9 mice in conjunction with *sgRNA* delivery allowed us to introduce an FBP2 knockout in the same animal to more closely recapitulate the nature of mutation accumulation in evolving tumors.

By comparing tumor initiation time between Cas9KP mice injected with AAV-Cre-sgLacZ or AAV-Cre-sgFBP2, we will be able to answer whether FBP2 loss is an essential event during early sarcomagenesis.

Exploring the potential correlation between muscle differentiation and FBP2 subcellular localization.

For some time, FBP2 has been considered as a key enzyme of glycogen synthesis, which is soluble and freely diffused in the cytoplasm. However, a previous study indicates that in dividing myoblasts, FBP2 is localized to both cytosol and nuclei; whereas in differentiated myofibers, FBP2 is restricted to the cytosolic compartment (Gizak et al., 2006). In addition, my preliminary data also showed FBP2 translocation from nucleus to cytosol in human and mouse myoblast. Interestingly, the nuclear-cytosolic shuttling during muscle differentiation is consistent with my findings of FBP2's specific functions in different cellular compartments described in this thesis. A shift from a highly glycolytic state to relying predominantly on OXPHOS has been observed during skeletal myoblast differentiation (Remels et al., 2010). We conclude that FBP2 is restricted to the nucleus in muscle progenitors, and transcriptionally suppresses mitochondrial biogenesis and OXPHOS. At the onset of differentiation, FBP2 exits the nucleus and functions as a gluconeogenic/glycogen producing enzyme to antagonize glycolysis in the cytosol. Of note, previous studies showed that cytosolic FBP2 binds to mitochondria and protects mitochondria from calcium-induced mitochondrial swelling and ensures ATP production in cardiomyocytes (Gizak and Rakus, 2012; 2014). The differential acts of FBP2 on mitochondria depends on its subcellular localizations, reflecting a complex and exquisite control of energy usage on each differentiation stage of these cells.

A conserved nuclear localization sequence "$_{203}$KKKGK$_{207}$" was identified in FBP1 and FBP2 (Gizak et al., 2005; 2009a). Interestingly, a potential target of Casein Kinase 2, Ser 10, is located closely to FBP2's NLS sequence, suggesting that nuclear transport of FBP2 might be regulated by phosphorylation of this amino acid residue (Gizak et al., 2005). We speculate that nutrient availability and growth factor signaling affect FBP2 translocation, and therefore activate its different functions in the cytosol and nucleus. However, the underlying mechanisms of FBP2 translocation

and whether subcellular shuttling of FBP2 contributes to muscle differentiation are unclear, and remain part of our future studies.

Bibliography

Ahmad, A., Aboukameel, A., Kong, D., Wang, Z., Sethi, S., Chen, W., Sarkar, F.H., and Raz, A. (2011). Phosphoglucose isomerase/autocrine motility factor mediates epithelial-mesenchymal transition regulated by miR-200 in breast cancer cells. Cancer Res. *71*, 3400–3409.

Ahuatzi, D., Herrero, P., la Cera, de, T., and Moreno, F. (2004). The glucose-regulated nuclear localization of hexokinase 2 in Saccharomyces cerevisiae is Mig1-dependent. Journal of Biological Chemistry *279*, 14440–14446.

Åsberg, C., Hjalmarson, O., Alm, J., Martinsson, T., Waldenström, J., and Hellerud, C. (2010). Fructose 1,6-bisphosphatase deficiency: enzyme and mutation analysis performed on calcitriol-stimulated monocytes with a note on long-term prognosis. J Inherit Metab Dis *33*, 113–121.

Barretina, J., Taylor, B.S., Banerji, S., Ramos, A.H., Lagos-Quintana, M., Decarolis, P.L., Shah, K., Socci, N.D., Weir, B.A., Ho, A., et al. (2010). Subtype-specific genomic alterations define new targets for soft-tissue sarcoma therapy. Nat. Genet. *42*, 715–721.

Bigl, M., Jandrig, B., Horn, L.-C., and Eschrich, K. (2008). Aberrant methylation of human L- and M-fructose 1,6-bisphosphatase genes in cancer. Biochemical and Biophysical Research Communications *377*, 720–724.

Birsoy, K., Wang, T., Chen, W.W., Freinkman, E., Abu-Remaileh, M., and Sabatini, D.M. (2015). An Essential Role of the Mitochondrial Electron Transport Chain in Cell Proliferation Is to Enable Aspartate Synthesis. Cell *162*, 540–551.

Boukouris, A.E., Zervopoulos, S.D., and Michelakis, E.D. (2016). Metabolic Enzymes Moonlighting in the Nucleus: Metabolic Regulation of Gene Transcription. Trends in Biochemical Sciences *41*, 712–730.

Brizel, D.M., Scully, S.P., Harrelson, J.M., Layfield, L.J., Bean, J.M., Prosnitz, L.R., and Dewhirst, M.W. (1996). Tumor oxygenation predicts for the likelihood of distant metastases in human soft tissue sarcoma. Cancer Res. *56*, 941–943.

Buscaglia, C.A., Penesetti, D., Tao, M., and Nussenzweig, V. (2006). Characterization of an aldolase-binding site in the Wiskott-Aldrich syndrome protein. Journal of Biological Chemistry *281*, 1324–1331.

Cai, L., Sutter, B.M., Li, B., and Tu, B.P. (2011). Acetyl-CoA induces cell growth and proliferation by promoting the acetylation of histones at growth genes. Molecular Cell *42*, 426–437.

Cancer Genome Atlas Research Network (2017). Comprehensive and Integrated Genomic Characterization of Adult Soft Tissue Sarcomas. Cell *171*, 950–965.e28.

Castonguay, Z., Auger, C., Thomas, S.C., Chahma, M., and Appanna, V.D. (2014). Nuclear lactate dehydrogenase modulates histone modification in human hepatocytes. Biochemical and Biophysical Research Communications *454*, 172–177.

Chatterjee, A., Dasgupta, S., and Sidransky, D. (2011). Mitochondrial Subversion in Cancer. Cancer Prev Res *4*, 638–654.

Chen, M., Zhang, J., Li, N., Qian, Z., Zhu, M., Li, Q., Zheng, J., Wang, X., and Shi, G. (2011). Promoter hypermethylation mediated downregulation of FBP1 in human hepatocellular carcinoma and colon cancer. PLoS ONE *6*, e25564.

Chen, X.J., Wang, X., Kaufman, B.A., and Butow, R.A. (2005). Aconitase couples metabolic regulation to mitochondrial DNA maintenance. Science *307*, 714–717.

Cheng, C., Ru, P., Geng, F., Liu, J., Yoo, J.Y., Wu, X., Cheng, X., Euthine, V., Hu, P., Guo, J.Y., et al. (2015). Glucose-Mediated N-glycosylation of SCAP Is Essential for SREBP-1 Activation and Tumor Growth. Cancer Cell *28*, 569–581.

Cheung, E.C., Ludwig, R.L., and Vousden, K.H. (2012). Mitochondrial localization of TIGAR under hypoxia stimulates HK2 and lowers ROS and cell death. Proc. Natl. Acad. Sci. U.S.a. *109*, 20491–20496.

Chiara, F., Castellaro, D., Marin, O., Petronilli, V., Brusilow, W.S., Juhaszova, M., Sollott, S.J., Forte, M., Bernardi, P., and Rasola, A. (2008). Hexokinase II detachment from mitochondria triggers apoptosis through the permeability transition pore independent of voltage-dependent anion channels. PLoS ONE *3*, e1852.

Cieśla, M., Mierzejewska, J., Adamczyk, M., Farrants, A.-K.Ö., and Boguta, M. (2014). Fructose bisphosphate aldolase is involved in the control of RNA polymerase III-directed transcription. Biochimica Et Biophysica Acta *1843*, 1103–1110.

Courtney, K.D., Bezwada, D., Mashimo, T., Pichumani, K., Vemireddy, V., Funk, A.M., Wimberly, J., McNeil, S.S., Kapur, P., Lotan, Y., et al. (2018). Isotope Tracing of Human Clear Cell Renal Cell Carcinomas Demonstrates Suppressed Glucose Oxidation In Vivo. Cell Metabolism *28*, 793–800.e2.

Dang, C.V., O'Donnell, K.A., Zeller, K.I., Nguyen, T., Osthus, R.C., and Li, F. (2006). The c-Myc target gene network. Semin. Cancer Biol. *16*, 253–264.

Detwiller, K.Y., Fernando, N.T., Segal, N.H., Ryeom, S.W., D'Amore, P.A., and Yoon, S.S. (2005). Analysis of hypoxia-related gene expression in sarcomas and effect of hypoxia on RNA interference of vascular endothelial cell growth factor A. Cancer Res. *65*, 5881–5889.

Dickinson, A., Yeung, K.Y., Donoghue, J., Baker, M.J., Kelly, R.D., McKenzie, M., Johns, T.G., and John, J.C.S. (2013). The regulation of mitochondrial DNA copy number in glioblastoma cells. Cell Death Differ *20*, 1644.

Dong, C., Yuan, T., Wu, Y., Wang, Y., Fan, T.W.M., Miriyala, S., Lin, Y., Yao, J., Shi, J., Kang, T., et al. (2013). Loss of FBP1 by Snail-mediated repression provides metabolic advantages in basal-like breast cancer. Cancer Cell *23*, 316–331.

Eisinger-Mathason, T.S.K., Mucaj, V., Biju, K.M., Nakazawa, M.S., Gohil, M., Cash, T.P., Yoon, S.S., Skuli, N., Park, K.M., Gerecht, S., et al. (2015). Deregulation of the Hippo pathway in soft-tissue sarcoma promotes FOXM1 expression and tumorigenesis. Proc. Natl. Acad. Sci. U.S.a. *112*, E3402–E3411.

Eisinger-Mathason, T.S.K., Zhang, M., Qiu, Q., Skuli, N., Nakazawa, M.S., Karakasheva, T., Mucaj, V., Shay, J.E.S., Stangenberg, L., Sadri, N., et al. (2013). Hypoxia-dependent modification of collagen networks promotes sarcoma metastasis. Cancer Discov *3*, 1190–1205.

Enzo, E., Santinon, G., Pocaterra, A., Aragona, M., Bresolin, S., Forcato, M., Grifoni, D., Pession, A., Zanconato, F., Guzzo, G., et al. (2015). Aerobic glycolysis tunes YAP/TAZ transcriptional activity. Embo J. *34*, e201490379–e201491370.

Faubert, B., Li, K.Y., Cai, L., Hensley, C.T., Kim, J., Zacharias, L.G., Yang, C., Do, Q.N., Doucette, S., Burguete, D., et al. (2017). Lactate Metabolism in Human Lung Tumors. Cell *171*, 358–371.e359.

Feo, S., Arcuri, D., Piddini, E., Passantino, R., and Giallongo, A. (2000). ENO1 gene product binds to the c-myc promoter and acts as a transcriptional repressor: relationship with Myc promoter-binding protein 1 (MBP-1). FEBS Letters *473*, 47–52.

Fletcher, C.D.M. (2014). The evolving classification of soft tissue tumours - an update based on the new 2013 WHO classification. Histopathology *64*, 2–11.

Frith, A.E., Hirbe, A.C., and Van Tine, B.A. (2013). Novel pathways and molecular targets for the treatment of sarcoma. Curr Oncol Rep *15*, 378–385.

Fruman, D.A., Chiu, H., Hopkins, B.D., Bagrodia, S., Cantley, L.C., and Abraham, R.T. (2017). The PI3K Pathway in Human Disease. Cell *170*, 605–635.

Fu, M., Li, L., Albrecht, T., Johnson, J.D., Kojic, L.D., and Nabi, I.R. (2011). Autocrine motility factor/phosphoglucose isomerase regulates ER stress and cell death through control of ER calcium release. Cell Death Differ *18*, 1057–1070.

Funasaka, T., Hu, H., Hogan, V., and Raz, A. (2007a). Down-regulation of phosphoglucose isomerase/autocrine motility factor expression sensitizes human fibrosarcoma cells to oxidative stress leading to cellular senescence. Journal of Biological Chemistry *282*, 36362–36369.

Funasaka, T., Hu, H., Yanagawa, T., Hogan, V., and Raz, A. (2007b). Down-regulation of phosphoglucose isomerase/autocrine motility factor results in mesenchymal-to-epithelial transition of human lung fibrosarcoma cells. Cancer Res. *67*, 4236–4243.

Gao, X., Wang, H., Yang, J.J., Liu, X., and Liu, Z.-R. (2012). Pyruvate kinase M2 regulates gene transcription by acting as a protein kinase. Molecular Cell *45*, 598–609.

Gentile, T.L., Lu, C., Lodato, P.M., Tse, S., Olejniczak, S.H., Witze, E.S., Thompson, C.B., and Wellen, K.E. (2013). DNMT1 Is Regulated by ATP-Citrate Lyase and Maintains Methylation Patterns during Adipocyte Differentiation. Mol. Cell. Biol. *33*, 3864–3878.

Ghosh, A.K., Steele, R., and Ray, R.B. (1999a). Functional domains of c-myc promoter binding protein 1 involved in transcriptional repression and cell growth regulation. Mol. Cell. Biol. *19*, 2880–2886.

Ghosh, A.K., Steele, R., and Ray, R.B. (1999b). MBP-1 physically associates with histone deacetylase for transcriptional repression. Biochemical and Biophysical Research Communications *260*, 405–409.

Gizak, A., and Dzugaj, A. (2003). FBPase is in the nuclei of cardiomyocytes. FEBS Letters *539*, 51–55.

Gizak, A., Rakus, D., and Dzugaj, A. (2005). Nuclear Localization of Fructose 1,6-bisphosphatase in Smooth Muscle Cells. J Mol Hist *36*, 243–248.

Gizak, A., Wrobel, E., Moraczewski, J., and Dzugaj, A. (2006). Changes in subcellular localization of fructose 1,6-bisphosphatase during differentiation of isolated muscle satellite cells. FEBS Letters *580*, 4042–4046.

Gizak, A., and Rakus, D. (2012). Muscle FBPase binds to cardiomyocyte mitochondria under glycogen synthase kinase-3 inhibition or elevation of cellular Ca2+ level. FEBS Letters *586*, 13–19.

Gizak, A., and Rakus, D. (2014). Changes in quaternary structure of muscle fructose-1,6-bisphosphatase regulate affinity of the enzyme to mitochondria. Int. J. Biochem *48*, 55–59.

Gizak, A., Maciaszczyk-Dziubinska, E., Maciaszczyk-Dziubinska, E., Jurowicz, M., Jurowicz, M., and Rakus, D. (2009a). Muscle FBPase is targeted to nucleus by its 203KKKGK 207sequence. Proteins *77*, 262–267.

Gizak, A., Zarzycki, M., and Rakus, D. (2009b). Nuclear targeting of FBPase in HL-1 cells is controlled by beta-1 adrenergic receptor-activated Gs protein signaling cascade. Biochimica Et Biophysica Acta *1793*, 871–877.

Gobble, R.M., Qin, L.-X., Brill, E.R., Angeles, C.V., Ugras, S., O'Connor, R.B., Moraco, N.H., Decarolis, P.L., Antonescu, C., and Singer, S. (2011). Expression profiling of liposarcoma yields a multigene predictor of patient outcome and identifies genes that contribute to liposarcomagenesis. Cancer Res. *71*, 2697–2705.

Gottlob, K., Majewski, N., Kennedy, S., Kandel, E., Robey, R.B., and Hay, N. (2001). Inhibition of early apoptotic events by Akt/PKB is dependent on the first committed step of glycolysis and mitochondrial hexokinase. Genes & Development *15*, 1406–1418.

Grosse, F., Nasheuer, H.P., Scholtissek, S., and Schomburg, U. (1986). Lactate dehydrogenase and glyceraldehyde-phosphate dehydrogenase are single-stranded DNA-binding proteins that affect the DNA-polymerase-alpha-primase complex. Eur. J. Biochem. *160*, 459–467.

Hara, M.R., Agrawal, N., Kim, S.F., Cascio, M.B., Fujimuro, M., Ozeki, Y., Takahashi, M., Cheah, J.H., Tankou, S.K., Hester, L.D., et al. (2005). S-nitrosylated GAPDH initiates apoptotic cell death by nuclear translocation following Siah1 binding. Nature Cell Biology *7*, 665–674.

Hay, N. (2016). Reprogramming glucose metabolism in cancer: can it be exploited for cancer therapy? Nat Rev Cancer *16*, 635–649.

Hirata, H., Sugimachi, K., Komatsu, H., Ueda, M., Masuda, T., Uchi, R., Sakimura, S., Nambara, S., Saito, T., Shinden, Y., et al. (2016). Decreased Expression of Fructose-1,6-bisphosphatase Associates with Glucose Metabolism and Tumor Progression in Hepatocellular Carcinoma. Cancer Res. *76*, 3265–3276.

Hosios, A.M., Fiske, B.P., Gui, D.Y., and Vander Heiden, M.G. (2015). Lack of Evidence for PKM2 Protein Kinase Activity. Molecular Cell *59*, 850–857.

Hosios, A.M., Hecht, V.C., Danai, L.V., Johnson, M.O., Rathmell, J.C., Steinhauser, M.L., Manalis, S.R., and Vander Heiden, M.G. (2016). Amino Acids Rather than Glucose Account for the Majority of Cell Mass in Proliferating Mammalian Cells. Dev. Cell *36*, 540–549.

Hsu, K.-W., Hsieh, R.-H., Lee, Y.-H.W., Chao, C.-H., Wu, K.-J., Tseng, M.-J., and Yeh, T.-S. (2008). The activated Notch1 receptor cooperates with alpha-enolase and MBP-1 in modulating c-myc activity. Mol. Cell. Biol. *28*, 4829–4842.

Huangyang, P., and Simon, M.C. (2018). Hidden features: exploring the non-canonical functions of metabolic enzymes. Dis Model Mech *11*, dmm033365.

Humpton, T.J., and Vousden, K.H. (2016). Regulation of Cellular Metabolism and Hypoxia by p53. Cold Spring Harb Perspect Med *6*, a026146.

Ishitani, R., Kimura, M., Sunaga, K., Katsube, N., Tanaka, M., and Chuang, D.M. (1996). An antisense oligodeoxynucleotide to glyceraldehyde-3-phosphate dehydrogenase blocks age-

induced apoptosis of mature cerebrocortical neurons in culture. J. Pharmacol. Exp. Ther. *278*, 447–454.

Ishitani, R., and Chuang, D.-M. (1996). Glyceraldehyde-3-phosphate dehydrogenase antisense oligodeoxynucleotides protect against cytosine arabinonucleoside-induced apoptosis in cultured cerebellar. Proc. Natl. Acad. Sci. U.S.a. *93*, 1–5.

Jiang, Y., Li, X., Yang, W., Hawke, D.H., Zheng, Y., Xia, Y., Aldape, K., Wei, C., Guo, F., Chen, Y., et al. (2014a). PKM2 regulates chromosome segregation and mitosis progression of tumor cells. Molecular Cell *53*, 75–87.

Jiang, Y., Qian, X., Shen, J., Wang, Y., Li, X., Liu, R., Xia, Y., Chen, Q., Peng, G., Lin, S.-Y., et al. (2015). Local generation of fumarate promotes DNA repair through inhibition of histone H3 demethylation. Nat. Cell Biol. *17*, 1158–1168.

Jiang, Y., Wang, Y., Wang, T., Hawke, D.H., Zheng, Y., Li, X., Zhou, Q., Majumder, S., Bi, E., Liu, D.X., et al. (2014b). PKM2 phosphorylates MLC2 and regulates cytokinesis of tumour cells. Nat Commun *5*, 5566.

Jin, X., Pan, Y., Wang, L., Zhang, L., Ravichandran, R., Potts, P.R., Jiang, J., Wu, H., and Huang, H. (2017). MAGE-TRIM28 complex promotes the Warburg effect and hepatocellular carcinoma progression by targeting FBP1 for degradation. Oncogenesis *6*, e312–e312.

Kaelin, W.G., and McKnight, S.L. (2013). Influence of metabolism on epigenetics and disease. Cell *153*, 56–69.

Kao, A.W., Noda, Y., Johnson, J.H., Pessin, J.E., and Saltiel, A.R. (1999). Aldolase mediates the association of F-actin with the insulin-responsive glucose transporter GLUT4. Journal of Biological Chemistry *274*, 17742–17747.

Katoh, Y., Ikura, T., Hoshikawa, Y., Tashiro, S., Ito, T., Ohta, M., Kera, Y., Noda, T., and Igarashi, K. (2011). Methionine adenosyltransferase II serves as a transcriptional corepressor of Maf oncoprotein. Molecular Cell *41*, 554–566.

Kelly, D.P., and Scarpulla, R.C. (2004). Transcriptional regulatory circuits controlling mitochondrial biogenesis and function. Genes & Development *18*, 357–368.

Kim, J.-W., and Dang, C.V. (2005). Multifaceted roles of glycolytic enzymes. Trends in Biochemical Sciences *30*, 142–150.

Kim, J.-W., Tchernyshyov, I., Semenza, G.L., and Dang, C.V. (2006). HIF-1-mediated expression of pyruvate dehydrogenase kinase: a metabolic switch required for cellular adaptation to hypoxia. Cell Metabolism *3*, 177–185.

Kirsch, D.G., Dinulescu, D.M., Miller, J.B., Grimm, J., Santiago, P.M., Young, N.P., Nielsen, G.P., Quade, B.J., Chaber, C.J., Schultz, C.P., et al. (2007). A spatially and temporally restricted mouse model of soft tissue sarcoma. Nat. Med. *13*, 992–997.

Kumble, K.D., and Vishwanatha, J.K. (1991). Immunoelectron microscopic analysis of the intracellular distribution of primer recognition proteins, annexin 2 and phosphoglycerate kinase, in normal and transformed cells. J. Cell. Sci. *99*, 751–758.

La Cera, De, T., Herrero, P., Moreno-Herrero, F., Chaves, R.S., and Moreno, F. (2002). Mediator factor Med8p interacts with the hexokinase 2: implication in the glucose signalling pathway of Saccharomyces cerevisiae. J. Mol. Biol. *319*, 703–714.

Lee, J.V., Carrer, A., Shah, S., Snyder, N.W., Wei, S., Venneti, S., Worth, A.J., Yuan, Z.-F., Lim, H.-W., Liu, S., et al. (2014). Akt-dependent metabolic reprogramming regulates tumor cell histone acetylation. Cell Metabolism *20*, 306–319.

Lee, J., Kim, H.K., Han, Y.-M., and Kim, J. (2008). Pyruvate kinase isozyme type M2 (PKM2) interacts and cooperates with Oct-4 in regulating transcription. Int. J. Biochem *40*, 1043–1054.

Lee, K.-M., Giltnane, J.M., Balko, J.M., Schwarz, L.J., Guerrero-Zotano, A.L., Hutchinson, K.E., Nixon, M.J., Estrada, M.V., Sánchez, V., Sanders, M.E., et al. (2017). MYC and MCL1 Cooperatively Promote Chemotherapy-Resistant Breast Cancer Stem Cells via Regulation of Mitochondrial Oxidative Phosphorylation. Cell Metabolism *26*, 633–647.e637.

Lee, S.M., Kim, J.H., Cho, E.J., and Youn, H.D. (2009). A nucleocytoplasmic malate dehydrogenase regulates p53 transcriptional activity in response to metabolic stress. Cell Death Differ *16*, 738–748.

Lee, W.N., Boros, L.G., Puigjaner, J., Bassilian, S., Lim, S., and Cascante, M. (1998). Mass isotopomer study of the nonoxidative pathways of the pentose cycle with [1,2-13C2]glucose. Am. J. Physiol. *274*, E843–E851.

Lehnhardt, M., Daigeler, A., Homann, H.H., Schwaiberger, V., Goertz, O., Kuhnen, C., and Steinau, H.U. (2009). MFH revisited: outcome after surgical treatment of undifferentiated pleomorphic or not otherwise specified (NOS) sarcomas of the extremities -- an analysis of 140 patients. Langenbecks Arch Surg *394*, 313–320.

Li, B., Li, B., Qiu, B., Qiu, B., Lee, D.S.M., Lee, D.S.M., Walton, Z.E., Walton, Z.E., Ochocki, J.D., Ochocki, J.D., et al. (2014). Fructose-1,6-bisphosphatase opposes renal carcinoma progression. Nature *513*, 251–255.

Li, F., Wang, Y., Zeller, K.I., Potter, J.J., Wonsey, D.R., O'Donnell, K.A., Kim, J.-W., Yustein, J.T., Lee, L.A., and Dang, C.V. (2005). Myc stimulates nuclearly encoded mitochondrial genes and mitochondrial biogenesis. Mol. Cell. Biol. *25*, 6225–6234.

Li, S., Swanson, S.K., Gogol, M., Florens, L., Washburn, M.P., Workman, J.L., and Suganuma, T. (2015). Serine and SAM Responsive Complex SESAME Regulates Histone Modification Crosstalk by Sensing Cellular Metabolism. Molecular Cell *60*, 408–421.

Li, X., Qian, X., and Lu, Z. (2017a). Local histone acetylation by ACSS2 promotes gene transcription for lysosomal biogenesis and autophagy. Autophagy *13*, 1790–1791.

Li, X., Yu, W., Qian, X., Xia, Y., Zheng, Y., Lee, J.-H., Li, W., Lyu, J., Rao, G., Zhang, X., et al. (2017b). Nucleus-Translocated ACSS2 Promotes Gene Transcription for Lysosomal Biogenesis and Autophagy. Molecular Cell *66*, 684–697.e689.

Lien, E.C., Lyssiotis, C.A., and Cantley, L.C. (2016). Metabolic Reprogramming by the PI3K-Akt-mTOR Pathway in Cancer. Recent Results Cancer Res. *207*, 39–72.

Lincet, H., and Icard, P. (2015). How do glycolytic enzymes favour cancer cell proliferation by nonmetabolic functions? Oncogene *34*, 3751–3759.

Linch, M., Miah, A.B., Thway, K., Judson, I.R., and Benson, C. (2014). Systemic treatment of soft-tissue sarcoma-gold standard and novel therapies. Nat Rev Clin Oncol *11*, 187–202.

Liu, G.-M., Li, Q., Zhang, P.-F., Shen, S.-L., Xie, W.-X., Chen, B., Wu, J., Hu, W.-J., Huang, X.-Y., and Peng, B.-G. (2018). Restoration of FBP1 suppressed Snail-induced epithelial to mesenchymal transition in hepatocellular carcinoma. Cell Death Dis *9*, 1132–12.

Luo, W., Hu, H., Chang, R., Zhong, J., Knabel, M., O'Meally, R., Cole, R.N., Pandey, A., and Semenza, G.L. (2011). Pyruvate kinase M2 is a PHD3-stimulated coactivator for hypoxia-inducible factor 1. Cell *145*, 732–744.

Majewski, N., Nogueira, V., Bhaskar, P., Coy, P.E., Skeen, J.E., Gottlob, K., Chandel, N.S., Thompson, C.B., Robey, R.B., and Hay, N. (2004). Hexokinase-mitochondria interaction mediated by Akt is required to inhibit apoptosis in the presence or absence of Bax and Bak. Molecular Cell *16*, 819–830.

McEwen, B.S., Allfrey, V.G., and Mirsky, A.E. (1963). Studies on Energy-Yielding Reactions in Thymus Nuclei. 2. Pathways of Aerobic Carbohydrate Catabolism. *238*, 2571–2578.

Mehren, von, M., Randall, R.L., Benjamin, R.S., Boles, S., Bui, M.M., Ganjoo, K.N., George, S., Gonzalez, R.J., Heslin, M.J., Kane, J.M., et al. (2018). Soft Tissue Sarcoma, Version 2.2018, NCCN Clinical Practice Guidelines in Oncology. J Natl Compr Canc Netw *16*, 536–563.

Mito, J.K., Riedel, R.F., Dodd, L., Lahat, G., Lazar, A.J., Dodd, R.D., Stangenberg, L., Eward, W.C., Hornicek, F.J., Yoon, S.S., et al. (2009). Cross species genomic analysis identifies a mouse model as undifferentiated pleomorphic sarcoma/malignant fibrous histiocytoma. PLoS ONE *4*, e8075.

Mizunuma, H., and Tashima, Y. (1990). Survey of fructose 1,6-bisphosphatase isoenzyme in rat organs and ontogenic expression of the enzyme in rat fetus. Int. J. Biochem *22*, 883–887.

Morrish, F., Giedt, C., and Hockenbery, D. (2003). c-MYC apoptotic function is mediated by NRF-1 target genes. Genes & Development *17*, 240–255.

Moullan, N., Mouchiroud, L., Wang, X., Ryu, D., Williams, E.G., Mottis, A., Jovaisaite, V., Frochaux, M.V., Quiros, P.M., Deplancke, B., et al. (2015). Tetracyclines Disturb Mitochondrial Function across Eukaryotic Models: A Call for Caution in Biomedical Research. Cell Rep *10*, 1681–1691.

Nakazawa, M.S., Eisinger-Mathason, T.S.K., Sadri, N., Ochocki, J.D., Gade, T.P.F., Amin, R.K., and Simon, M.C. (2016a). Epigenetic re-expression of HIF-2α suppresses soft tissue sarcoma growth. Nat Commun *7*, 10539.

Nakazawa, M.S., Keith, B., and Simon, M.C. (2016b). Oxygen availability and metabolic adaptations. Nat Rev Cancer *16*, 663–673.

Neary, C.L., and Pastorino, J.G. (2013). Akt inhibition promotes hexokinase 2 redistribution and glucose uptake in cancer cells. J. Cell. Physiol. *228*, 1943–1948.

Newsholme, E.A., and Crabtree, B. (1970). The role of fructose-1,6-diphosphatase in the regulation of glycolysis in skeletal muscle. FEBS Letters *7*, 195–198.

Nickerson, M.L., Jaeger, E., Shi, Y., Durocher, J.A., Mahurkar, S., Zaridze, D., Matveev, V., Janout, V., Kollarova, H., Bencko, V., et al. (2008). Improved identification of von Hippel-Lindau gene alterations in clear cell renal tumors. Clin. Cancer Res. *14*, 4726–4734.

Nissim, I., Horyn, O., Nissim, I., Daikhin, Y., Wehrli, S.L., Yudkoff, M., and Matschinsky, F.M. (2012). Effects of a glucokinase activator on hepatic intermediary metabolism: study with 13C-isotopomer-based metabolomics. Biochem. J. *444*, 537–551.

Pan, D., Mao, C., and Wang, Y.-X. (2013). Suppression of gluconeogenic gene expression by LSD1-mediated histone demethylation. PLoS ONE *8*, e66294.

Pastorino, J.G., Shulga, N., and Hoek, J.B. (2002). Mitochondrial binding of hexokinase II inhibits Bax-induced cytochrome c release and apoptosis. Journal of Biological Chemistry *277*, 7610–7618.

Phillips, D., Aponte, A.M., French, S.A., Chess, D.J., and Balaban, R.S. (2009). Succinyl-CoA synthetase is a phosphate target for the activation of mitochondrial metabolism. Biochemistry *48*, 7140–7149.

Platt, R.J., Chen, S., Zhou, Y., Yim, M.J., Swiech, L., Kempton, H.R., Dahlman, J.E., Parnas, O., Eisenhaure, T.M., Jovanovic, M., et al. (2014). CRISPR-Cas9 knockin mice for genome editing and cancer modeling. Cell *159*, 440–455.

Popanda, O., Fox, G., and Thielmann, H.W. (1998). Modulation of DNA polymerases alpha, delta and epsilon by lactate dehydrogenase and 3-phosphoglycerate kinase. Biochimica Et Biophysica Acta *1397*, 102–117.

Remels, A.H.V., Langen, R.C.J., Schrauwen, P., Schaart, G., Schols, A.M.W.J., and Gosker, H.R. (2010). Regulation of mitochondrial biogenesis during myogenesis. Mol. Cell. Endocrinol. *315*, 113–120.

Ritterson Lew, C., and Tolan, D.R. (2012). Targeting of several glycolytic enzymes using RNA interference reveals aldolase affects cancer cell proliferation through a non-glycolytic mechanism. *287*, 42554–42563.

Rossignol, R., Gilkerson, R., Aggeler, R., Yamagata, K., Remington, S.J., and Capaldi, R.A. (2004). Energy substrate modulates mitochondrial structure and oxidative capacity in cancer cells. Cancer Res. *64*, 985–993.

Sadri, N., and Zhang, P.J. (2013). Hypoxia-inducible factors: mediators of cancer progression; prognostic and therapeutic targets in soft tissue sarcomas. Cancers *5*, 320–333.

Scarpulla, R.C. (2008). Transcriptional paradigms in mammalian mitochondrial biogenesis and function. Physiol. Rev. *88*, 611–638.

Scarpulla, R.C. (2012). Nucleus-encoded regulators of mitochondrial function: integration of respiratory chain expression, nutrient sensing and metabolic stress. Biochimica Et Biophysica Acta *1819*, 1088–1097.

Schieber, M., and Chandel, N.S. (2014). ROS function in redox signaling and oxidative stress. Curr. Biol. *24*, R453–R462.

Sellers, K., Fox, M.P., Bousamra, M., Slone, S.P., Higashi, R.M., Miller, D.M., Wang, Y., Yan, J., Yuneva, M.O., Deshpande, R., et al. (2015). Pyruvate carboxylase is critical for non-small-cell lung cancer proliferation. J. Clin. Invest. *125*, 687–698.

Sen, N., Hara, M.R., Ahmad, A.S., Cascio, M.B., Kamiya, A., Ehmsen, J.T., Agrawal, N., Aggrawal, N., Hester, L., Doré, S., et al. (2009). GOSPEL: a neuroprotective protein that binds to GAPDH upon S-nitrosylation. Neuron *63*, 81–91.

Sen, N., Hara, M.R., Kornberg, M.D., Cascio, M.B., Bae, B.-I., Shahani, N., Thomas, B., Dawson, T.M., Dawson, V.L., Snyder, S.H., et al. (2008). Nitric oxide-induced nuclear GAPDH activates p300/CBP and mediates apoptosis. Nat. Cell Biol. *10*, 866–873.

Shaw, J.H.F., Humberstone, D.M., and Wolfe, R.R. (1988). Energy and Protein Metabolism in Sarcoma Patients. Annals of Surgery *207*, 283–289.

Si, W., Huang, W., Zheng, Y., Yang, Y., Liu, X., Shan, L., Zhou, X., Wang, Y., Su, D., Gao, J., et al. (2015). Dysfunction of the Reciprocal Feedback Loop between GATA3- and ZEB2-Nucleated Repression Programs Contributes to Breast Cancer Metastasis. Cancer Cell *27*, 822–836.

Siegel, R.L., Miller, K.D., and Jemal, A. (2019). Cancer statistics, 2019. CA Cancer J Clin *97*, 3133.

Sivanand, S., Rhoades, S., Jiang, Q., Lee, J.V., Benci, J., Zhang, J., Yuan, S., Viney, I., Zhao, S., Carrer, A., et al. (2017). Nuclear Acetyl-CoA Production by ACLY Promotes Homologous Recombination. Molecular Cell *67*, 252–265.

Sun, Y.J., Chou, C.C., Chen, W.S., Wu, R.T., Meng, M., and Hsiao, C.D. (1999). The crystal structure of a multifunctional protein: phosphoglucose isomerase/autocrine motility factor/neuroleukin. Proc. Natl. Acad. Sci. U.S.a. *96*, 5412–5417.

Sundararaj, K.P., Wood, R.E., Ponnusamy, S., Salas, A.M., Szulc, Z., Bielawska, A., Obeid, L.M., Hannun, Y.A., and Ogretmen, B. (2004). Rapid shortening of telomere length in response to ceramide involves the inhibition of telomere binding activity of nuclear glyceraldehyde-3-phosphate dehydrogenase. Journal of Biological Chemistry *279*, 6152–6162.

Sutendra, G., Kinnaird, A., Dromparis, P., Paulin, R., Stenson, T.H., Haromy, A., Hashimoto, K., Zhang, N., Flaim, E., and Michelakis, E.D. (2014). A Nuclear Pyruvate Dehydrogenase Complex Is Important for the Generation of Acetyl-CoA and Histone Acetylation. Cell *158*, 84–97.

Taylor, B.S., Barretina, J., Maki, R.G., Antonescu, C.R., Singer, S., and Ladanyi, M. (2011). Advances in sarcoma genomics and new therapeutic targets. Nat Rev Cancer *11*, 541–557.

Tejwani, G.A. (1983). Regulation of fructose-bisphosphatase activity. Adv. Enzymol. Relat. Areas Mol. Biol. *54*, 121–194.

Vander Heiden, M.G., and DeBerardinis, R.J. (2017). Understanding the Intersections between Metabolism and Cancer Biology. Cell *168*, 657–669.

Wang, H.-J., Hsieh, Y.-J., Cheng, W.-C., Lin, C.-P., Lin, Y.-S., Yang, S.-F., Chen, C.-C., Izumiya, Y., Yu, J.-S., Kung, H.-J., et al. (2014). JMJD5 regulates PKM2 nuclear translocation and reprograms HIF-1α-mediated glucose metabolism. Proc. Natl. Acad. Sci. U.S.a. *111*, 279–284.

Wang, W., Wang, L., Endoh, A., Hummelke, G., Hawks, C.L., and Hornsby, P.J. (2005). Identification of alpha-enolase as a nuclear DNA-binding protein in the zona fasciculata but not the zona reticularis of the human adrenal cortex. J. Endocrinol. *184*, 85–94.

Wang, Z., and Dong, C. (2019). Gluconeogenesis in Cancer: Function and Regulation of PEPCK, FBPase, and G6Pase. Trends Cancer *5*, 30–45.

Warburg, O. (1956). On respiratory impairment in cancer cells. Science *124*, 269–270.

Watanabe, H., Takehana, K., Date, M., Shinozaki, T., and Raz, A. (1996). Tumor cell autocrine motility factor is the neuroleukin/phosphohexose isomerase polypeptide. Cancer Res. *56*, 2960–2963.

Weinberg, S.E., and Chandel, N.S. (2015). Targeting mitochondria metabolism for cancer therapy. *11*, 9–15.

Wellen, K.E., Hatzivassiliou, G., Sachdeva, U.M., Bui, T.V., Cross, J.R., and Thompson, C.B. (2009). ATP-citrate lyase links cellular metabolism to histone acetylation. Science *324*, 1076–1080.

Yalcin, A., Clem, B.F., Imbert-Fernandez, Y., Ozcan, S.C., Peker, S., O'Neal, J., Klarer, A.C., Clem, A.L., Telang, S., and Chesney, J. (2014). 6-Phosphofructo-2-kinase (PFKFB3) promotes cell cycle progression and suppresses apoptosis via Cdk1-mediated phosphorylation of p27. Cell Death Dis *5*, e1337.

Yalcin, A., Clem, B.F., Simmons, A., Lane, A., Nelson, K., Clem, A.L., Brock, E., Siow, D., Wattenberg, B., Telang, S., et al. (2009). Nuclear targeting of 6-phosphofructo-2-kinase

(PFKFB3) increases proliferation via cyclin-dependent kinases. Journal of Biological Chemistry *284*, 24223–24232.

Yang, J., Jin, X., Yan, Y., Shao, Y., Pan, Y., Roberts, L.R., Zhang, J., Huang, H., and Jiang, J. (2017). Inhibiting histone deacetylases suppresses glucose metabolism and hepatocellular carcinoma growth by restoring FBP1 expression. Sci. Rep. *7*, 43864.

Yang, W., Xia, Y., Cao, Y., Zheng, Y., Bu, W., Zhang, L., You, M.J., Koh, M.Y., Cote, G., Aldape, K., et al. (2012a). EGFR-induced and PKCε monoubiquitylation-dependent NF-κB activation upregulates PKM2 expression and promotes tumorigenesis. Molecular Cell *48*, 771–784.

Yang, W., Xia, Y., Ji, H., Zheng, Y., Liang, J., Huang, W., Gao, X., Aldape, K., and Lu, Z. (2011). Nuclear PKM2 regulates β-catenin transactivation upon EGFR activation. Nature *480*, 118–122.

Yang, W., Zheng, Y., Xia, Y., Ji, H., Chen, X., Guo, F., Lyssiotis, C.A., Aldape, K., Cantley, L.C., and Lu, Z. (2012b). ERK1/2-dependent phosphorylation and nuclear translocation of PKM2 promotes the Warburg effect. Nat. Cell Biol. *14*, 1295–1304.

Yogev, O., Yogev, O., Singer, E., Shaulian, E., Goldberg, M., Fox, T.D., and Pines, O. (2010). Fumarase: a mitochondrial metabolic enzyme and a cytosolic/nuclear component of the DNA damage response. PLoS Biol. *8*, e1000328.

Yuan, T.L., and Cantley, L.C. (2008). PI3K pathway alterations in cancer: variations on a theme. Oncogene *27*, 5497–5510.

Zhang, J., Wang, J., Xing, H., Li, Q., Zhao, Q., and Li, J. (2016). Down-regulation of FBP1 by ZEB1-mediated repression confers to growth and invasion in lung cancer cells. Mol. Cell. Biochem. *411*, 331–340.

Zhao, S., Torres, A., Henry, R.A., Trefely, S., Wallace, M., Lee, J.V., Carrer, A., Sengupta, A., Campbell, S.L., Kuo, Y.-M., et al. (2016). ATP-Citrate Lyase Controls a Glucose-to-Acetate Metabolic Switch. Cell Rep *17*, 1037–1052.

Zheng, H., Gupta, V., Patterson-Fortin, J., Bhattacharya, S., Katlinski, K., Wu, J., Varghese, B., Carbone, C.J., Aressy, B., Fuchs, S.Y., et al. (2013). A BRISC-SHMT complex deubiquitinates IFNAR1 and regulates interferon responses. Cell Rep *5*, 180–193.

Zheng, L., Roeder, R.G., and Luo, Y. (2003). S phase activation of the histone H2B promoter by OCA-S, a coactivator complex that contains GAPDH as a key component. Cell *114*, 255–266.

Zhou, Y., Yi, X., Stoffer, J.B., Bonafe, N., Gilmore-Hebert, M., McAlpine, J., and Chambers, S.K. (2008). The multifunctional protein glyceraldehyde-3-phosphate dehydrogenase is both regulated and controls colony-stimulating factor-1 messenger RNA stability in ovarian cancer. Mol. Cancer Res. *6*, 1375–1384.

Zhu, Y., Shi, M., Chen, H., Gu, J., Zhang, J., Shen, B., Deng, X., Xie, J., Zhan, X., and Peng, C. (2015). NPM1 activates metabolic changes by inhibiting FBP1 while promoting the tumorigenicity of pancreatic cancer cells. Oncotarget *6*, 21443–21451.